



NAVAL POSTGRADUATE SCHOOL

MONTEREY, CALIFORNIA

THESIS

**EXPLORATION OF INTEGRATED VISIBLE TO NEAR-,
SHORTWAVE-, AND LONGWAVE-INFRARED
(FULL-RANGE) SPECTRAL ANALYSIS**

by

Shelli R. Cone

September 2014

Thesis Advisor:
Second Reader:

Fred A. Kruse
Meryl L. McDowell

Approved for public release; distribution is unlimited

THIS PAGE INTENTIONALLY LEFT BLANK

REPORT DOCUMENTATION PAGE			<i>Form Approved OMB No. 0704-0188</i>	
Public reporting burden for this collection of information is estimated to average 1 hour per response, including the time for reviewing instruction, searching existing data sources, gathering and maintaining the data needed, and completing and reviewing the collection of information. Send comments regarding this burden estimate or any other aspect of this collection of information, including suggestions for reducing this burden, to Washington headquarters Services, Directorate for Information Operations and Reports, 1215 Jefferson Davis Highway, Suite 1204, Arlington, VA 22202-4302, and to the Office of Management and Budget, Paperwork Reduction Project (0704-0188) Washington DC 20503.				
1. AGENCY USE ONLY (Leave blank)		2. REPORT DATE September 2014	3. REPORT TYPE AND DATES COVERED Master's Thesis	
4. TITLE AND SUBTITLE EXPLORATION OF INTEGRATED VISIBLE TO NEAR-, SHORTWAVE-, AND LONGWAVE-INFRARED (FULL-RANGE) SPECTRAL ANALYSIS			5. FUNDING NUMBERS	
6. AUTHOR(S) Shelli R. Cone				
7. PERFORMING ORGANIZATION NAME(S) AND ADDRESS(ES) Naval Postgraduate School Monterey, CA 93943-5000			8. PERFORMING ORGANIZATION REPORT NUMBER	
9. SPONSORING /MONITORING AGENCY NAME(S) AND ADDRESS(ES) N/A			10. SPONSORING/MONITORING AGENCY REPORT NUMBER	
11. SUPPLEMENTARY NOTES The views expressed in this thesis are those of the author and do not reflect the official policy or position of the Department of Defense or the U.S. Government. IRB Protocol number ____N/A____.				
12a. DISTRIBUTION / AVAILABILITY STATEMENT Approved for public release; distribution is unlimited			12b. DISTRIBUTION CODE	
13. ABSTRACT (maximum 200 words) Visible to near-, shortwave-, and longwave-infrared (VNIR, SWIR, LWIR) remote sensing data are typically analyzed in their individual wavelength regions, even though theory suggests combined use would emphasize complementary features. This research explored the potential for improvements in material classification using integrated datasets. Hyperspectral (HSI) VNIR and SWIR data from the MaRSuper Sensor System (MSS-1) were analyzed with HSI LWIR data from the Spatially Enhanced Broadband Array Spectrograph System (SEBASS) to determine differences between individual (baseline) and combined analyses. The first integration approach applied separate minimum noise fraction (MNF) transforms to the three regions and combined only non-noise transformed bands from the individual regions during analysis. The second approach integrated over 470 hyperspectral bands covering the VNIR, SWIR, and LWIR wavelengths before using MNF analysis to isolate linear band combinations containing high signal to noise. Spectral endmembers isolated from data were unmixed using partial unmixing. The feasible and high abundance pixels were spatially mapped using a consistent feasibility ratio threshold. Both integration methods enabled straightforward and effective identification, characterization, and mapping of the scene because higher variability existed between endmembers and background. Results were compared to the baseline analysis. Material identification was more conclusive when analyzing across the full spectrum.				
14. SUBJECT TERMS Hyperspectral Imaging, Full-Range Spectral Analysis, Visible to Near Infrared, Shortwave Infrared, MSS-1, Longwave Infrared, SEABASS			15. NUMBER OF PAGES 129	
			16. PRICE CODE	
17. SECURITY CLASSIFICATION OF REPORT Unclassified	18. SECURITY CLASSIFICATION OF THIS PAGE Unclassified	19. SECURITY CLASSIFICATION OF ABSTRACT Unclassified	20. LIMITATION OF ABSTRACT UU	

THIS PAGE INTENTIONALLY LEFT BLANK

Approved for public release; distribution is unlimited

**EXPLORATION OF INTEGRATED VISIBLE TO NEAR-, SHORTWAVE-, AND
LONGWAVE-INFRARED (FULL-RANGE) SPECTRAL ANALYSIS**

Shelli R. Cone
Contractor, Scitor Corporation
B.S., Purdue University, 2012

Submitted in partial fulfillment of the
requirements for the degree of

MASTER OF SCIENCE IN REMOTE SENSING INTELLIGENCE

from the

**NAVAL POSTGRADUATE SCHOOL
September 2014**

Author: Shelli R. Cone

Approved by: Dr. Fred A. Kruse
Thesis Advisor

Dr. Meryl L. McDowell
Second Reader

Dr. Dan C. Boger
Chair, Department of Information Sciences Department

THIS PAGE INTENTIONALLY LEFT BLANK

ABSTRACT

Visible to near-, shortwave-, and longwave-infrared (VNIR, SWIR, LWIR) remote sensing data are typically analyzed in their individual wavelength regions, even though theory suggests combined use would emphasize complementary features. This research explored the potential for improvements in material classification using integrated datasets. Hyperspectral (HSI) VNIR and SWIR data from the MaRSuper Sensor System (MSS-1) were analyzed with HSI LWIR data from the Spatially Enhanced Broadband Array Spectrograph System (SEBASS) to determine differences between individual (baseline) and combined analyses. The first integration approach applied separate minimum noise fraction (MNF) transforms to the three regions and combined only non-noise transformed bands from the individual regions during analysis. The second approach integrated over 470 hyperspectral bands covering the VNIR, SWIR, and LWIR wavelengths before using MNF analysis to isolate linear band combinations containing high signal to noise. Spectral endmembers isolated from data were unmixed using partial unmixing. The feasible and high abundance pixels were spatially mapped using a consistent feasibility ratio threshold. Both integration methods enabled straight-forward and effective identification, characterization, and mapping of the scene because higher variability existed between endmembers and background. Results were compared to the baseline analysis. Material identification was more conclusive when analyzing across the full spectrum.

THIS PAGE INTENTIONALLY LEFT BLANK

TABLE OF CONTENTS

I.	INTRODUCTION	1
II.	BACKGROUND	3
A.	ELECTROMAGNETIC RADIATION	3
B.	SPECTROSCOPY	5
1.	Radiance	5
2.	Reflectance	6
3.	Thermal Emission	7
C.	REMOTE SENSING	9
1.	Imaging Spectrometry	10
2.	Atmospheric Effects	13
D.	PREVIOUS WORK: FULL-RANGE SPECTRAL ANALYSIS	16
E.	HYPERSPECTRAL SENSORS, DATA SET, AND STUDY SITE	22
1.	Hyperspectral Sensors	22
a.	<i>VNIR-SWIR Sensor</i>	<i>22</i>
b.	<i>LWIR Sensor</i>	<i>23</i>
2.	Study Site	25
3.	Data Sets	25
III.	APPROACH AND METHODS	27
A.	VNIR-SWIR DATA PREPARATION	27
1.	Destriping	27
2.	Atmospheric Correction	30
a.	<i>Quick Atmospheric Correction</i>	<i>32</i>
b.	<i>Fast Line-of-Sight Atmosphere Analysis of Spectral Hypercubes</i>	<i>34</i>
c.	<i>Radiative-Transfer-Ground-Calibration</i>	<i>38</i>
3.	Geometric Corrections	39
a.	<i>Georeferenced Geometry Lookup Table</i>	<i>40</i>
b.	<i>Image-to-Map Registration</i>	<i>41</i>
B.	LWIR DATA PREPARATION	42
1.	Sensor Artifact Removal	43
2.	Atmospheric Correction	44
a.	<i>In-Scene Atmospheric Correction</i>	<i>44</i>
b.	<i>Fast Line-of-Sight Atmosphere Analysis of Spectral Hypercubes – Infrared</i>	<i>45</i>
3.	Temperature Emissivity Separation	46
4.	Geometric Corrections	50
a.	<i>Georeferenced Geometry Lookup Table</i>	<i>50</i>
b.	<i>Image-to-Image Registration</i>	<i>52</i>
C.	ANALYSIS APPROACHES	52
1.	Standard Hyperspectral Analysis	53
a.	<i>Spectral Data Reduction</i>	<i>54</i>

b.	<i>Spatial Data Reduction</i>	55
c.	<i>Visualization</i>	55
d.	<i>Identification</i>	56
e.	<i>Mapping and Characterization</i>	57
2.	Integration	60
a.	<i>MNF Integration</i>	60
b.	<i>Full Integration</i>	61
3.	Field Spectroscopy and Validation	61
a.	<i>Spectra Vista Corporation (SVC)</i>	62
b.	<i>Designs and Prototypes (D&P)</i>	63
IV.	RESULTS AND DISCUSSION	65
A.	STANDARD HYPERSPECTRAL ANALYSIS APPROACH	65
B.	MNF INTEGRATION APPROACH	74
C.	FULL INTEGRATION APPROACH	81
D.	COMPARISON AND DISCUSSION OF IMAGE MAP RESULTS	88
1.	Comparison	90
2.	Discussion	91
V.	SUMMARY AND CONCLUSIONS	95
VI.	RECOMMENDATIONS FOR FUTURE WORK	99
	LIST OF REFERENCES	101
	INITIAL DISTRIBUTION LIST	109

LIST OF FIGURES

Figure 1.	Electromagnetic Spectrum (from Shapley, 2012).	4
Figure 2.	The four fundamental energy interactions with matter (from Olsen, 2014).	4
Figure 3.	Comparison of Blackbody, Graybody, and Selective Radiator (from Riedl, 2001).	8
Figure 4.	The imaging spectroscopy concept includes an imaging sensor with a large number of narrow and contiguous spectral bands (from Shaw & Burke, 2003).	11
Figure 5.	Comparison of spectral resolution of HSI and MSI data (from Goetz, 2009).	12
Figure 6.	Hyperspectral Imaging Applications (from Shaw & Burke, 2003).	13
Figure 7.	Atmospheric Transmission Plot of VNIR-SWIR (from Berk et al., 1989).	14
Figure 8.	MODTRAN Plot displaying atmospheric transmission bands (from Olsen, 2014).	14
Figure 9.	Atmospheric scattering effects caused by the size of the scattering agent (from Olsen, 2014).	15
Figure 10.	Mineral maps of Comstock mining district around Virginia City, Nevada (from Vaughan & Calvin, 2004).	19
Figure 11.	The results from study conducted by Chen, et al. (2007) to determine the advantage of using combined wavelength datasets.	20
Figure 12.	Signal-to-noise ratio comparison of MaRS to 2004 AVIRIS (after Simi & Olchowski, 2009).	23
Figure 13.	Comparison of SEBASS emissivity spectrum (hydrothermal silica, Cuprite, NV) and laboratory spectrum of quartz (JHU Minerals Emissivity spectral library).	24
Figure 14.	MSS-1 and SEBASS georeferenced (not registered) coverage area of the NNSS location.	26
Figure 15.	MSS-1 calibrated radiance true color image (left), MNF-transformed image (MNF Bands 1, 2, 3 as RGB) showing striping problems (right).	28
Figure 16.	MNF-transformed image without destriping (left), MNF-transformed image with THOR destriping applied (right). MNF Bands 1, 2, 3 as RGB.	29
Figure 17.	Comparison of Destriping: SPEAR Vertical Stripe Removal (left) and THOR De-Striping (right).	30
Figure 18.	Outline of QUAC data processing algorithm (from Bernstein, Jin, Gregor, & Adler-Golden, 2012).	33
Figure 19.	Comparison of the radiance and QUAC corrected reflectance spectra. QUAC corrected true color reflectance image (left). Radiance ($\mu W \cdot cm^{-2} \cdot sr^{-1} \cdot \mu m^{-1}$) spectrum and QUAC corrected reflectance (scaled from 0 to 10,000) spectrum of pixel (335, 892) (right).	34
Figure 20.	QUAC reflectance spectrum (red), FLAASH reflectance spectrum using U.S. Standard atmospheric model (green), FLAASH reflectance spectrum using Mid-Latitude Summer atmospheric model (blue). Spectra are representative of a single pixel located at (335,892).	37

Figure 21.	Column water vapor (cm) obtained from the Mid-Latitude Summer FLAASH algorithm.....	38
Figure 22.	Comparison of FLAASH and RTGC correction results against ground measurements. Left: Manmade target (335,892), Right: Soil target (349,209).....	39
Figure 23.	GLT Sample Lookup image (left), GLT Line Lookup image (center), Georeferenced Reflectance image (right). The dark pixels in the GLT images represent interpolated pixels. The dark area in the georeferenced image is the image boundary of no data.	41
Figure 24.	True color unregistered MSS-1 image showing GCPs (left), Geocorrected MSS-1 image (right).....	42
Figure 25.	MNF Bands #1-3 exposed the non-linear focal plane array and MNF Band #4 showed the sensor artifact. MNF Band #5 (right) represented the expected MNF result.	43
Figure 26.	ISAC Results for single pixel SEBASS LWIR data.	45
Figure 27.	Comparison of ISAC and FLAASH-IR radiance spectra: coated road pixel (left) and vegetation pixel (right).	46
Figure 28.	Comparison of ISAC - NEM and FLAASH-IR - NEM results for SEBASS LWIR data.....	47
Figure 29.	The temperature range, in both the original dataset (left) and the data corrected for sensor artifacts (right), was approximately 301 to 328°K.....	49
Figure 30.	Comparison of uncorrected LWIR emissivity data to corrected data.	50
Figure 31.	GLT Sample Lookup image (left), GLT Line Lookup image (center), Georeferenced Emissivity image (right). The dark pixels in the GTL images represent interpolated pixels and the dark area in the georeferenced image is image boundary of no data.....	51
Figure 32.	GCPs from base MSS-1 Band 52 (left) aligned with GCPs on warped SEBASS Band 65 (center) used to register the SEBASS image (right).	52
Figure 33.	Subset of VNIR-SWIR and LWIR data used for integrated analysis.	53
Figure 34.	N-Dimensional processing flow for VNIR-SWIR HSI data (from Boardman & Kruse, 2011).....	54
Figure 35.	MTMF Feasibility Cone Concept (from Boardman & Kruse, 2011).....	58
Figure 36.	Examples of dispersal of pixels in MTMF plot; compact background and isolated endmember (left) compared to distributed background and endmembers with inclusion of background pixels using the 0.04 feasibility ratio threshold (right).	60
Figure 37.	SVC reflectance field measurements of F1 Road.....	63
Figure 38.	D&P emissivity field measurements averages of F1 Road (red) and F2 Road (green).	64
Figure 39.	Linear MNF transform results of VIS (left), SWIR (center), LWIR (right) displaying MNF bands 1, 2, 3 as RGB.....	66
Figure 40.	Image Map of MSS-1 VNIR endmembers using a feasibility ratio threshold of 0.04 (Top Left); VNIR endmember reflectance spectra extracted using MNF data (Right and Bottom Spectral Plots).	69

Figure 41.	Image Map of MSS-1 SWIR endmembers using a feasibility ratio threshold of 0.04 (Top Left); SWIR endmember reflectance spectra extracted using MNF data (Right and Bottom Spectral Plots).	71
Figure 42.	Differences between road (Soil-Road #2 [blue] and Soil-Road #4 [cyan]) and bare soil (Soil #5 [orange]).	72
Figure 43.	Image Map of SEBASS LWIR endmembers using a feasibility ratio threshold of 0.04 (Top Left); LWIR endmember reflectance spectra extracted using MNF data (Right and Bottom Spectral Plots).	73
Figure 44.	Comparison of ratio threshold at 0.04 (red) and 0.02 (green).	74
Figure 45.	Image Map of MNF Integration endmembers using a feasibility ratio threshold of 0.2.	75
Figure 46.	True color image showing classification results of Man-made #12-#15 (left); VNIR-SWIR reflectance spectra (top right); LWIR emissivity spectra (bottom right).	77
Figure 47.	Full range comparison of spatially similar soil (Soil #6, Soil #7) and road (Road #3, Road #4) endmembers; VNIR-SWIR reflectance spectra (left) and LWIR emissivity spectra (right).	78
Figure 48.	True color image showing classification results of Road #5 and #6 (left); VNIR-SWIR reflectance spectra of Road #5-#8 (top right); LWIR emissivity spectra of Road #6-8 (bottom right).	79
Figure 49.	Spectral comparison of field (black) and image endmember spectra (green).	80
Figure 50.	Spectral comparison of sagebrush library spectrum and vegetation image endmember spectra.	81
Figure 51.	Linear MNF transform results of full integration image displaying MNF bands 1, 2, 3 as RGB.	82
Figure 52.	Image Map of MNF Integration endmembers using a feasibility ratio threshold of 0.2.	83
Figure 53.	Spectral comparison of assumed plastic spectra; VNIR-SWIR reflectance spectra (left); LWIR emissivity spectra (right).	84
Figure 54.	Spectral comparison of assumed plastic spectra; VNIR-SWIR reflectance spectra (left); LWIR emissivity spectra (right).	85
Figure 55.	Spectral comparison of soil spectra; VNIR-SWIR reflectance spectra (left); LWIR emissivity spectra (right).	85
Figure 56.	True color image showing classification results soil and road endmembers (left); VNIR-SWIR reflectance spectra (top right); LWIR emissivity spectra (bottom right).	87
Figure 57.	Spectral comparison of assumed vegetation endmember spectra; VNIR-SWIR reflectance spectra (left); LWIR emissivity spectra (right).	88
Figure 58.	Comparison of MTMF feasibility ratio classification maps; VNIR (top left), SWIR (top right), LWIR (middle center); MNF Integration (bottom left), Full Integration (bottom right).	89

THIS PAGE INTENTIONALLY LEFT BLANK

LIST OF TABLES

Table 1.	Sensor Parameters for FLAASH	35
Table 2.	FLAASH Parameters.....	36
Table 3.	GLT Parameters for MSS-1 Data	41
Table 4.	GLT Parameters for SEBASS Data.....	51
Table 5.	MNF Transform Parameters of VNIR-SWIR-LWIR data.....	65
Table 6.	Number of endmembers from each wavelength region	67
Table 7.	Description of comparison locations.....	88

THIS PAGE INTENTIONALLY LEFT BLANK

LIST OF ACRONYMS AND ABBREVIATIONS

ACORN	Atmospheric Correction Now
ASD	Advanced Spectral Devices
ASTER	Advanced Spaceborne Thermal Emission and Reflection Radiometer
ATCOR	Atmospheric Correction
ATREM	Atmospheric Removal
AVIRIS	Airborne Visible/Infrared Imaging Spectrometer
DAIS	Digital Airborne Imaging Spectrometer
DN	Digital Number
D&P	Designs & Prototypes
EM	Electromagnetic
EMR	Electromagnetic Radiation
ENVI	Environment for Visualizing Images
EO	Electro-optical
FFC	Flat field correction
FLAASH	Fast Line-of-sight Atmospheric Analysis of Spectral Hypercubes
GCPs	Ground Control Points
GLT	Geometry Lookup Table
GSD	Ground Separation Distance
HgCdTe	Mercury Cadmium Telluride
HSI	Hyperspectral Imaging
HST	HyperSpecTIR
HyMap	Hyperspectral Mapping
HypIRI	Hyperspectral Infrared Imager
IARR	Internal Average Relative Reflectance
IGM	Input Geometry File
InGaAs	Indium Gallium Arsenide
InSb	Indium Antimonide
ISAC	In-Scene Atmospheric Correction
JPL	Jet Propulsion Laboratory

LiDAR	Light Detection and Ranging
LWIR	Longwave-Infrared
MaRS	Mapping Reflected-energy Sensor
MASTER	MODIS/ASTER Airborne Simulator
MF	Match Filtering
MNF	Minimum Noise Fraction
MODIS	Moderate-resolution Imaging Spectroradiometer
MODTRAN	Moderate resolution atmospheric Transmission
MSI	Multispectral Imaging
MSS-1	MaRSuper Sensor System
MT	Mixture-Tuned
MTMF	Mixture-Tuned Matched Filtering
MWIR	Midwave-Infrared
NASA	National Aeronautics and Space Administration
NRC	National Research Council
PPI	Pixel Purity Index
QUAC	Quick Atmospheric Correction
RADAR	Radio Detection and Ranging
SAM	Spectral Angle Mapper
SEBASS	Spatially Enhanced Broadband Array Spectrograph System
SFF	Spectral Feature Fitting
SONAR	Sound Navigation and Ranging
SpecTIR	Spectral Technology and Innovative Research Corporation
SVC	Spectra Vista Corporation
SWIR	Shortwave-Infrared
TIR	Thermal Infrared
TIMS	Thermal Infrared Multispectral Scanner
UTM	Universal Transverse Mercator
VNIR	Visible to Near-Infrared
WGS-84	World Geodetic System from 1984

ACKNOWLEDGMENTS

I would like to thank Dr. Fred Kruse and Dr. R. Christopher Olsen for their dedication in expanding the essential knowledge base of remote sensing. Words do not express my gratitude for the support and advice provided by Dr. Kruse and Dr. Meryl McDowell throughout my thesis writing experience. I would also like to thank Mr. Herbert Mitchell for his support of my attendance at the Naval Postgraduate School. Studying at NPS has been a truly unique opportunity professionally and personally. I also would like to thank the members of the Integrated Signatures Program for providing invaluable advice and data. Another thank-you goes to the leadership at Scitor Corporation for allowing me to participate in the Remote Sensing Intelligence master's program, as well as my wonderful colleagues on the Strategic Analysis Team. Lastly, I would like to thank my family for their unwavering support of all my endeavors.

THIS PAGE INTENTIONALLY LEFT BLANK

I. INTRODUCTION

Spectra of surface materials have historically been collected and analyzed in separate wavelength regions, which include the visible to near-infrared (VNIR), shortwave-infrared (SWIR), midwave-infrared (MWIR), and longwave-infrared (LWIR). Each individual region is sensitive to different electronic and vibrational processes based on the physiochemical makeup of the substance in question. The LWIR and MWIR regions retain fundamental vibrational features, while the VNIR and SWIR regions expose overtones and combination tones. When spectra are measured and analyzed using only individual regions, additional features that occur at wavelengths outside of a single region may be undetected. For example, vegetation pigments are detected in the visible region, with prominent absorption features near 0.4 and 0.68 micrometers. Vegetation also has high reflectance in the NIR near 0.8 micrometers, the so-called “IR plateau.” Spectra of leaves in the SWIR wavelengths exhibit specific spectral features due to chemical composition. Only subtle spectral features exist for vegetation in the LWIR (van der Meer & de Jong, 2011). Another example is quartz, which has broad emissivity features in the LWIR caused by silicon-oxygen stretching vibrations in the silicate lattice, but is mostly featureless in the VNIR and SWIR wavelength regions (Lyon, 1964; Moersch & Christensen, 1995; van der Meer & de Jong, 2011; Vincent & Thomson, 1972). This thesis explores the topic of full-spectrum terrain analysis and classification for improved detection and identification of surface materials.

The strategy used for this study was to integrate VNIR, SWIR, and LWIR spectra (0.4 to 14 micrometers, excluding MWIR channels from 3 to 5 micrometers), to exploit both reflective and emissive signatures. Existing algorithms for analysis of atmospheric corrections, temperature emissivity separation, and geometric corrections were evaluated and implemented as part of this research. Two integration techniques were analyzed and compared to a standard hyperspectral analysis approach utilizing individual wavelength regions. Ground point spectra collected in the field were used to correct for sensor calibration errors and for identification of spectral endmember—the key spectral signatures that explain the data variability.

Integration of datasets has the potential to help all aspects of imaging spectrometry, including mapping, target and anomaly detection, and identification of surface materials. This technique is expected to expedite the hyperspectral analysis process and provide efficient identification and mapping capabilities. The addition of ground truth spectra in the analysis process should increase the probability of conclusive identification.

Following this introduction, an inclusive background (Chapter II) on electromagnetic radiation, the science of spectroscopy, and the remote sensing discipline is described. The approaches and methods section (Chapter III) explains the atmospheric and geometric corrections applied to the original datasets and the specific algorithms used for hyperspectral analysis and integration. The next section (Chapter IV) presents and compares the results from the standard analysis and the two integrated approaches. Finally, the research is summarized and conclusions are offered (Chapter V) on the benefits of integrating the VNIR-SWIR-LWIR wavelength regions. Suggestions for future research are offered in Chapter VI.

II. BACKGROUND

This section introduces the vast field and capabilities of remote sensing. For initial understanding of the subject matter it is imperative to review the electromagnetic continuum and the interactions of light at both the macroscopic and microscopic scale. Both reflectance and emission spectroscopy are introduced. Next, various remote sensing technologies are discussed, with emphasis on imaging spectrometry. An overview of previous full-range spectral analysis is also provided. Lastly, the hyperspectral sensors, the dataset, and the study site used in this thesis are presented.

A. ELECTROMAGNETIC RADIATION

The electromagnetic (EM) spectrum spans all wavelengths and frequencies of energy interactions described as electromagnetic radiation (EMR) (Olsen, 2014; Richards & Jia, 2013) (Figure 1). EMR can be described by its energy, frequency, or wavelength. Energy E is related to frequency ν as described by Planck's relation using Planck's constant h , which is approximately equivalent to $6.62 \times 10^{-34} \text{ J} \cdot \text{s}$.

$$E = h\nu \quad (1)$$

Frequency ν and wavelength λ are inversely related with respect to the speed of light c , which is approximated to be $3.0 \times 10^8 \frac{\text{m}}{\text{s}}$. Equation 2 details the fundamental inverse relationship.

$$\lambda = \frac{c}{\nu} \quad (2)$$

Frequency can be replaced by wavelength changing the energy equation (Equation 1) to:

$$E = h \frac{c}{\lambda} \quad (3)$$

High energy waves, such as gamma rays, are characterized by short wavelengths and high frequencies, and are located at one extreme of the EM spectrum. At the other end of the EM spectrum lower energy waves, such as microwaves and radio waves, are represented by longer wavelengths and lower frequencies (Figure 1).

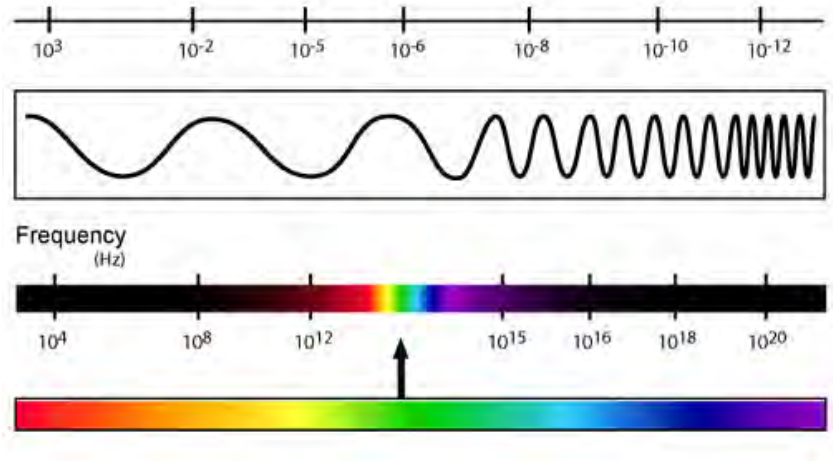


Figure 1. Electromagnetic Spectrum (from Shapley, 2012).

The four fundamental EMR interactions with matter are transmission, reflectance, scattering, and absorption. The relative importance of these interactions is based on the compositional and physical properties of the medium, the specific wavelength of the incident radiation, and the angle at which the light strikes the surface (Figure 2) (Olsen, 2014). The variation in partitioning of energy as a function of wavelength is the key to differentiating and characterizing different materials.

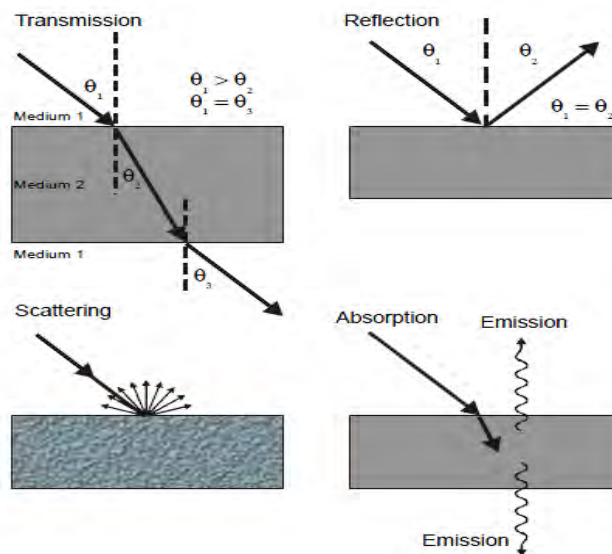


Figure 2. The four fundamental energy interactions with matter (from Olsen, 2014).

Transmission occurs when incident radiation passes through a material (Olsen, 2014). Light transmission must be accounted for to analyze absorption features caused by photon interactions with the atomic structure of the chemicals present in the material being observed (Richards & Jia, 2013). Specular reflectance occurs when incident radiation bounces off the surface in a single, predictable direction and is characteristic of smooth surfaces relative to the wavelengths of the light source (Olsen, 2014). Scattering, or diffuse reflection, occurs when incident radiation hits the surface and is returned in many unpredictable directions, including the direction from which it originated (Olsen, 2014). Diffuse reflection is characteristic of rough surfaces relative to the wavelengths of the light source. Absorption occurs when incident radiation is absorbed by a medium because the material is opaque to the incident radiation. A portion of the absorbed radiation is converted into heat energy and some of the radiation may later be emitted (Olsen, 2014).

B. SPECTROSCOPY

The science of spectroscopy investigates material properties based on the interaction of EMR with matter (Green, 1998). When incident light interacts with a selected substance, light at certain wavelengths is absorbed, while at other wavelengths light is reflected or transmitted (van der Meer & de Jong, 2011). Molecular vibrations and electronic processes produce key spectral features that have unique positions, shapes, depth, and width parameters related to the crystal and chemical structure of the material (van der Meer & de Jong, 2011). The primary vibrational interactions are measureable in the LWIR, while overtones and combination tones can be measured in the VNIR and SWIR portion of the EM spectrum.

1. Radiance

Radiance is the amount of optical power from a surface area that is emitted into a solid angle (Berk, Bernstein, & Robertson, 1989; Olsen, 2014; Rees, 2013; Salvaggio, Miller, Baue, & Lewis, 2011; van der Meer & de Jong, 2011). This measurement is indicative of how much power radiated, by a reflective or emitting surface, will be received by an optical instrument looking at the surface from a specified angle.

Radiance, L in units $\frac{Watts}{m^2 \cdot \mu \cdot ster}$ is defined as:

$$L = \frac{2hc^2}{\lambda^5} \frac{1}{e^{\frac{hc}{\lambda kT}} - 1} \quad (4)$$

where

L	Spectral radiance
T	Absolute temperature
k_B	Boltzmann constant, $1.38 \times 10^{-23} \frac{m^2 \cdot kg}{s^2 \cdot K}$
h	Planck constant, $6.62 \times 10^{-34} J \cdot s$
c	Speed of light, $3.0 \times 10^8 \frac{m}{s}$

2. Reflectance

The ratio of the intensity of the light reflected from the sample material to the intensity of the incident light is defined as the reflectance (van der Meer & de Jong, 2011). Reflectance spectroscopy is the study of light as a function of wavelength that has been reflected or scattered from matter. As photons enter a material, some are reflected from the surface, some pass through the surface, and others are absorbed. Primary reflectance features are seen in the VNIR and SWIR wavelengths.

Spectral features occurring in the VNIR wavelength region from 0.4 to 1.0 micrometers are caused by electronic processes. Electronic processes include crystal field effects, charge transfer, conduction band absorption, and color centers (van der Meer & de Jong, 2011). A common electronic process is seen in healthy vegetation, which has an absorption feature at approximately 0.68 micrometers from the presences of chlorophyll (Elvidge, 1990).

Features occurring in the SWIR wavelength region from 1.0 to near 2.5 micrometers are the result of molecular vibrational processes. Rocks and soils have absorption features that depend on the specific molecules and the types of molecular bonds present in the substance (Goetz, Vane, Solomon, & Rock, 1985). Most mica materials have an absorption feature near 2.2 micrometers caused by Al-O, Fe-O, and

Mg-O bending vibrations. Prominent features such as these can be used to uniquely identify materials.

3. Thermal Emission

Heat energy is the result of kinetic energy from random motion of particles of matter. As heat energy increases, the number of collisions also increases, which may cause changes in vibrational, orbital, and rotational orientations. The change in physical properties of particles results in the emission of EMR, causing the heat energy to be converted into radiant energy (van der Meer & de Jong, 2011). Thermal radiation is emitted by all objects at temperatures above absolute zero (van der Meer & de Jong, 2011). This emitted energy is in the 3 to longward of 20 micrometer range. This thesis explores these effects principally in the LWIR region, which covers the spectral range from approximately 8 to 14 micrometers.

A blackbody is a perfect emitter of all incident energy and transforms heat energy to radiant energy at the maximum rate (van der Meer & de Jong, 2011). A blackbody in thermal equilibrium radiates according to Planck's law. The wavelength λ of maximum spectral radiance of a blackbody decreases with increasing temperature and can be calculated from the division of a constant $C = 2.898 \times 10^{-3} \text{ m} \cdot \text{K}$ by temperature T , as described by Wien's displacement law:

$$\lambda_{\max} = \frac{C}{T} \quad (5)$$

Most materials are not perfect blackbodies, however, and instead reflect or transmit some radiation through molecular interactions based on their physiochemical makeup (Figure 3). The spectral emissivity ϵ of a material is the ratio of the spectral radiance $L_{\lambda}(\text{material})$ to that of a blackbody $L_{\lambda}(\text{blackbody})$ at the same temperature (van der Meer & de Jong, 2011).

$$\epsilon_{\lambda} = \frac{L_{\lambda}(\text{material})}{L_{\lambda}(\text{blackbody})} \quad (6)$$

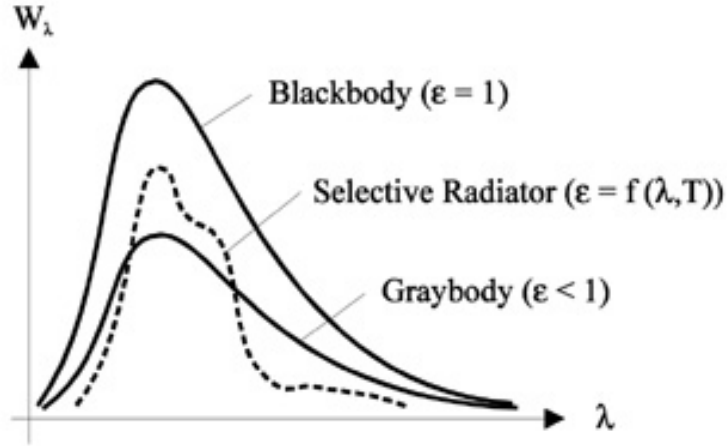


Figure 3. Comparison of Blackbody, Graybody, and Selective Radiator (from Riedl, 2001).

The majority of materials have emissivity values between 0.9 and 1.0, although certain minerals do have lower emissivity values (van der Meer & de Jong, 2011). An important feature that occurs in the LWIR spectral region is commonly called the Reststrahlen effect. At the reststrahlen maximum frequency of a particular material, the reflectance of the material increases sharply causing low emissivity features. An example of a well-known reststrahlen band is that for quartz near 9 micrometers, where an intense emissivity minimum appears due to the vibrational stretching of Si-O bonds (Lyon, 1964; van der Meer & de Jong, 2011; Vincent & Thomson, 1972). Other silicate minerals have features between 8 and 12 micrometers depending on silica concentration and characteristics of the silicate bonds. Sulfates, phosphates, oxides, and hydroxides also exhibit strong features in the LWIR.

Because the perfect blackbody by definition has an emissivity of 1.0, the only additional factor that contributes to the radiance of the observed material is temperature. The relationship between temperature, emissivity, and the location of the radiance peak with respect to total power can be explained by the Stephan-Boltzmann law. Total power S is defined by emissivity ϵ , a constant $\sigma = 5.669 \times 10^{-8} \frac{W \cdot m^2}{K^4}$, and temperature T of the object being measured.

$$S = \epsilon \sigma T^4 \quad (7)$$

The quintessential relationship between emissivity and reflectance can be explained by Kirchoff's law, where ε is emissivity and ρ is reflectance.

$$\varepsilon = 1 - \rho \quad (8)$$

C. REMOTE SENSING

Remote sensing is the science of acquiring information about an object of interest without actual physical contact with the object (van der Meer & de Jong, 2011). Advantages of using remote sensing techniques rather than in situ methods include obtaining wide-area coverage, avoiding regional hazards, and retaining minimal disturbances. Remote sensing data can be acquired by ground-based, airborne, and space-based platforms (Campbell, 2002).

The two primary remote sensing operational modes are active and passive (Elachi, 1987). Active remote sensing technologies require a self-generated signal from a radiation source. Examples of active methods include Radio Detection and Ranging (RADAR), Light Detection and Ranging (LiDAR), and Sound Navigation and Ranging (SONAR). Passive remote sensing does not require a self-generated signal, energy, or radiation to achieve a measurement. The primary passive remote sensing technology is electro-optical (EO) imaging, which is the primary focus of this thesis.

Various regions of the EM spectrum can be exploited to obtain information desired from EO imagery. EO systems covering the full spectral range of the EM spectrum initially record radiance measurements. The radiance values are later converted to either reflectance or emissivity after evaluating atmosphere influences. The commonality of units enables analysis and characterization of the full range of the spectrum.

Reflected solar radiation can be detected and measured in the VNIR to SWIR EM regions (Richards & Jia, 2013). Depending on the spatial resolution of the sensor, VNIR imagery can provide structural information about buildings, city layouts, traffic patterns, and general ways of life. Both VNIR and SWIR imagery can provide information about the composition of materials. LWIR imagery can provide information about the surface materials' composition and temperature properties (Richards & Jia, 2013).

Within the EO imaging subset of the remote sensing discipline, finer areas of study can be defined such as multispectral imaging (MSI) and imaging spectrometry. MSI is widely understood as subdividing selected spectral ranges into broad spectral intervals, producing images that show varying spectral response for surface materials (Goetz, 2009). The usual spectral width is on the order of hundreds of nanometers and sensors have a limited number of bands, nominally four to sixteen. In comparison, imaging spectrometry sensors have narrow contiguous spectral bands with widths on the order of tens of nanometers (Goetz et al., 1985). The narrower bands provide higher spectral resolution and include significantly more spectral channels compared to MSI sensors allowing identification rather than discrimination of materials.

1. Imaging Spectrometry

Imaging spectrometry, also known as hyperspectral imaging (HSI), acquires images in a large number of narrow, contiguous spectral bands (Figure 4). Hyperspectral refers to the multidimensional character of spectral data. Goetz et al. (1985) formally defined imaging spectrometry as “the acquisition of images in many narrow contiguous spectral bands throughout the visible and solar-reflected infrared” portions of the electromagnetic spectrum (p. 1147). Although the lexicon has diverse meanings, the community regards this technique as “the acquisition of images in hundreds of registered, contiguous spectral bands such that for each picture element of an image it is possible to derive a complete reflective spectrum,” (Goetz, 1992, p. 547). The greater number of bands enables more accurate measurements of physical quantities at the Earth’s surface, such as upwelling radiance, reflectance, emissivity, and temperature (van der Meer & de Jong, 2011). The ability to identify materials using HSI differs from MSI systems because the band widths are narrower and more closely spaced (Figures 4 and 5).

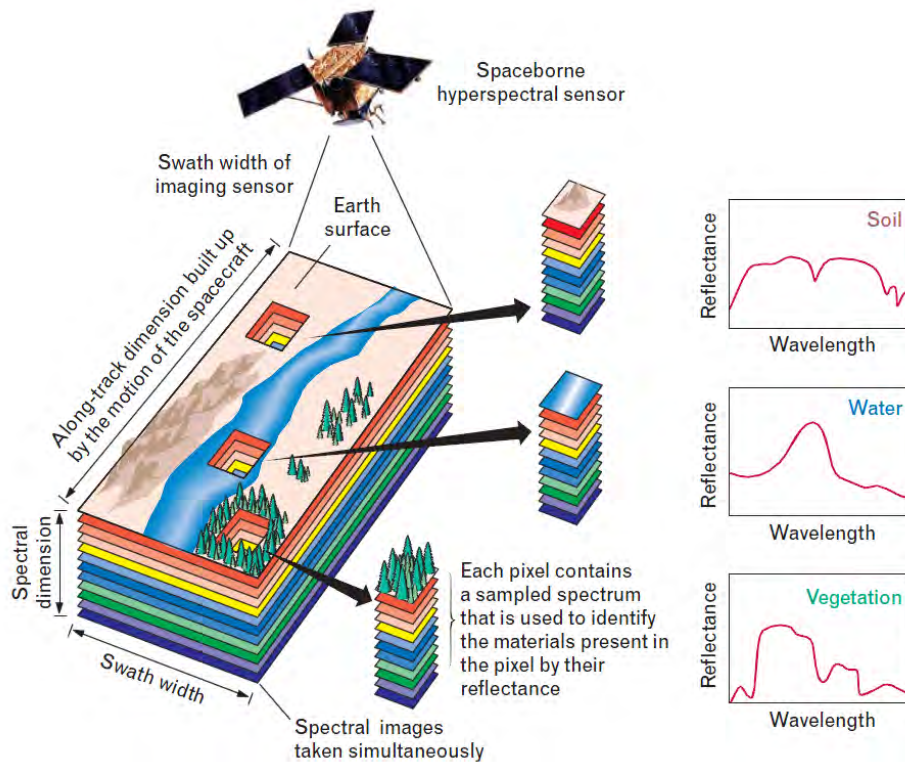


Figure 4. The imaging spectroscopy concept includes an imaging sensor with a large number of narrow and contiguous spectral bands (from Shaw & Burke, 2003).

The high spectral resolution of imaging spectrometers allows the data to be self-reducing and for atmospheric and solar effects to be removed for direct comparison with spectra measured in the field or in a laboratory setting (van der Meer & de Jong, 2011). High spectral resolution also aids in separating subtle material differences, allowing identification in addition to discrimination of surface materials (Figure 5). Multispectral systems with higher spatial resolution, but coarser spectral resolution lose the ability to distinguish and map fine spectral detail.

Spectral Signature in HSI data vs. MSI data

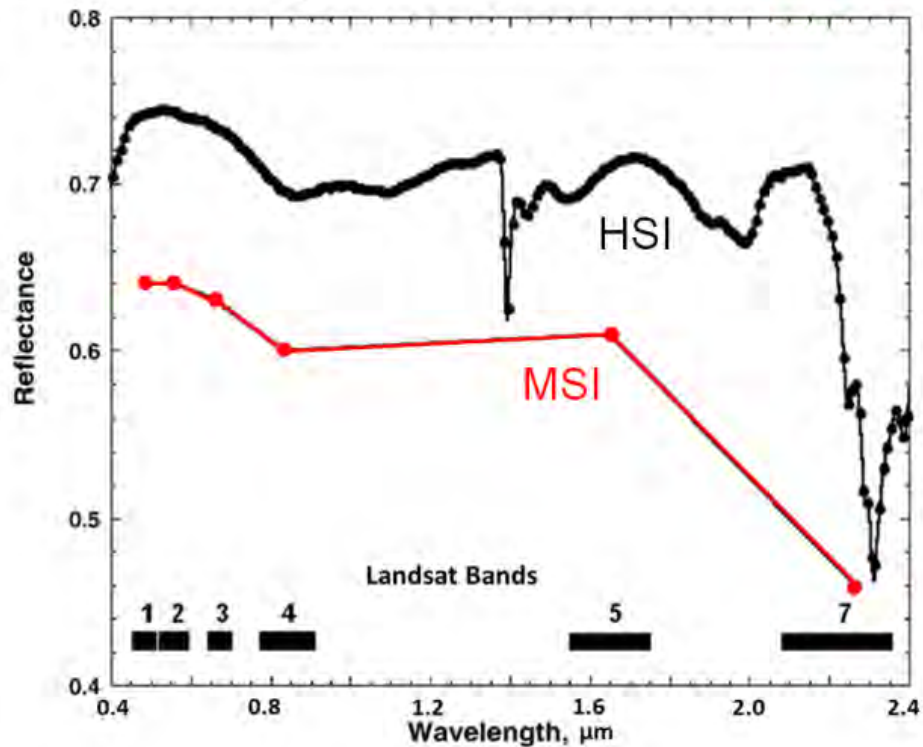


Figure 5. Comparison of spectral resolution of HSI and MSI data (from Goetz, 2009).

Hyperspectral imaging has many diverse applications, which can be grouped into three main categories: anomaly detection, target recognition, and background characterization (Figure 6). Anomaly detection separates pixels into man-made objects or natural features, target recognition provides detection and classification parameters of potential targets, and background characterization identifies the condition of natural features associated with land, ocean, or the atmosphere (Shaw & Burke, 2003).

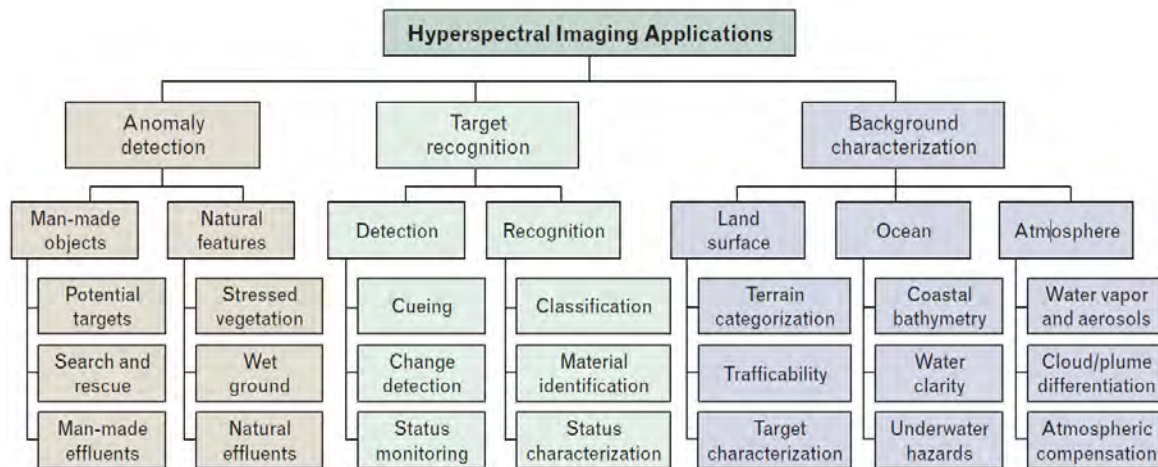


Figure 6. Hyperspectral Imaging Applications (from Shaw & Burke, 2003).

2. Atmospheric Effects

Primary effects caused by the atmosphere with regard to EO remote sensing of the Earth's surface include absorption, scattering, and turbulence. Atmospheric absorption is caused by atomic and molecular interactions of the gases present in the atmosphere, commonly water vapor, carbon dioxide, and ozone, with the surface-leaving radiance (Olsen, 2014) (Figures 7 and 8). The water vapor features in the SWIR region of the EM spectrum are commonly found at approximately 1.4 and 1.9 micrometers. In these regions, all energy is absorbed by the atmosphere and no remote sensing data can be obtained from the ground surface. Similar water vapor, carbon dioxide, and ozone features define the atmospheric windows for other portions of the EMR spectrum, including those near 2.5, 4.4, between 5 and 8 micrometers, and longward of 14 micrometers (Figures 7 and 8).

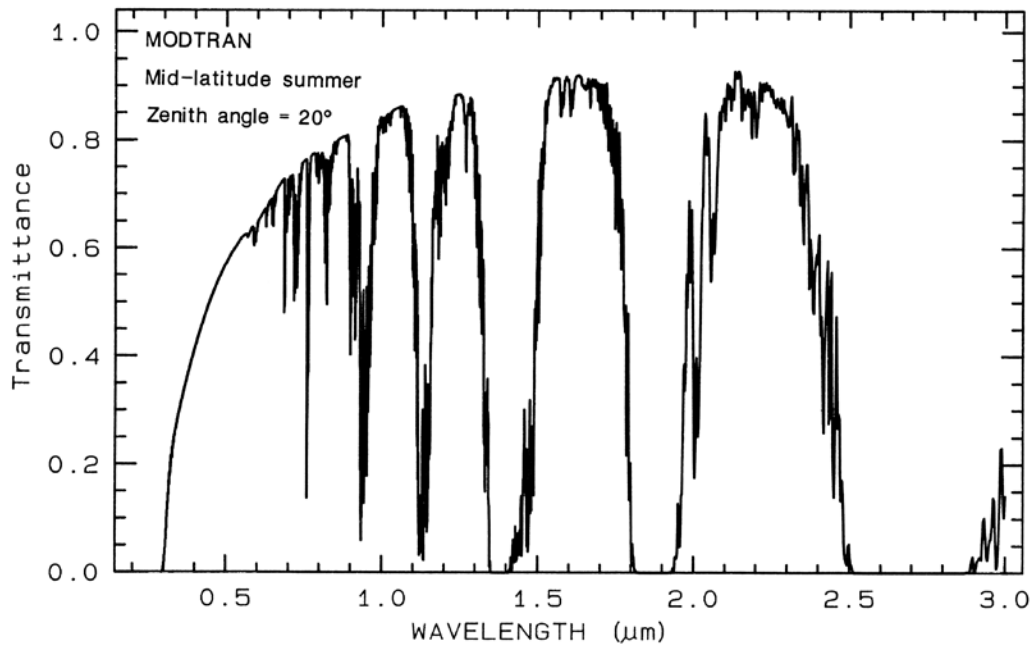


Figure 7. Atmospheric Transmission Plot of VNIR-SWIR
(from Berk et al., 1989).

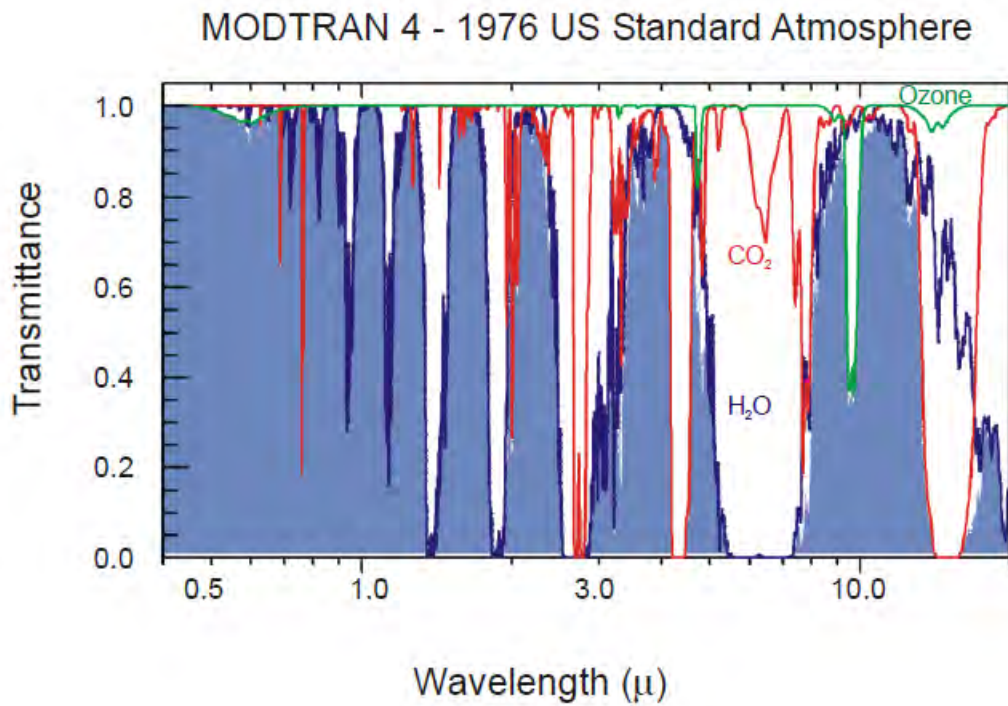


Figure 8. MODTRAN Plot displaying atmospheric transmission bands
(from Olsen, 2014).

Scattering is caused by collisions between the photons and scattering agents that include molecules, suspended particles, and clouds (Olsen, 2014). Rayleigh, Mie, and Nonselective scattering differ based on the relationship between wavelength and size of the scattering agent (Figure 9). Rayleigh scattering, commonly referred to as molecular scattering, is typically caused by oxygen and nitrogen molecules whose diameters are significantly smaller than the wavelength being scattered (Olsen, 2014). Mie scattering primarily is caused by larger size particles such as water vapor and small dust particles. Nonselective scattering is independent to wavelength because the size of the particles in the atmosphere is larger than the wavelength (Olsen, 2014). Common particles contributing to nonselective scattering are large raindrops and dust particles.

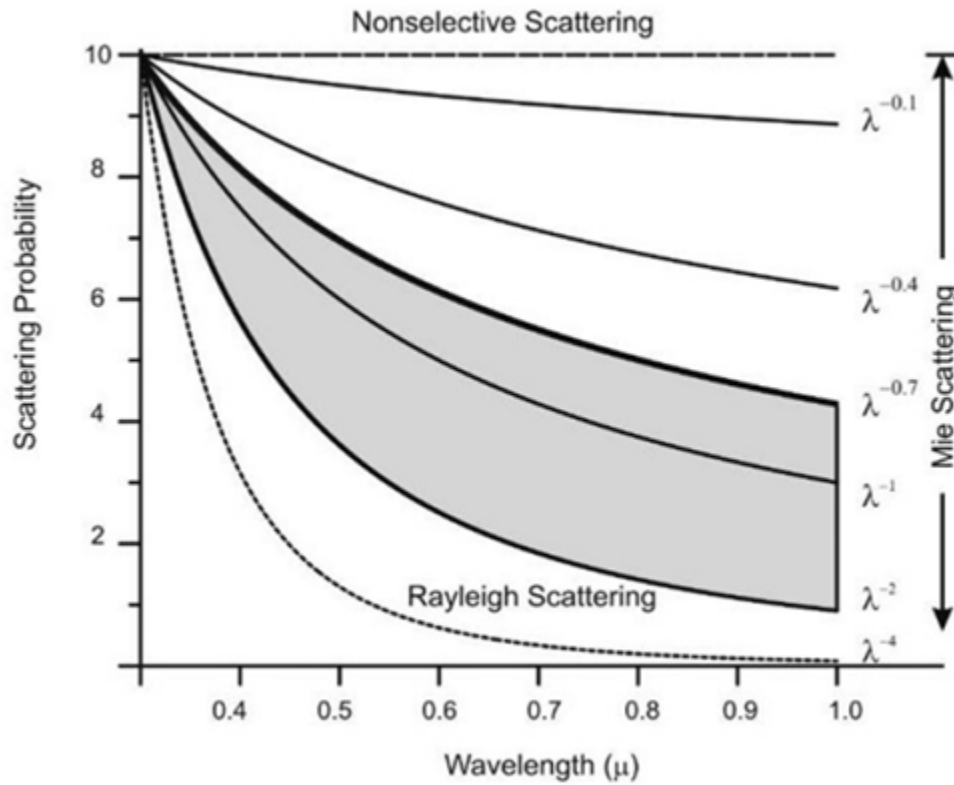


Figure 9. Atmospheric scattering effects caused by the size of the scattering agent (from Olsen, 2014).

The last environmental effect that limits the obtainable resolution with an imaging system is turbulence. Turbulence is caused by fluctuations in the temperature and density of the atmosphere (Olsen, 2014).

D. PREVIOUS WORK: FULL-RANGE SPECTRAL ANALYSIS

Spectral imagery is commonly analyzed and characterized separately as either VNIR-SWIR using reflectance or LWIR using emission, even though the spectral information provided tends to be complementary (Hook, Abbott, Grove, Kahle, & Palluconi, 1999).

An early exception is shown in the work by Abrams, Abbott, and Kahle (1991), a study that combined VNIR-SWIR and LWIR MSI information to map lava flows in Hawaii. The NS-001 sensor collected eight spectral channels covering the visible, infrared, and thermal infrared regions of the EM spectrum with eight meter pixels, and was processed using principal components transformation to reduce dimensionality. The Thermal Infrared Multispectral Scanner (TIMS) collected six spectral channels between 8 to 12 micrometers with an angular resolution of 2.5 milliradians and was processed using a decorrelation stretch to distinguish color differences within the image. The VNIR-SWIR data were sensitive to presences of iron oxides, brightness of the flow, and surface vegetation variation. The LWIR data were sensitive to surfaces containing silica and detecting younger lava flows. The combined dataset was processed using principal component analysis (PCA), which provided evidence that the VNIR-SWIR and LWIR data were correlated and not independent. Image color variations were used to distinguish relative ages of the flows. Overall, it was found that the combined data exposed more information compared to the separated analysis. This work combined a relatively small number of bands at fairly coarse spatial resolution for analysis. Obtaining smaller pixels may have improved results and using HSI instruments instead of MSI would have provided higher spectral resolution leading to quantitative results and identification of the variations of lava flows.

Cudahy, et al. (2001) also investigated the benefits of complementary VNIR-SWIR-LWIR data. This study used VNIR-SWIR Hyperspectral Mapping (HyMap) data

and LWIR Spatially Enhanced Broadband Array Spectrograph System (SEBASS) data to analyze variations of minerals near Yerington, Nevada. Both datasets were independently calibrated to radiance and atmospherically corrected. It was hypothesized that full spectral analysis would improve mapping of iron oxides, oxyhydroxides, both OH-bearing and non-OH-bearing silicates, carbonates, sulfates, and phosphates. The study concluded that separately, VNIR-SWIR and LWIR were able to map calcite, dolomite, amphibole, and epidote. The VNIR-SWIR data were sensitive to chlorite and overall abundance levels of mica minerals. The LWIR data were sensitive to garnet and plagioclase feldspar. The VNIR-SWIR and LWIR data were not combined, but the authors suggested that full spectral coverage would provide complementary information about the mineralogical and mineral chemistry patterns. The separate analysis of the overlapping images was the first step in analyzing full spectral coverage. Future work was proposed to combine the HSI bands to analyze variations in the results to quantitatively and effectively map the surface.

Kruse (2002) combined MSI SWIR and LWIR data to map minerals associated with hot springs and epithermal mineral deposits from sites around the world containing both active and fossil hot springs. The study used data obtained from the Advanced Spaceborne Thermal Emission and Reflection Radiometer (ASTER) and the MODIS/ASTER Airborne Simulator (MASTER). The ASTER sensor spans from approximately 0.55 to 11.3 micrometers and has three spectral bands in the VNIR with 15 meter resolution, six bands in the SWIR with 30 meter resolution, and five bands in the LWIR with 90 meter resolution. (Yamaguchi, Kahle, Tsu, Kawakami, & Pniel, 1998; Kruse, 2002) The MASTER sensor has 50 spectral bands ranging from 0.4 to 13 micrometers; 11 bands cover the VNIR, 14 bands cover the SWIR, and 25 bands cover the LWIR (Hook, Myers, Thome, Fitzgerald, & Kahle, 2001; Kruse, 2002). The VNIR-SWIR data were atmospherically corrected and converted to reflectance and the LWIR data were atmospherically corrected and converted to temperature and emissivity (Kruse, 2002). Only the SWIR and LWIR bands were analyzed. The SWIR and LWIR data were analyzed separately using the same overall processing flow to include using a linear transformation of the reflectance or emissivity data to minimize noise and data

dimensionality, identifying purest pixels, extracting endmember spectra, and spatially mapping specific image endmembers. The SWIR region mapped carbonates, kaolinite, alunite, buddingtonite, muscovite, and hydrothermal silica, while the LWIR region only detected siliceous sinter. The identification of minerals was supplemented with ground truth and library spectra. The integration of the datasets was not completed at the time of publication, but the hypothesis for future research was that refined maps showing the distribution of key minerals associated with hot springs and epithermal mineral deposits would be possible using combined VNIR-SWIR-LWIR. In addition to integrating the datasets an improvement to the work would be to include an additional HSI dataset to refine identification of key features in addition to using ground and library spectra for comparison with ASTER and MASTER spectra.

Vaughan and Calvin (2004) integrated HSI VNIR-SWIR-LWIR data collected by the HyperSpecTIR (HST) spectrometer and SEBASS to explore environmental hazards and precious metals found in the Comstock mining district around Virginia City, Nevada. The HST, developed by Spectral Technology and Innovative Research Corporation (SpecTIR), measured solar reflected radiance between 0.45 and 2.45 micrometers in 227 continuous channels (Vaughan & Calvin, 2004). The VNIR-SWIR images had a spatial resolution of 2.5 meters and were acquired in a series of overlapping frames rather than a single, continuous strip. The SEBASS data had a spatial resolution of 2 meters. Both data ranges were independently atmospherically corrected. The VNIR-SWIR data were converted to reflectance and the LWIR data were converted to emissivity. A similar processing scheme as described in the Kruse (2002) study was implemented to focus on the information necessary to characterize mineral features within the image. Clay minerals were more clearly identified by the VNIR-SWIR spectra and the LWIR image spectra excelled in identifying hydrous sulfate phases. Most interestingly, minerals that could not conclusively be identified with one spectral range could be identifying using a combination of VNIR-SWIR and LWIR HSI data, specifically the differentiation of jarosite and hydrous sulfate (Figure 10).

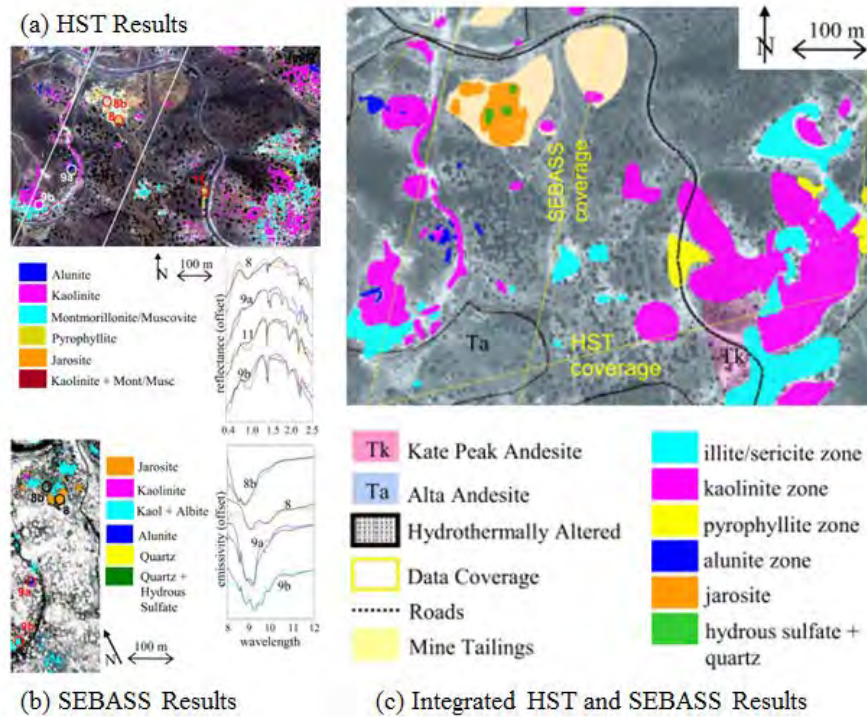


Figure 10. Mineral maps of Comstock mining district around Virginia City, Nevada (from Vaughan & Calvin, 2004).

Chen, Warner, and Campagna (2007) explored the possibilities of integrating the full spectral range for geological mapping of the canonical Cuprite, Nevada site. This experiment combined data from the Airborne Visible/Infrared Imaging Spectrometer (AVIRIS) and the MASTER sensor to examine if the integrated dataset would provide improved lithologic mapping. AVIRIS measures the solar reflected spectrum from 0.4 to 2.5 micrometers, with 224 contiguous spectral channels at 10 nanometer intervals across the spectrum (Green et al., 1998). This study focused on HSI VNIR-SWIR and MSI LWIR because at the time of the study it was difficult to obtain HSI LWIR imagery, while MSI imagery was widely available and provided sufficient geological information (Chen, Warner, & Campagna, 2007). The AVIRIS and MASTER data were separately geo-referenced and converted from radiance to reflectance and emissivity, respectively. Classification and identification were performed using two statistical classification methods, minimum distance and maximum likelihood, as well as two spectral classification methods, spectral angle mapper (SAM) and spectral feature fitting (SFF).

The combined data mapped using SAM provided the most accurate results, as determined by the calculated Kappa coefficients for each wavelength region (Figure 11). Overall, improvements in most of the classification results were seen with the integrated VNIR-SWIR and LWIR data compared to the AVIRIS and MASTER data alone.

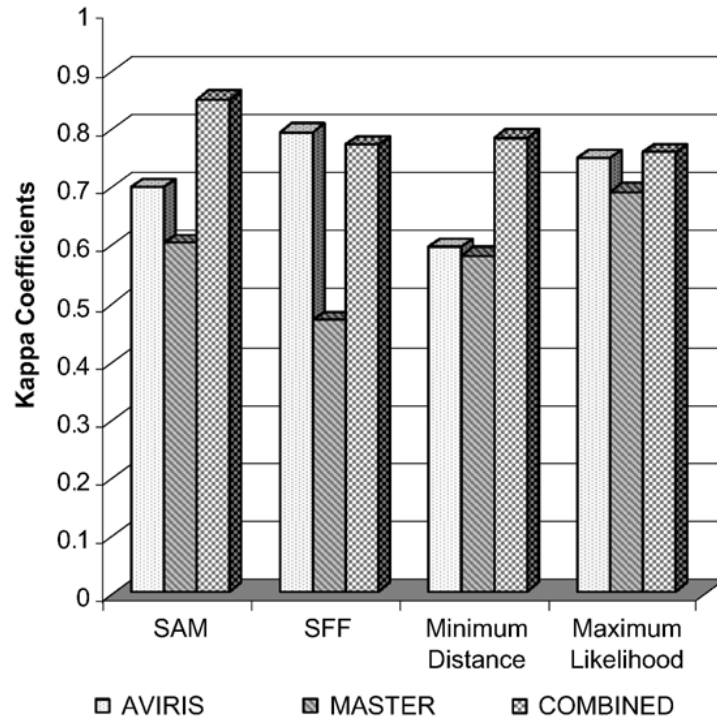


Figure 11. The results from study conducted by Chen, et al. (2007) to determine the advantage of using combined wavelength datasets.

In a continuing effort to improve classification results Chen, Warner, and Campagna (2010) further explored classification methods by implementing a hybrid algorithm exploiting the strengths of SAM classification and SFF. The new expert system achieved a notably higher performance than the SAM, SFF, minimum distance, and maximum likelihood classification methods did on their own. An improvement to the study would have been to use HSI LWIR rather than MSI. The increase in number of LWIR bands would, however, likely complicate the methods of combining the datasets. Inclusion of ground truth would have also confirmed the results and accuracy of their classification approach.

Warner and Nerry (2009) combined HSI VNIR-SWIR data with MSI LWIR to explore urban land-cover classification of Strasbourg, France. Support vector machine classification was used to analyze the data. The imagery was taken with the Digital Airborne Imaging Spectrometer (DAIS), which has 79 spectral channels: 72 bands covering the VNIR-SWIR, 1 band in the MWIR, and 6 MSI bands in the LWIR. The VNIR-SWIR bands were converted to reflectance and atmospherically corrected. The LWIR bands were recalibrated using ground measurements to separate temperature and emissivity. Ground reference data was obtained from high-resolution orthophotography and used to create eight training classes. Various band combinations were analyzed, new regions of interests were created, and an accuracy parameter was calculated. The accuracy score calculated using the HSI VNIR-SWIR bands for classification was high. Interestingly, the accuracy of using only the MSI LWIR bands was also high. The inclusion of a single, broad thermal band increased the accuracy and indicated that variance in surface temperatures is useful in distinguishing between classes. This was further proven when the accuracy parameter increased approximately 10% when including all LWIR bands. Specifically, railway, roof, and road-asphalt became distinguishable when the LWIR bands were included in analysis because their spectra differed in the LWIR, but were too similar for discrimination when only using spectral information in the VNIR-SWIR region. This study was interesting because it provided evidence of the usefulness of full spectrum analysis beyond geological applications. Improvements and future work include HIS rather than MSI bands to identify more endmembers in the scene.

The National Research Council (NRC) (2007) introduced the Hyperspectral Infrared Imager (HyspIRI) satellite proposed by the National Aeronautics and Space Administration (NASA). The HyspIRI remote sensing payload will be composed of two instruments that will combine over 200 VNIR and SWIR hyperspectral channels ranging from 0.38 to 2.5 micrometers with eight thermal MSI bands. Analysis of simulated VNIR-SWIR-LWIR HyspIRI data using AVIRIS and MASTER data by Kruse et al. (2011) suggests that HyspIRI will be useful for many geologic applications. The simulated data were resampled using the proposed HyspIRI band passes. The VNIR-

SWIR and LWIR datasets were individually atmospherically corrected and converted to reflectance and emissivity, respectfully. The VNIR-SWIR and LWIR data were analyzed separately to extract endmembers and compared to library spectra for identification. The simulated datasets were used to successfully identify and map minerals such as goethite, hematite, jarosite, kaolinite, dickite, alunite, buddingtonite, montmorillonite, muscovite-illite, calcite, and hydrothermal silica. The MSI LWIR results were similar to ASTER, allowing minerals rich in silica to be detected. The surface temperatures obtained from the LWIR data were also used to identify active hot springs areas. The coarse HypsIRI spatial resolution of 60 meters limited the detection of some occurrences and details compared to airborne data. The proposed spaceborne sensor will provide larger coverage area and is predicted to measure geothermal and hydrothermal systems. Future work will include additional test sites and refinement of simulations.

E. HYPERSENSPECTRAL SENSORS, DATA SET, AND STUDY SITE

The hyperspectral data used for full-range spectral analysis for the purposes of this thesis were acquired using the MaRSuper Sensor System (MSS-1) covering the VNIR-SWIR wavelength regions and SEBASS covering the LWIR wavelength region.

1. Hyperspectral Sensors

a. VNIR-SWIR Sensor

The precursor to MSS-1, the Mapping Reflected-energy Sensor (MaRS) was developed by JPL in the mid-2000s as the next generation AVIRIS system. The sensor system used 332 spectral channels to cover the solar reflective spectral region ranging from 0.38 to 2.5 micrometers with high spectral resolution (Simi & Olchowski, 2009). A low-distortion Offner spectrometer provided high optical throughput, allowing high SNR over the full spectrum (Figure 12). The MaRS was first flown in May 2005 at Ivanpah Playa in Nevada to perform both functionality testing and radiometric verification (Simi & Olchowski, 2009). Additional MaRS collect locations included Cuprite, Nevada in March 2007 to investigate surface texture information, and Washington, DC, in August 2008 to investigate species variability (Simi & Olchowski, 2009).

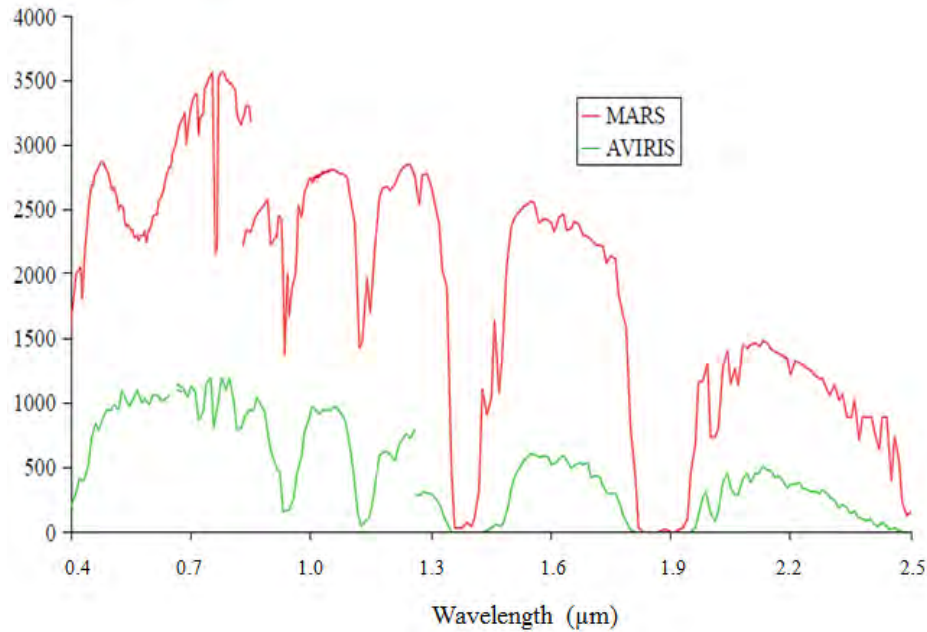


Figure 12. Signal-to-noise ratio comparison of MaRS to 2004 AVIRIS (after Simi & Olchowski, 2009).

The MSS series was developed as an improved MaRS. The MSS-1 sensor used for this study is a Northrop Grumman Integrated Systems pushbroom sensor with a high-magnification telescope. The MSS-1 collected solar radiance in the VNIR-SWIR spectral regions ranging from 0.38 to 2.5 micrometers using over 400 spectral channels. This HSI sensor had a spectral resolution of approximately five nanometers. The pixel size for the dataset of interest for this study was approximately 0.65 meters. The sensor was cooled using a cryocooler device capable of cooling to 140°K without using liquid nitrogen and utilized an on-board calibrator. Four MSS sensors make up the fleet, and the sensors have successfully carried out diverse missions. One advantage of MSS-1 is the higher signal-to-noise ratio (SNR) output compared to both MaRS and AVIRIS sensors.

b. LWIR Sensor

The LWIR data used for this study were collected using the SEBASS sensor. The imaging spectrometer was built by the Aerospace Corporation and first flown in October 1995 (Hackwell et al., 1996). The original intent of SEBASS was to be able to remotely

identify solids, liquids, gases, and chemical vapors in the 2 to 14 micrometer “chemical fingerprint” spectral region.

The SEBASS is a pushbroom scanner with high signal-to-noise ratio (SNR) capable of measuring an instantaneous field of view of 1.1 milliradians (Wright, Riley, Peppin, & Schulenburg, 2008; Kirkland et al., 2002). The sensor collects 256 spectral channels with varying spatial resolution depending on the flight altitude (Wright et al., 2008). The spectral channels consist of 128 MWIR bands ranging from 2.5 to 5.3 micrometers and 128 LWIR bands ranging from 7.6 to 13.5 micrometers. The SNR remains high because the optical bench is cooled to 4°K using liquid helium which increases the sensitivity of the sensor (Kirkland et al., 2002). Typically, SEBASS produces LWIR hyperspectral images that are 128 pixels wide and approximately 2000 pixels long.

Some of the prominent applications of SEBASS include target detection, mapping atmospheric variations, geological mapping, and environmental monitoring. Spectra obtained by SEBASS can be compared with laboratory emissivity spectra to identify surface materials (Figure 13).

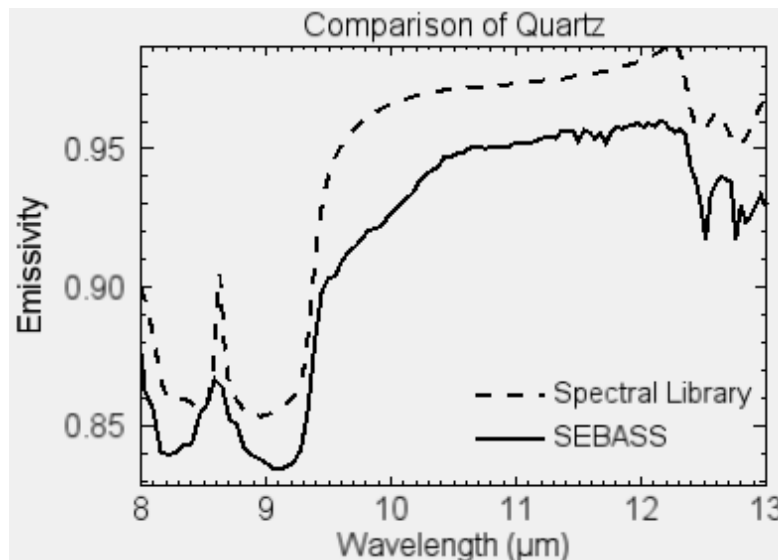


Figure 13. Comparison of SEBASS emissivity spectrum (hydrothermal silica, Cuprite, NV) and laboratory spectrum of quartz (JHU Minerals Emissivity spectral library).

2. Study Site

The study site for this research is a small, selected portion of the Nevada National Security Site (NNSS). The NNSS is located approximately 65 miles northwest of Las Vegas, Nevada. The site is a rural desert area and was chosen for this work because of the uniform background and unique targets.

The NNSS was originally created in the 1950s under the Truman administration to provide a desolate area for atmospheric nuclear tests and research. A total of 100 atmospheric tests were conducted at the site until all atmospheric testing was banned on August 5, 1963 when the Limited Test Ban treaty was signed in Moscow (Fehner & Gosling, 2000). After the treaty was signed, 928 full-scale nuclear tests were conducted underground. All full-scale nuclear testing ended in 1992 when the U.S. entered into the Comprehensive Nuclear Test Ban with Russia and France (Fehner & Gosling, 2000). Presently, NNSS has become the United States' principal area for nuclear/radiological testing, training, and emergency response in support of Homeland Security.

3. Data Sets

Imagery used for this research cover a selected portion of the NNSS (Figure 14). The VNIR-SWIR MSS-1 data were acquired on August 20, 2013, with approximately 0.65 meter spatial resolution. The LWIR SEBASS data were collected on September 16th, 2013, with approximately 0.86 meter spatial resolution. MSS-1 covered a larger area compared to SEBASS. Figure 14 shows the data coverage. Co-registered, geometrically corrected images illustrating coincident coverage for the VNIR-SWIR and LWIR are used for integrated analysis and are shown later in this thesis.

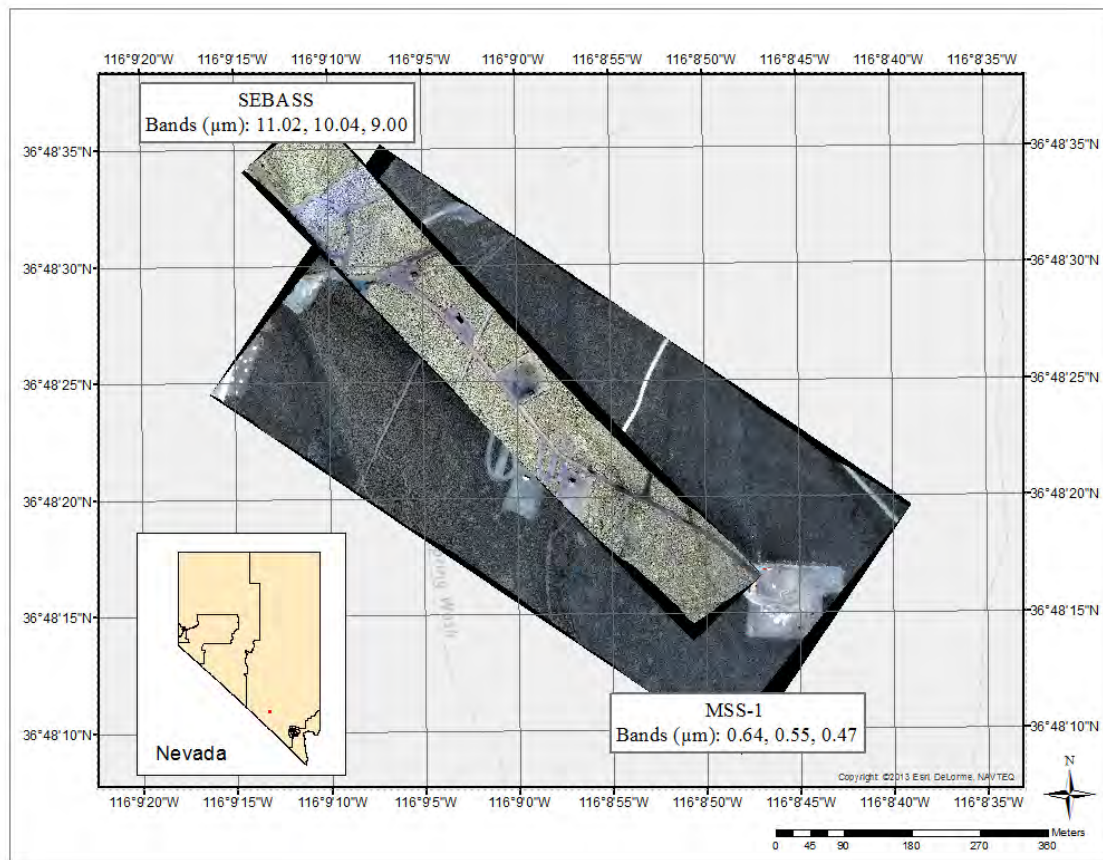


Figure 14. MSS-1 and SEBASS georeferenced (not registered) coverage area of the NNSS location.

III. APPROACH AND METHODS

Imaging spectrometer data must be spectrally, radiometrically, and geometrically calibrated in order to derive physical parameters including reflectance, emissivity, temperature, and water vapor. The VNIR-SWIR and LWIR data were atmospherically corrected separately and then geometrically corrected to cover the same area. Once all corrections were finalized two methods of integration were examined and compared to a standard baseline processing scheme utilizing the individual spectral regions to characterize and map the VNIR, SWIR, and LWIR data.

A. VNIR-SWIR DATA PREPARATION

The MSS-1 VNIR-SWIR data used for this thesis work were first prepared for analysis by removing vertical line artifacts from the image using a destriping algorithm. Then, primary atmospheric influences were removed using a model-based approach to convert the calibrated radiance to reflectance. The model-based reflectance was further refined to remove instrument artifacts using ground spectral measurements. Lastly, the data were geometrically corrected by georeferencing the image to ground surveyed points.

1. Destriping

Vertical striping artifacts are common in hyperspectral pushbroom scanners, such as MSS-1. A radiometric correction algorithm is required to correct the variable calibration of the focal plane arrays, which results in vertical striping artifacts (Scheffler & Karrasch, 2014) (Figure 15). A common issue known as the keystone effect is caused by aberration or slight misalignments of the optical components in the sensor system (Scheffler & Karrasch, 2014). Co-calibration-registration issues can also be caused by using two or more spectrometer systems. Often the striping effects aren't apparent in standard color composite images and only become noticeable when a sharply contrast stretch is applied to the image or when spectral signatures are extracted. The striping artifacts are more apparent in transformed data spaces utilized to maximize data variance

(Figure 15). Ultimately the striping effects need to be eliminated so spectral analysis can be conducted and endmembers can be identified.

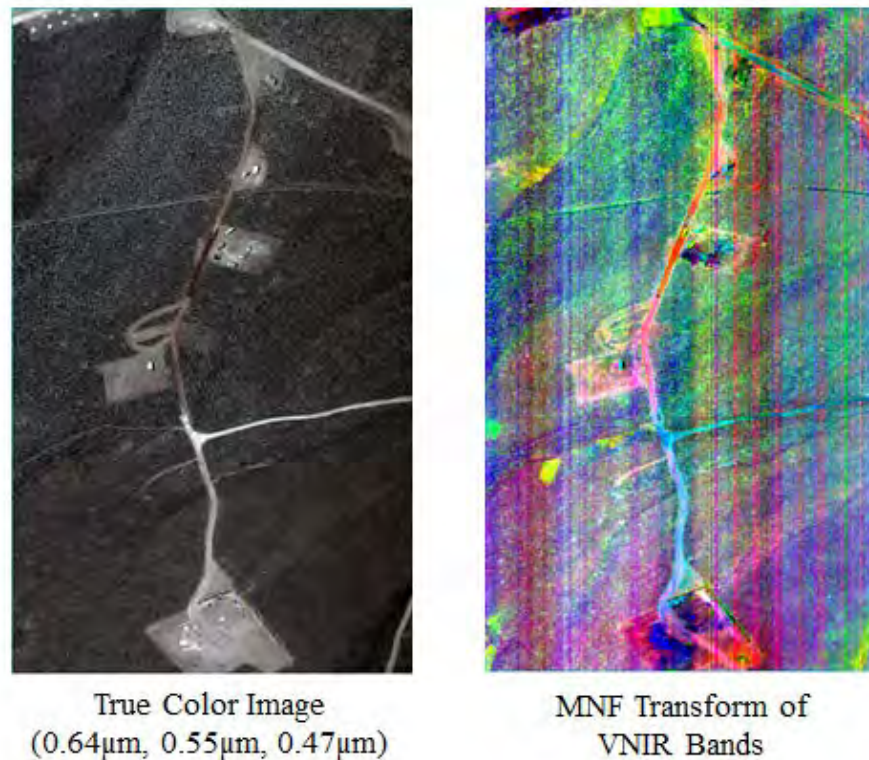


Figure 15. MSS-1 calibrated radiance true color image (left), MNF-transformed image (MNF Bands 1, 2, 3 as RGB) showing striping problems (right).

Two different algorithms were tested to remove the striping artifacts present in the MSS-1 imagery. First, the Spectral Processing Exploitation and Analysis Resource (SPEAR) Vertical Stripe Removal algorithm was applied using the Environment for Visualizing Images (ENVI) software interface (EXELIS, 2014). The SPEAR algorithm corrects for variations in brightness of pixels relative to other nearby pixels, as in striping artifacts. The algorithm is most effective on heterogeneous images (those with bright or dark areas, e.g., clouds and shadows). By default, the darkest and brightest 5% of the band is masked to aid in identifying the striping artifacts. For the specific image of interest, a mask of band 52 at 0.63 micrometers (red channel) was created using a lower bound of 5.00% and an upper bound of 95.00% to filter the bright and dark pixels. The

ability to manually exclude the darkest and brightest pixels in the image from the correction is unique compared to the general destriping algorithm available in ENVI (EXELIS, 2014).

Next, the Tactical Hyperspectral Operations Resource (THOR) De-Striping algorithm was applied using ENVI. This method presents an alternative for removing the vertical line artifacts by calculating the mean of the determined number of vertical lines or horizontal row samples and normalizing each one to its respective mean (EXELIS, 2014). Figure 16 presents a visual comparison of the THOR destriping method utilizing Minimum Noise Fraction (MNF) images to best emphasize the similarities and differences. A more thorough explanation of MNF will be provided in the analysis and integration chapter.

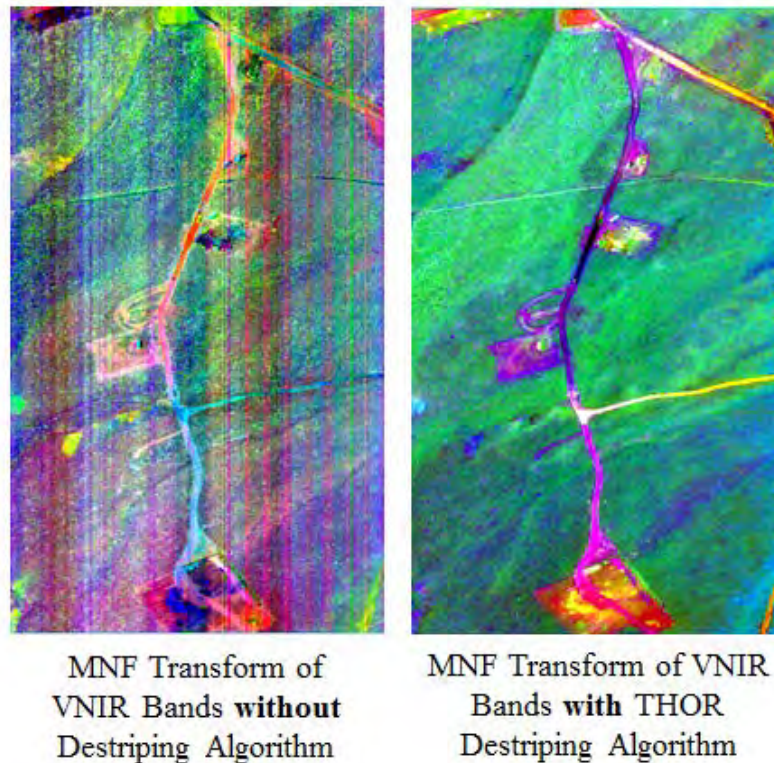


Figure 16. MNF-transformed image without destriping (left), MNF-transformed image with THOR destriping applied (right). MNF Bands 1, 2, 3 as RGB.

Both algorithms seem to work effectively on the lower MNF bands. Vertical stripe artifacts remain in the higher MNF bands, which isolate the noise content. In both methods the first MNF band highlighted a bright vertical stripe in the middle of the image (Figure 17). The THOR De-Striping algorithm displayed a smoother average of the artifact, while the line artifact appeared more prominent in SPEAR image against the dark background. This result was consistent in the majority of the non-noise MNF transformed bands. Moving forward, all analysis was performed on the THOR destriped image.

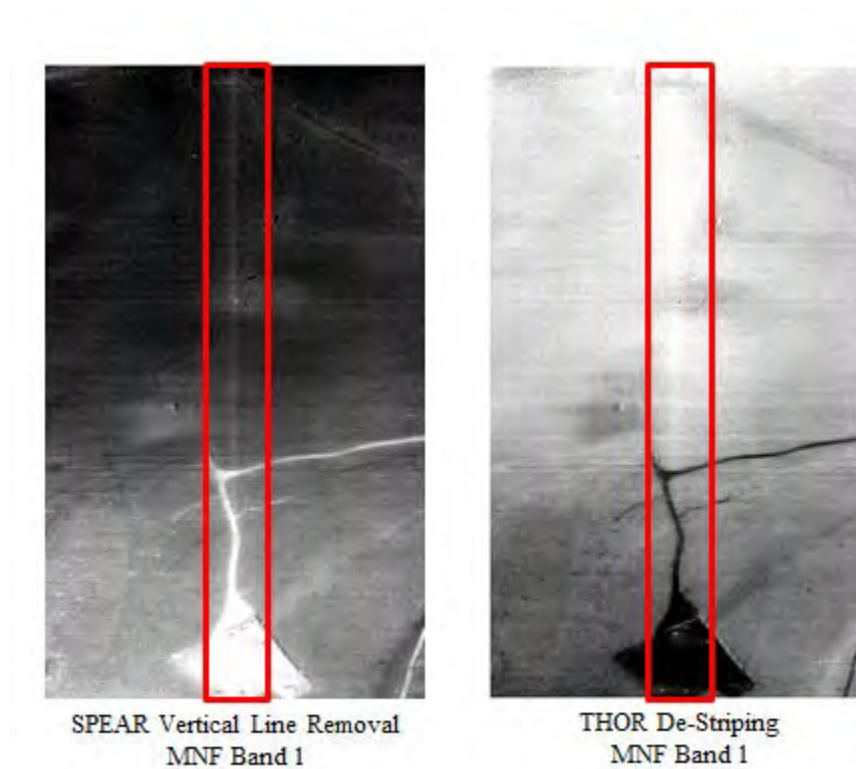


Figure 17. Comparison of Destriping: SPEAR Vertical Stripe Removal (left) and THOR De-Striping (right).

2. Atmospheric Correction

Atmospheric correction is required for comparing and analyzing HSI data with data acquired by other imaging instruments, spectrometers, or spectra generated by

system models. In addition, atmospheric correction is required to be able to compare spectra across time and space by transforming the calibrated radiance data to dimensionless reflectance data.

Several different methodologies have been developed to remove atmospheric influences and convert radiance to reflectance, including empirical and model-based algorithms. The objective of all correction methods is to remove atmospheric absorption and scattering effects, as well as the solar spectrum (Matthew et al., 2003). Empirical models based on in-scene parameters are appropriate to use when sensor calibration data is not available and when overall collection and model parameters are not available. Empirical methods tend to be less computationally demanding than model-based methods, resulting in faster returns (Bernstein, Jin, Gregor, & Adler-Golden, 2012). Empirical methods perform more approximate atmospheric correction compared to model-based approaches. Some statistical techniques include the internal average relative reflectance (IARR) method, which uses the mean radiance of all the pixels in the images as a correction factor to adjust raw radiance data, and the flat field correction (FFC), which assumes there is an area in the scene that is spectrally neutral (Clark et al., 2002; Griffin & Burke, 2003; Kruse, 1988). The Quick Atmospheric Correction (QUAC) is another common in-scene based approach that works with a variety of MSI and HSI VNIR-SWIR channels and provides absolute accuracy of approximately $\pm 15\%$ with respect to radiative transfer models (Bernstein et al., 2012). Empirical atmospheric correction can be used as a baseline for expected influences, but model based approaches that use sensor parameters, atmospheric models, aerosol models, and flight information calculate more accurate reflectance spectra.

Common model-based approaches in use for VNIR-SWIR imaging spectrometer data analysis include Atmospheric Removal (ATREM), Atmospheric Correction Now (ACORN), Atmospheric Correction (ATCOR), and Fast Line-of-sight Atmosphere Analysis of Spectral Hypercubes (FLAASH) (Gao, Heidebrecht, & Geotz, 1993; Griffin & Burke, 2003; Kruse, 2004; Matthew et al., 2003; Richter, 1996). These all are based on the use of the Moderate resolution atmospheric Transmission (MODTRAN) atmospheric radiative transfer code, which allows modeling of specific atmospheric parameters such

as water vapor, gas constituents, and scattering (Berk, Bernstein, & Robertson, 1987). All of the models require that the hyperspectral data be well calibrated and that certain information is known about the sensor, atmospheric parameters, and location.

This work tested and compared the empirical QUAC algorithm, the model-based FLAASH algorithm, and a hybrid approach that combines FLAASH and ground measurements.

a. Quick Atmospheric Correction

The QUAC method uses information from the scene to correct and remove atmospheric influences. The correction does not require user input or knowledge of sensor metadata and instead uses approximate specifications of sensor band locations and radiometric calibration (Bernstein et al., 2012). It is assumed that the average reflectance of material spectra is not dependent on each scene, allowing faster processing when compared to model-based methods (Bernstein et al., 2012). The algorithm calculates approximate reflectance spectra if the following two assumptions are met: the scene has at least 10 diverse materials and enough dark pixels to estimate the baseline spectrum. The results of QUAC will not worsen as sensor and measurement uncertainties increase because only in-scene information is being used in the algorithm (Bernstein et al., 2012). QUAC can be applied to MSI and HSI data covering all or part of the VNIR–SWIR spectral range (Bernstein et al., 2012). The data processing flow is illustrated in Figure 18.



Figure 18. Outline of QUAC data processing algorithm
(from Bernstein, Jin, Gregor, & Adler-Golden, 2012).

The QUAC algorithm was applied to the destriped MSS-1 VNIR-SWIR data to create a baseline for expected radiance and reflectance spectra. Figure 19 depicts the calibrated radiance and the QUAC-corrected reflectance spectrum of a single pixel located at position (335, 892) in the image. The QUAC method corrects for the major atmospheric water vapor bands near 1.4 and 1.9 micrometers, seen by the removal of data points near these regions (Figure 19). The 1.9 to 2.1 micrometer range is noisy, indicating that carbon dioxide influences remain in the QUAC-corrected spectrum (Griffin & Burke, 2003).

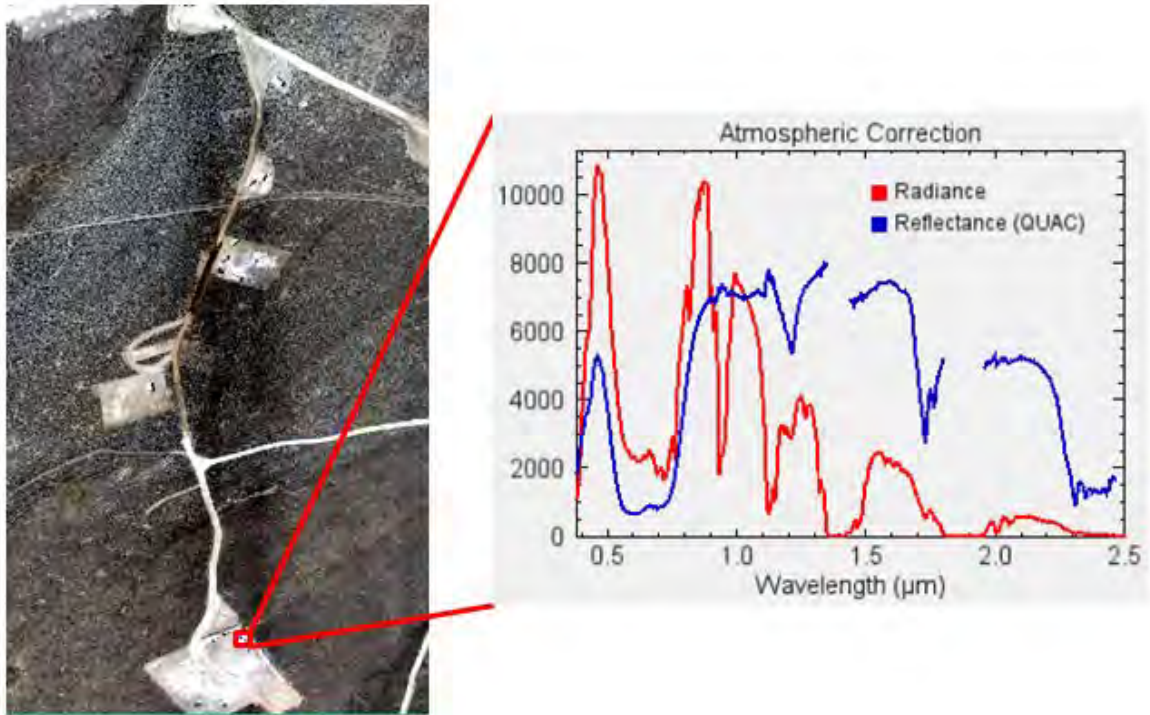


Figure 19. Comparison of the radiance and QUAC corrected reflectance spectra. QUAC corrected true color reflectance image (left). Radiance ($\mu W \cdot cm^{-2} \cdot sr^{-1} \cdot \mu m^{-1}$) spectrum and QUAC corrected reflectance (scaled from 0 to 10,000) spectrum of pixel (335, 892) (right).

b. Fast Line-of-Sight Atmosphere Analysis of Spectral Hypercubes

FLAASH was developed by Spectral Sciences, Inc., the Air Force Research Laboratory, and the Spectral Information Technical Applications Center (SITAC) and uses MODTRAN atmospheric models to make atmospheric corrections (Matthew et al., 2003). The FLAASH approach uses the physics-based model to apply atmospheric correction that uses flight and sensor metadata to include date, time, and location with assumed and measured atmospheric parameters to generate reflectance spectra from radiance data (Matthew et al., 2003).

FLAASH is available in the EXELIS ENVI software package (EXELIS, 2014). The model-based, or first-principles, atmospheric correction is carried out in three steps. The first step obtains atmospheric parameters to include an aerosol description and the

column water amount (Matthew et al., 2003). The second step in the correction converts the radiance data to reflectance and calculates the aerosol and column water vapor levels using the radiative transport equation. The FLAASH model has an option to compute average visibility from the amount of aerosol and haze present in the scene (Matthew et al., 2003). The MODTRAN-based algorithm is also capable of providing correction for the adjacency effect, which is caused by atmospheric scattering of surface-reflected radiance from pixels adjacent to the one being corrected. The final step in the process is spectral polishing to remove remaining artifacts from the spectra. FLAASH allows adjusting the thresholds for polishing to suppress artifacts. Spectral polishing uses only information from the image of interest to produce an atmospherically corrected HSI image with consistent spectra.

A scale factor of 1000 was applied to the MSS-1 calibrated radiance data for data scaling purposes. Additional parameters are listed in Table 1 specifying sensor and flight information and in Table 2 specifying FLAASH options that were used to analyze and compare the U.S. Standard and the Mid-Latitude Summer atmospheric models for the MSS-1 data. These models were chosen based on the scene temperature, date, and latitude.

Scene Center Location	Latitude: 36°48'21.68"
	Longitude: -116°8'56.96"
Sensor Altitude (km)	3.950
Ground Elevation (km)	1.150
Pixel Size (m)	0.655
Flight Date	August 20, 2013
Flight Time GMT	21:29:10

Table 1. Sensor Parameters for FLAASH

Water Retrieval	Yes
Water Absorption Feature	1.135 μm
Aerosol Mode	Rural
Aerosol Retrieval	2-Band (K-T)
Initial Visibility (km)	40.00
Spectral Polishing	Yes
Width (number of bands)	9
Wavelength Recalibration	No

Table 2. FLAASH Parameters

The U.S. Standard model did not accurately correct for the atmospheric conditions for these data and the model was assumed to be too general for the site location. Deep, broad absorptions features appeared near 0.9, 1.1, 1.4, and 1.9 micrometers indicating the presences of atmospheric water (Griffin & Burke, 2003). The reflectance spectra deviated only slightly when different water absorption features were used in the FLAASH algorithm to calculate atmospheric water vapor. The reflectance spectra drastically differ from the baseline QUAC results and no significant features can be detected (Figure 20).

The Mid-Latitude Summer model produced reflectance spectra with distinct features similar to the QUAC spectra (Figure 20). When using 0.820 micrometers as the water absorption feature for water vapor determination, the spectra do, however, overcompensate for atmospheric influences, especially the atmospheric water absorption bands near 1.4 and 1.9 micrometers. Corrections preformed on the 0.940 and 1.135 micrometers water absorption feature calculate nearly the same reflectance spectra, with less overcompensation compared to the 0.820 micrometers result. The carbon dioxide region is less noisy in the FLAASH spectra compared to the QUAC spectra.

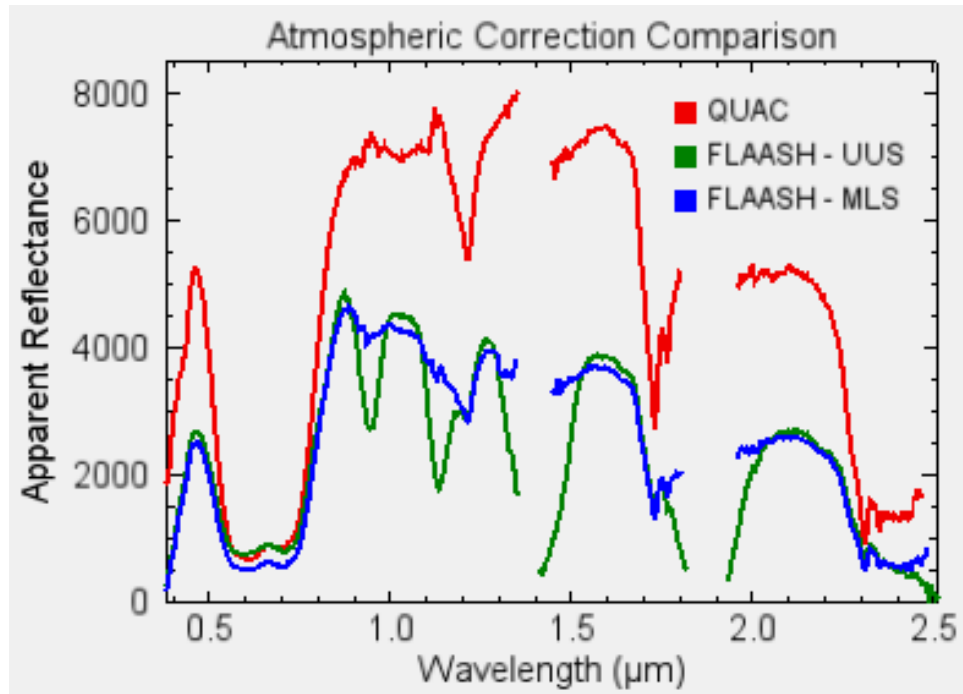


Figure 20. QUAC reflectance spectrum (red), FLAASH reflectance spectrum using U.S. Standard atmospheric model (green), FLAASH reflectance spectrum using Mid-Latitude Summer atmospheric model (blue). Spectra are representative of a single pixel located at (335,892).

The results obtained by applying the Mid-Latitude Summer atmospheric model, using the 1.135 micrometers water absorption feature, to the calibrated radiance data were used to further analyze cloud cover and column water vapor of the scene. Almost no cloud cover appears in these data (Figure 21), and only 12 pixels representing structural objects (i.e., building, car, etc.) returned water retrieval errors. The pixels resulting in water retrieval error had to be masked to accurately display the column water vapor of the scene (Figure 21). The column water vapor is displayed in units of centimeters multiplied by the atmospheric scale factor of 1000 (EXELIS, 2014). Purple to blue pixels show low water vapor, while red pixels show higher water vapor content. The bottom of the image shows less water vapor compared to the top of the image because the ground elevation is higher. Most of the road surface pixels show highest water vapor compared to the desert vegetation background because a special liquefied plastic coating has been applied to the surface.

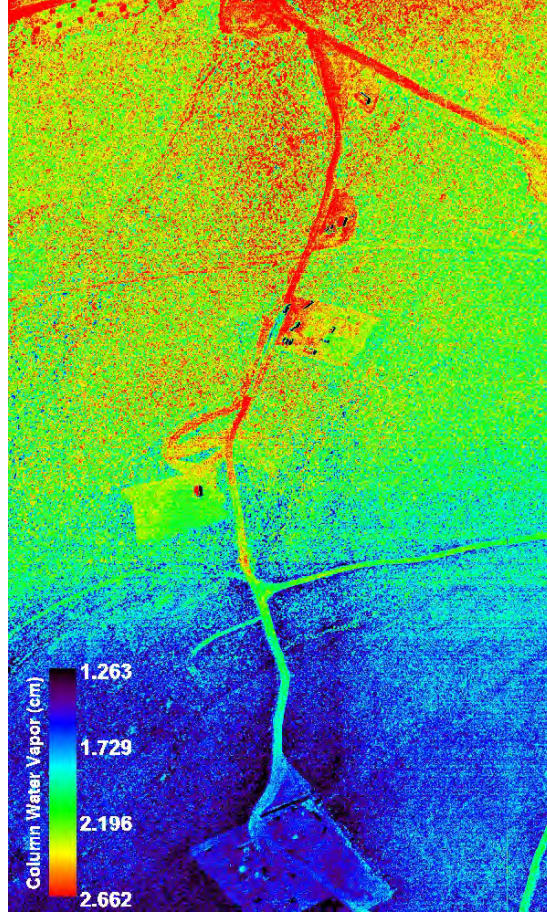


Figure 21. Column water vapor (cm) obtained from the Mid-Latitude Summer FLAASH algorithm.

c. Radiative-Transfer-Ground-Calibration

When comparing the Mid-Latitude Summer FLAASH results to field measurements, it became clear that undesired atmospheric and sensor influences remained present in the image spectra. Specifically, overcorrected features are seen near 0.94, 1.11 and 1.13 micrometers creating unexpected peaks in the reflectance spectra (Figure 22). The features are most likely due to elevation differences within the scene. These issues may also be associated with the assumption that the model is an exact representation of reality, which is not true for this dataset. The features are more apparent in soil spectra compared to spectra of manmade targets (Figure 22).

To remove the undesired features a hybrid method similar to the method described by Clark et al. (2002) was implemented. Radiative-transfer-ground-calibration

(RTGC) used a combination of radiative transfer model results and ground spectral measurements to convert radiance to reflectance. First, the Mid-Latitude Summer FLAASH algorithm was applied to the image to remove atmospheric absorption features and correct spectral response relative to wavelength. Next, ground spectra collected on site were used to create a calibration site. A comparison of the average ground spectra to the image spectra indicated that additional corrections were required (Clark et al., 2002). A multiplicative gain factor was derived for each spectral channel by dividing the average field spectrum by the calibration site average spectrum. After applying the correction factor to the data, the resulting image spectra for the calibration site closely resembled the field and laboratory reflectance spectra. This approach also makes spectra for other natural and manmade targets in the scene appear more like known reference spectra (Figure 22). Moving forward, VNIR and SWIR analysis was performed on the reflectance data corrected using the hybrid RTGC approach.

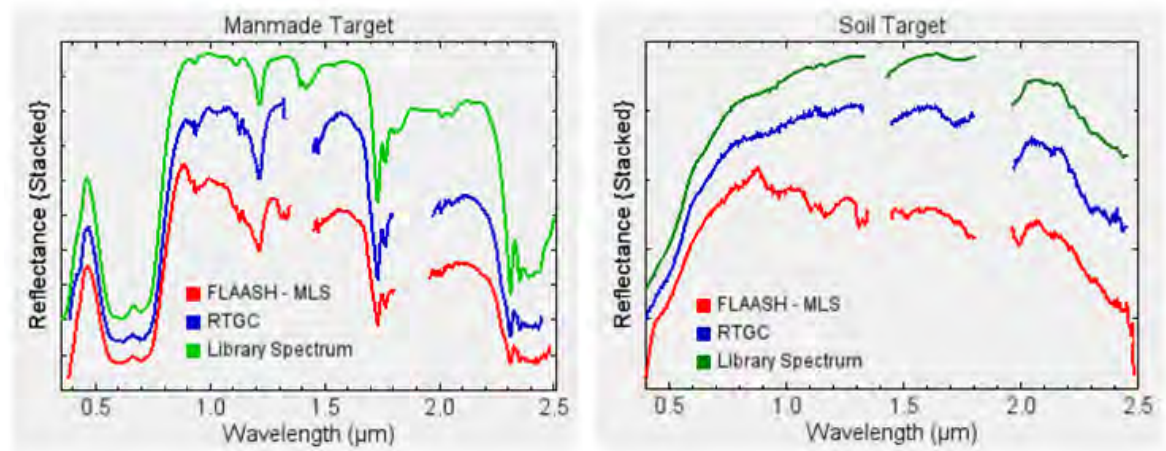


Figure 22. Comparison of FLAASH and RTGC correction results against ground measurements. Left: Manmade target (335,892), Right: Soil target (349,209).

3. Geometric Corrections

The MSS-1 imagery were geometrically corrected to allow direct comparison of image spectra to ground truth spectra and for later combined full spectrum analysis with

the SEBASS imagery. A Geometry Lookup Table (GLT) was created by transforming the Input Geometry File (IGM), derived from sensor parameters and collection information, to a map referenced dataset (EXELIS, 2014). The image geometry and location were further refined utilizing known ground control points (GCPs) to provide more accurate geolocation.

Georeferencing changes the hyperspectral cube by adding null values around the edges of the image that must be masked in processing. These inflate the size of the dataset by replicated pixels as indicated in the GLT files (EXELIS, 2013). Due to these drawbacks only three bands representing a true color image ($0.638\ \mu\text{m}$; $0.547\ \mu\text{m}$; $0.467\ \mu\text{m}$) were used to create a GLT for initial georeferencing.

a. Georeferenced Geometry Lookup Table

The provided IGM file associated with the MSS-1 data was used to create the GLT, a file of map-projected coordinates for each image pixel. The IGM file consists of the x and y latitude and longitude coordinates for each pixel in the uncorrected input image (EXELIS, 2013). In this specific case the IGM input data were geographic latitude and longitude utilizing the World Geodetic System from 1984 (WGS-84) datum, while the desired output for georeferenced image (which contains the map projected pixel coordinates for the specified map projection) was Universal Transverse Mercator (UTM) using WGS-84 datum - Zone 11 North.

The GLT file contained the sample and line locations of each pixel in the output image corresponding to the input image. Positive GLT values indicated there was an exact pixel match and negative values used the nearest neighboring pixel value to interpolate the pixel value (EXELIS, 2013). The calculated parameters for the GLT are shown in Table 3 and the georeferenced true color reflectance image is shown in Figure 23 along with the visual representation of the GLT. The dimensions of the referenced reflectance image changed from 600 samples x 1000 lines to 611 samples x 1294 lines. The majority of the negative GLT values were around the edges of the GLT image. The dark pixels in the GLT images represent interpolated pixels and the dark area bordering the georeferenced image is the image boundary of no data (Figure 23).

Output Pixel Size (m)	0.654920
Output Rotation	-56°
Georeference Background Value	0

Table 3. GLT Parameters for MSS-1 Data

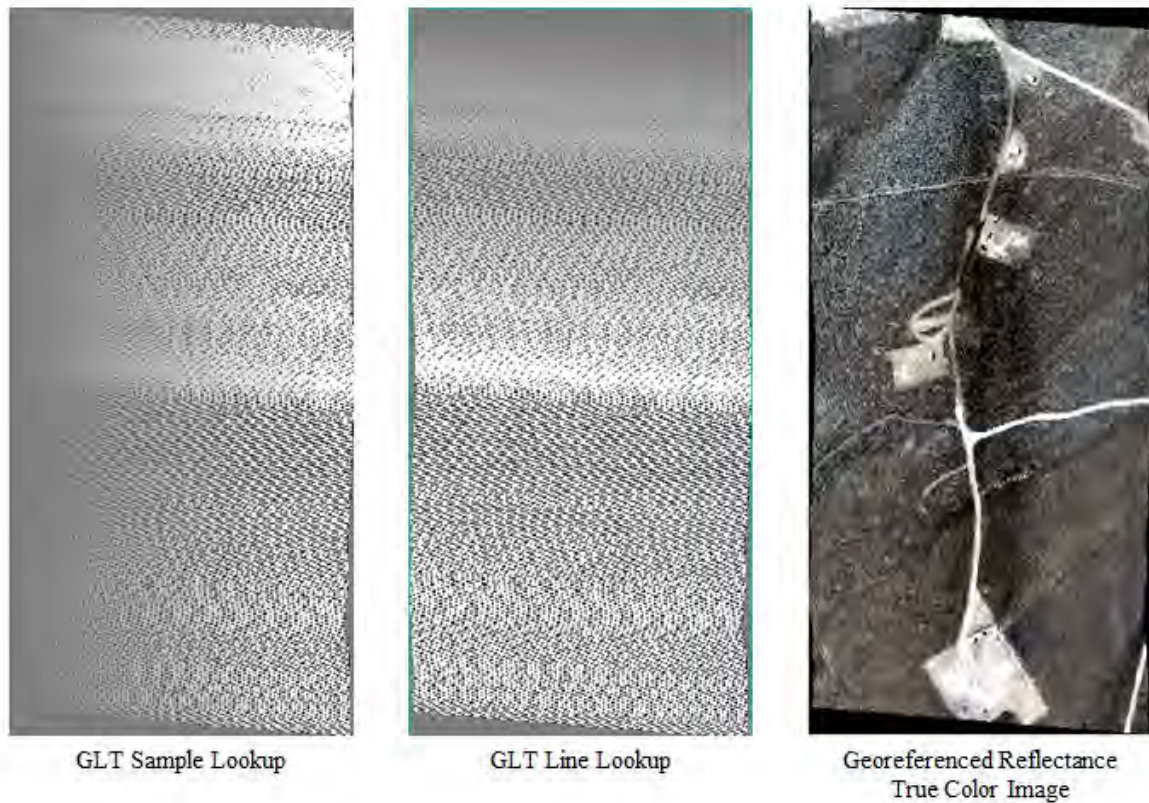


Figure 23. GLT Sample Lookup image (left), GLT Line Lookup image (center), Georeferenced Reflectance image (right). The dark pixels in the GLT images represent interpolated pixels. The dark area in the georeferenced image is the image boundary of no data.

b. Image-to-Map Registration

Sixteen surveyed ground points corresponding to the corners of the four farmhouses in the image were used to refine the geometric corrections. First, the sixteen ground control points (GCP) were plotted in Google Earth to confirm reference latitude and longitude positioning. Using the ENVI software, the GCPs were assigned image

pixel values based on a true color image using the red, green, and blue channels described above (Figure 24). A low root mean square (RMS) error value of 0.16 meters was obtained.

Image warping was applied using a first order polynomial method. This warp includes an XY interaction term to account for image shear (EXELIS, 2014). Nearest neighbor resampling was used because the method uses the nearest pixel without any interpolation to create the warped image limiting the alteration of spectral information. The georeferenced and registered MSS-1 image is shown in Figure 24.

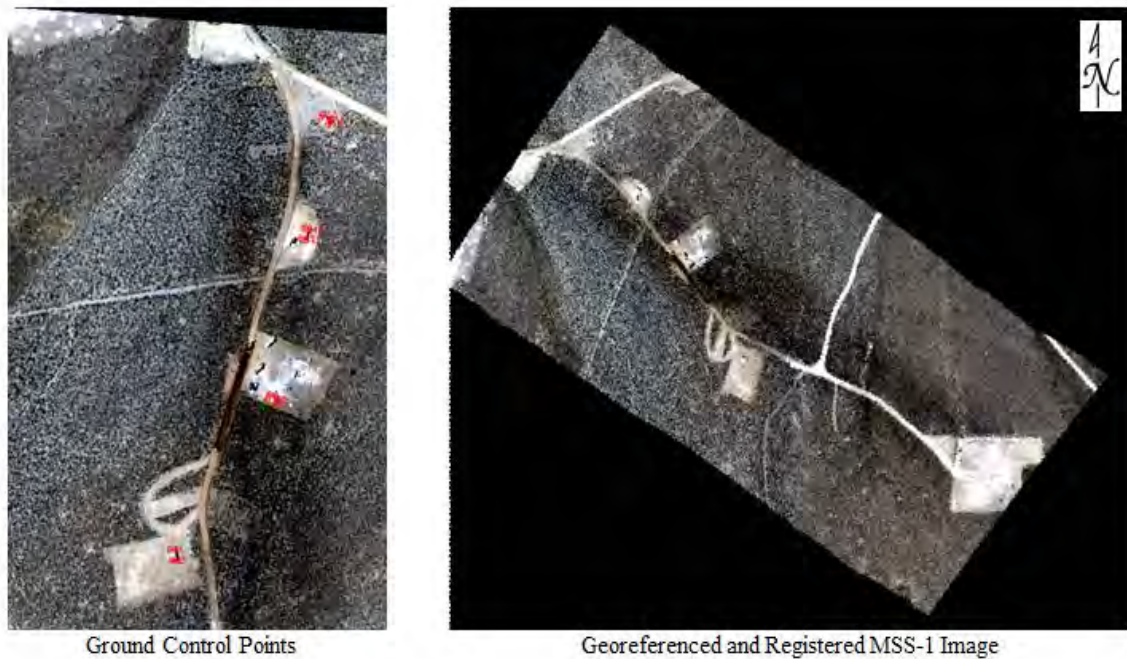


Figure 24. True color unregistered MSS-1 image showing GCPs (left), Geocorrected MSS-1 image (right).

B. LWIR DATA PREPARATION

To begin preparing the LWIR data, approximately the first consecutive 200 hundred lines were removed from the SEBASS flight line because of apparently corrupt pixels as evidenced by horizontal line artifacts. The new subset, used for the remainder of this analysis, had dimensions of 128 samples by 823 lines by 128 bands.

1. Sensor Artifact Removal

A MNF transform was applied to the at-sensor calibrated radiance to assess the quality of the data. The initial MNF bands exposed a nonlinear response of the focal plane as well as very pronounced sensor artifacts (Collins, 1996). These features were most apparent in MNF space because the signal response of these artifacts was stronger than the signal of the features within the scene. The sensor artifact caused a pattern of horizontal lines to show up throughout the image. The first four MNF bands were removed to isolate the bands containing the excess noise issues and an inverse MNF rotation was applied to MNF bands 5-12 (Fountanas, 2014) (Figure 25).

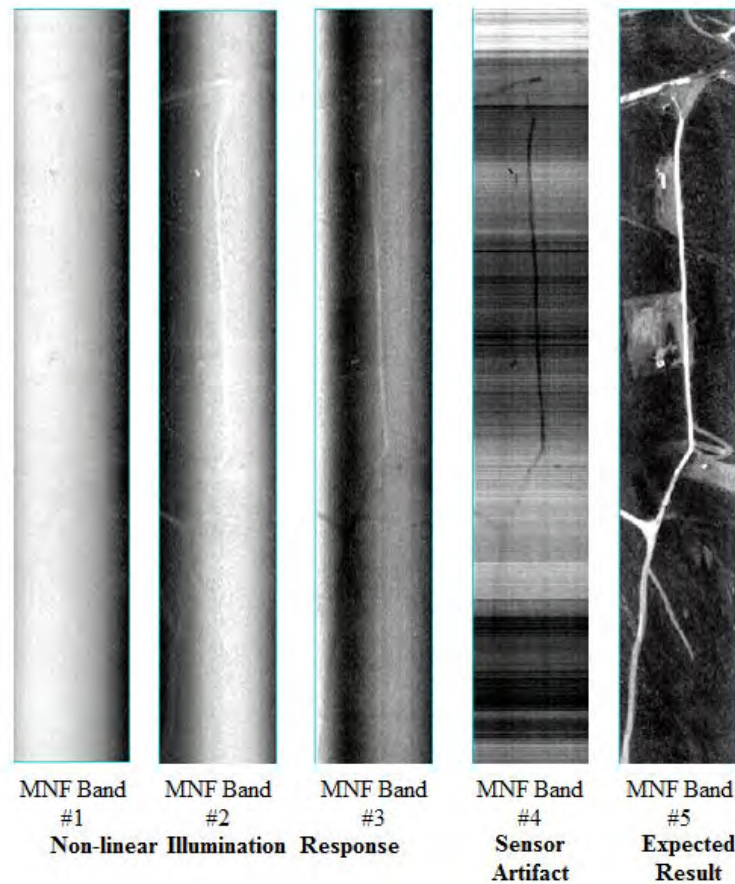


Figure 25. MNF Bands #1-3 exposed the non-linear focal plane array and MNF Band #4 showed the sensor artifact. MNF Band #5 (right) represented the expected MNF result.

An assumption was made that the remaining response signals from the artifacts were weaker compared to the targets within the scene and would therefore not be assigned as endmembers later on in the analysis.

2. Atmospheric Correction

For reasons similar to those discussed previously, atmospheric corrections are necessary in the LWIR region for comparison between image and library emissivity spectra across time and space. Equally important, surface temperatures need to be separated from the emissivity curves for direct comparison to field and library spectra.

Two different atmospheric compensation algorithms were investigated to include an empirical method and a model-based method. The first atmospheric correction algorithm explored was the In-Scene Atmospheric Correction (ISAC), commonly used for simple empirical correction of LWIR data and found in the ENVI suite (Young, Johnson, & Hackwell, 2002). The second algorithm used was a pre-release version of the MODTRAN-based atmospheric model “Fast Line-of-sight Atmosphere Analysis of Spectral Hypercubes – Infrared” (“FLAASH-IR”) based on principles similar to FLAASH (Adler-Golden, Conforti, Gagnon, Tremblay, & Chamberland, 2014; Matthew, 2003). The same temperature emissivity separation algorithm was applied to provide direct comparison of the two algorithms (Kealy & Hook, 1993).

a. In-Scene Atmospheric Correction

The ISAC algorithm used in-scene LWIR information to characterize the terrestrial scene (Young et al., 2002). ISAC is an effective and available algorithm that does not require radiative transfer modeling (DiStasio & Resmini, 2010). The transmission and upwelling radiance were extracted from the data using a line-fitting procedure (Young et al., 2002). ISAC depends on the natural occurrence of blackbody surfaces within the scene and assumes natural temperature variations (Young et al., 2002). Surface areas covered by green vegetation or water exhibit near blackbody qualities and were therefore used as blackbody references in the algorithm. The algorithm also assumed that the surface temperature is greater than the effective atmospheric radiation temperature (Young et al., 2002).

Surface temperature estimated for each pixel were calculated from a normalized regression fitting technique using the maximum value of the brightness temperatures found throughout the input wavelengths (EXELIS, 2013). The “Top of Bins” fitting techniques was used which fits a line to the top of the scatter plot of radiance verse brightness temperature. A spectrum atmospherically corrected with ISAC is compared to a spectrum of calibrated radiance in Figure 26.

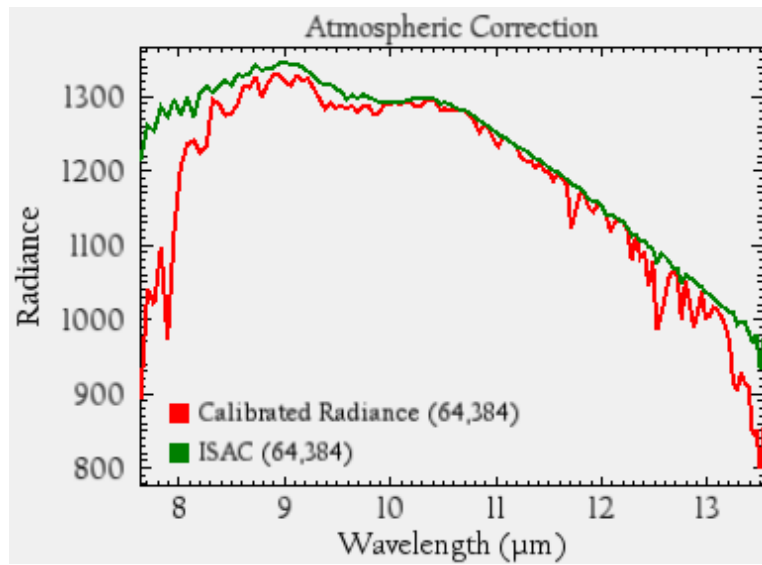


Figure 26. ISAC Results for single pixel SEBASS LWIR data.

b. Fast Line-of-Sight Atmosphere Analysis of Spectral Hypercubes – Infrared

A pre-release version of FLAASH-IR was used for this research. FLAASH-IR allows the user to manipulate atmospheric and aerosol models for the LWIR spectral range (Adler-Golden et al., 2014). Similar to the FLAASH algorithm implemented in ENVI for VNIR-SWIR HSI data, flight and sensor parameters were included in the correction and removal of atmospheric influences. The algorithm took into account the surface air temperature, water vapor column density, and an ozone column density scale factor to suppress atmospheric influences by modifying a built-in MODTRAN atmospheric model (Adler-Golden et al., 2014). Both the model mode and aerosol type were designated to “automatic” allowing the algorithm to choose the best model based on

the location and date information. Several FLAASH-IR modes were tested, however, the differences between the results were negligible and the “TES with Rigorous Fitting to entire wavelength range” was used for comparison with the ISAC results.

Comparison of the calculated emissivity to the calibrated radiance shows that both atmospheric corrections remove a significant amount of the atmospheric influences. The atmospherically corrected spectra resemble Planck-like radiance curves (Figure 27). The FLAASH-IR spectra appear less noisy in the 7.5 to 9.0 micrometer range compared to the ISAC corrected spectra. Slight minima in all three radiance spectra are seen near 9.6 micrometers caused by activated ozone (Adler-Golden, Gruninger, & Smith, 1992).

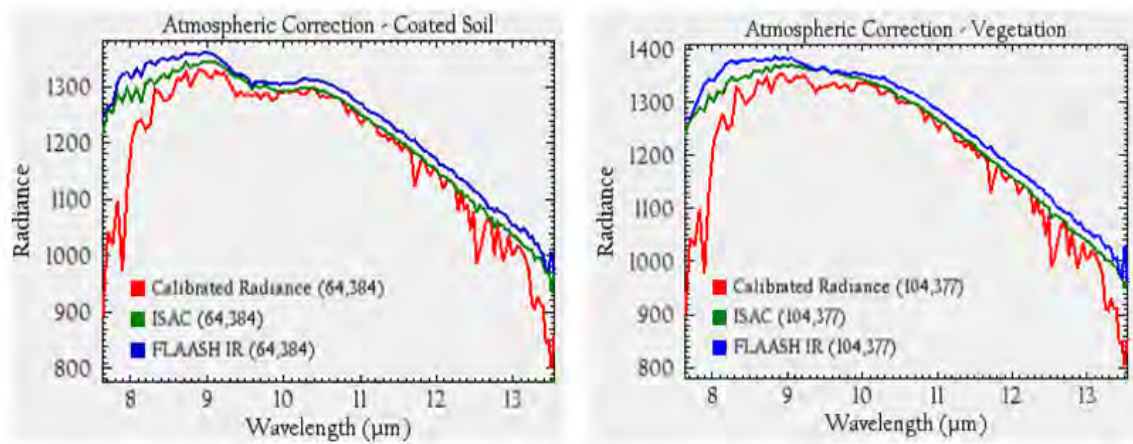


Figure 27. Comparison of ISAC and FLAASH-IR radiance spectra: coated road pixel (left) and vegetation pixel (right).

3. Temperature Emissivity Separation

The radiation emitted from a surface in the LWIR is a function of surface temperature and surface spectral emittance, as well as atmospheric influences (Kahle & Alley, 1992). To determine surface emissivity spectra within the scene, temperature has to be removed from the radiance data.

Emissivity values for both the ISAC corrected image and FLAASH-IR corrected image were calculated using the emissivity normalization algorithm in ENVI. The emissivity normalization technique calculates the temperature for every band in each

pixel using a fixed emissivity value. The highest temperature for each pixel is used to calculate the emissivity values using Planck's function (Kealy & Hook, 1993). For this work, the maximum emissivity value was set to 1.0 for better comparison with the ground truth spectra, which have values with maxima of 1.0. The first and last three bands showed noisy results and were removed from the image before separating the temperature component because their values contained outliers.

A mean region of the coated road was selected for emissivity comparison, highlighted in red in Figure 28. The model-based FLAASH-IR spectrum is smoother compared to the ISAC spectrum, especially longward of 10 micrometers. Both spectra contain the ozone feature near 0.96 micrometers, but a similar feature is also found in the ground measurements of the coated road.

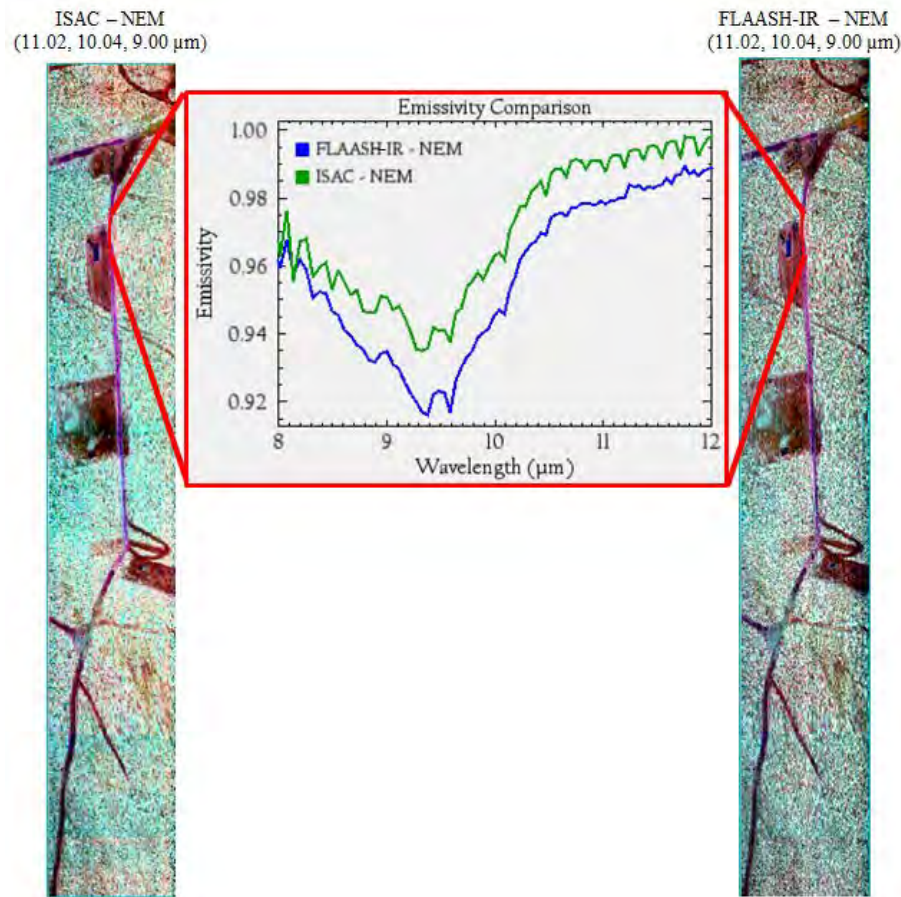


Figure 28. Comparison of ISAC - NEM and FLAASH-IR - NEM results for SEBASS LWIR data.

The emissivity spectra produced from the TES algorithm in FLAASH-IR were visually compared to the FLAASH-IR NEM spectra. The ozone feature near 9.6 micrometers was more pronounced in FLAASH-IR TES spectra causing real features in the 9.0 to 10.0 micrometer region to be falsely represented. Additional testing to remove the ozone feature would be useful, but was not attempted as part of this research. The FLAASH-IR NEM image was chosen as the best option for further integration analysis.

The temperature and emissivity results obtained from the inverse MNF correction were compared against non-corrected LWIR data to identify if and how the correction technique affected the original data. The inverse MNF approach removed the strong signals of the sensor artifacts and had negligible effects on the surface temperature range within the scene (Figure 29). The surface temperature range remained the same in both the original and the corrected data, but some individual pixel temperature values did change. Specifically, the surface temperature of the desert background composed of a mixture of vegetation and soils became more consistent. In the original data the desert background appeared speckled and ranged from 306°K in some regions to 328°K in others. The desert background in the corrected data averaged around 316°K throughout the majority of the scene. The center road in the original data was measured to be approximately 318°K, while the same road surfaces in the corrected data were measured to be approximately 10°K warmer at 328°K. Some emissivity spectra did change with the correction, but overall became less noisy when the artifacts were removed from the radiance image. Two single pixel emissivity spectra from an area in the image showing the largest temperature change, from approximately 305°K to 301°K, were examined (Figure 30). Emissivity features remained at the same wavelength, but overall noise in the corrected spectrum was reduced compared to the uncorrected spectrum. Using a MNF transform to suppress noise and remove the sensor artifacts from the LWIR data was effective and the results were used for the remainder of this research. It is important to note that even though the temperature and emissivity of some individual pixels changed when the correction was applied the slight alterations were expected to be beneficial for analysis and isolation of spectral endmembers.

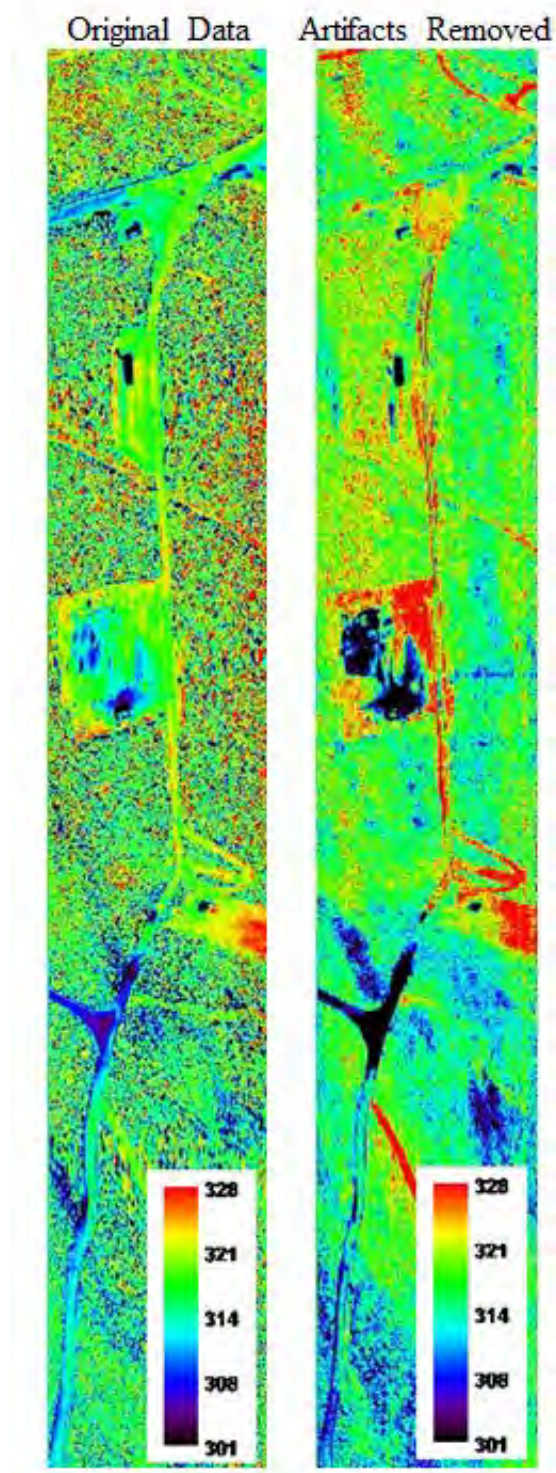


Figure 29. The temperature range, in both the original dataset (left) and the data corrected for sensor artifacts (right), was approximately 301 to 328°K.

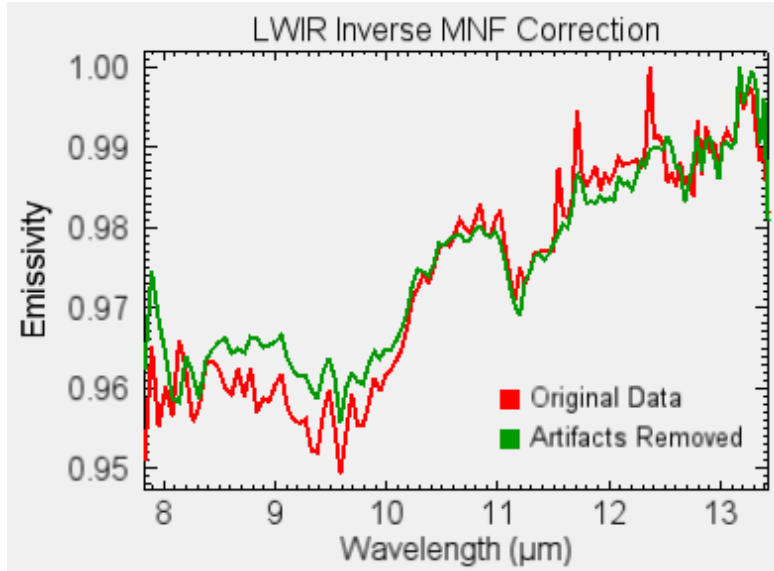


Figure 30. Comparison of uncorrected LWIR emissivity data to corrected data.

4. Geometric Corrections

The final steps in preparing the LWIR data before integrated analysis were georeferencing the SEBASS data using the provided IGM file and then registering the new image to the registered MSS-1 imagery.

a. Georeferenced Geometry Lookup Table

The same procedure as described in the VNIR-SWIR Data Preparation section for georeferencing, using the provided IGM file, was used to build GLT files for the LWIR data. The input geographic latitude and longitude coordinates were projected to UTM WGS-84, Zone 11 North. The updated pixel size and rotation value produced from the projection are recorded in Table 4. The georeferenced result provided a rough estimation of the geographic coverage area of the LWIR scene (Figure 31). The most significant change was the flip with respect to the y-axis changing the overall orientation of the image.

The dark pixels in the GLT images represent interpolated pixels using a nearest neighbor resampling because there was not an exact pixel match from the input image corresponding to the map location. All interpolated pixels have a negative value in the GLT results, while pixels unable to be interpolated have a value of zero. To investigate

the sensor artifacts seen as horizontal lines in the bottom third of the GLT images, a threshold was set to identify all the pixels with a value of zero. Only the image boundary contained pixels unable to be interpolated, while the pixels within the scene to include the sensor artifacts were able to be interpolated using a nearest neighbor pixel.

Output Pixel Size (m)	0.864215
Output Rotation	-44°
Georeference Background Value	0

Table 4. GLT Parameters for SEBASS Data

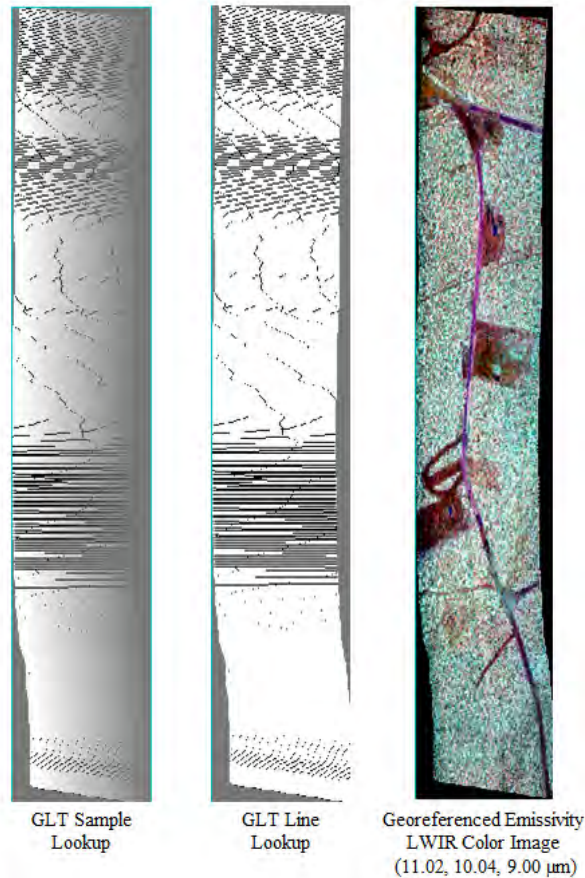


Figure 31. GLT Sample Lookup image (left), GLT Line Lookup image (center), Georeferenced Emissivity image (right). The dark pixels in the GTL images represent interpolated pixels and the dark area in the georeferenced image is image boundary of no data.

b. Image-to-Image Registration

The SEBASS image, using band 65 ($11.02\ \mu\text{m}$, ~ 0.86 meter spatial resolution), was registered to the MSS-1 band 52 ($0.638\ \mu\text{m}$, ~ 0.65 meter spatial resolution) using ground control points (GCPs). Thirty-five GCPs were manually chosen from the VNIR-SWIR image to estimate locations within the LWIR scene. A RMS error value of 1.65 meters was obtained. The LWIR data was warped using a first order polynomial method and nearest neighbor resampling. A color composite of the warped LWIR data is displayed below using 11.02 , 10.04 , and $9.00\ \mu\text{m}$ as RGB (Figure 32).

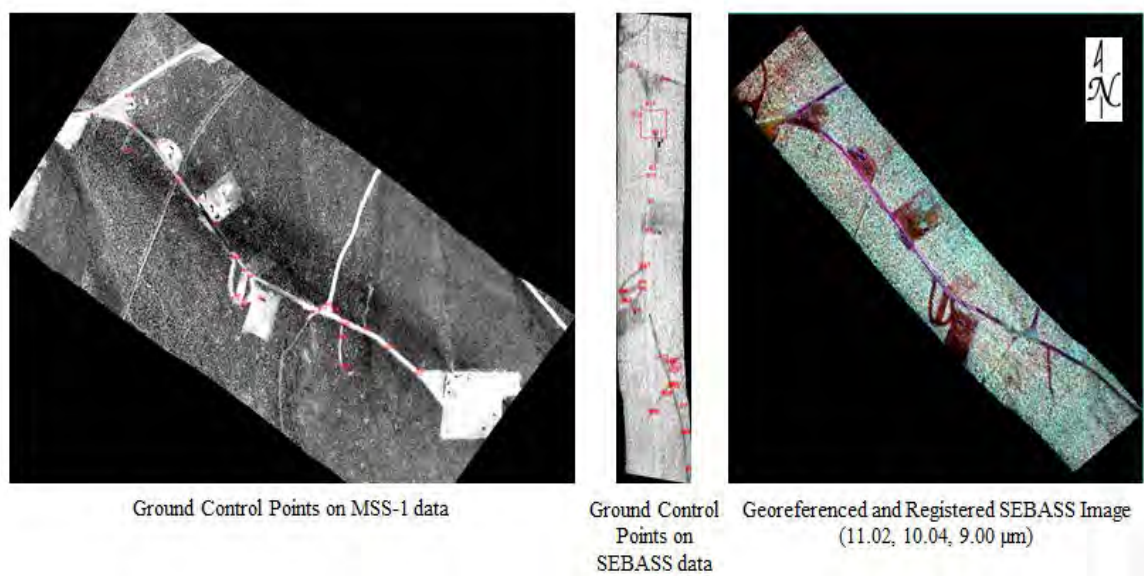
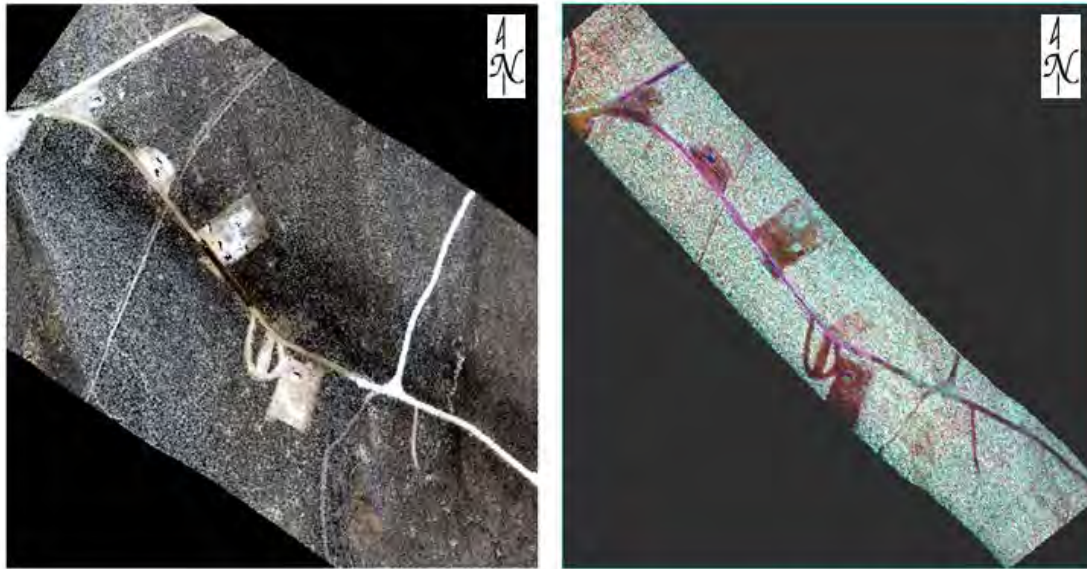


Figure 32. GCPs from base MSS-1 Band 52 (left) aligned with GCPs on warped SEBASS Band 65 (center) used to register the SEBASS image (right).

C. ANALYSIS APPROACHES

Combining the VNIR, SWIR, and LWIR data requires that the scene coverage be identical. The two geocorrected and registered datasets were chipped to the same size (825×875) using a region of interest created from the registered images (Figure 33).



MSS-1 (VNIR-SWIR)

SEBASS (LWIR)

Figure 33. Subset of VNIR-SWIR and LWIR data used for integrated analysis.

1. Standard Hyperspectral Analysis

A standard approach to classifying and mapping hyperspectral data outlined by Boardman and Kruse (2011) was carried out on each wavelength region individually to provide a control for comparison of the integration results (Figure 34). Individual MNF transforms were applied to the VNIR, SWIR, and LWIR subsets. Spectral endmembers were extracted and identified. Individual classification maps were created to expose the sensitivity of each wavelength region and were used as the control for the integration experiment.

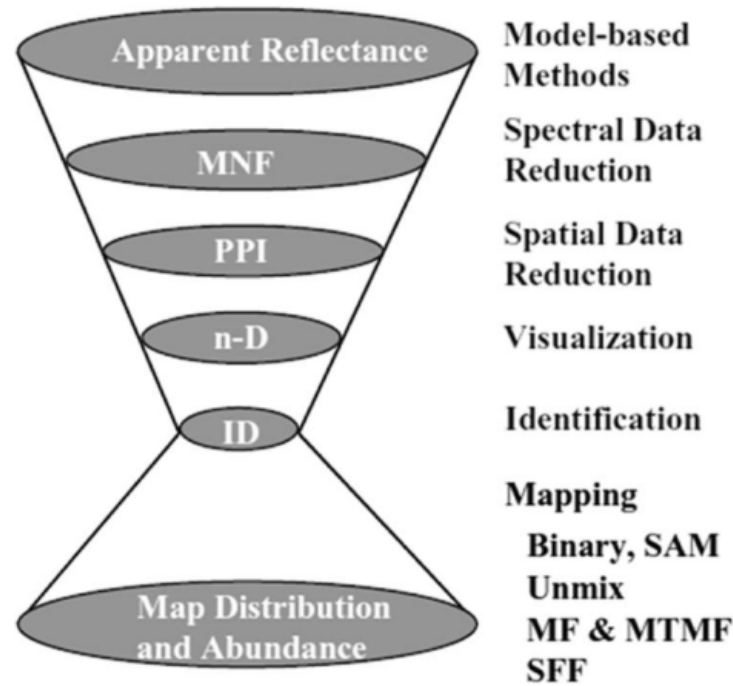


Figure 34. N-Dimensional processing flow for VNIR-SWIR HSI data (from Boardman & Kruse, 2011).

a. Spectral Data Reduction

The MNF transform was coined and developed by Green, Berman, Switzer, and Craig (1988) as an improved principal component analysis (PCA) for reduction of noise content in airborne imaging scanner data. MNF is similar to the PCA transformation, which is standard for MSI data because the data have high between band correlation. Both transforms reduce the spectral information content by performing a linear transformation of the data to reorganize the bands according to high information content. The MNF transform differs from PCA because the noise variance in the transformed data is normalized, resulting in image bands ordered by decreasing signal-to-noise (Boardman & Kruse, 2011; Green, Berman, Switzer, & Craig, 1988).

The dimensionality analysis is essential in hyperspectral data so that the noise in every band is uncorrelated and has unit variance (Boardman, Kruse, & Green, 1995). The output of the MNF transform is apparent reflectance (or emissivity) data projected onto a subset of minimum dimension, with the majority of noise eliminated from the dataset

(Boardman, 1993). This linear transform is commonly used for noise characterization and minimization in HSI data (Boardman & Kruse, 2011). Spectra from the three data regions used in this research were transformed into MNF space to minimize the influence of noise on the data processing and analysis. Only the coherent portions of the data resulting in the highest signal, the initial MNF bands, were carried forward in the analysis.

b. Spatial Data Reduction

The pixel purity index (PPI) algorithm was useful to reduce spatial dimensionality of HSI data to narrow down the possible endmember spectra. Thinking of spectra as points in an n -dimensional scatterplot, where n is the number of bands, allows spectral endmembers to be detected from the distribution of points (Boardman, 1993). Spectral endmembers are defined as the purest spectral signatures and their combinations can be used to explain all of the spectra in an HSI dataset via spectral mixing. Applying convex geometry principals, a best fit simplex was determined based on the content of the scatterplot. The vertices of the simplex were used to best estimate the spectral signatures of the mixing endmembers (Boardman, 1993).

The PPI was created by repeatedly projecting the data in MNF space onto random unit vectors (Boardman et al., 1995). A cumulative record was maintained during the iterations when a pixel was found to be extreme (i.e., most spectrally pure). The output was an image created using digital number (DN) values to display the number of extreme hits each pixel obtained during the PPI iterations. The pixels with the most hits were identified as possible image endmembers minimizing the number of pixels used for further analysis (Boardman et al., 1995; Boardman & Kruse, 2011).

c. Visualization

Once the spectral and spatial information were reduced to a manageable size, the pixels were visualized in the n -Dimensional Visualizer tool in ENVI. The desired dimensionality corresponded with the number of non-noise MNF bands. Initially, the ‘Auto Cluster’ option using the most extreme 10,000 pixels was chosen to assign an endmember class to pixels containing similar spectral information. The majority of classes consisted of single pixels as endmembers, so several of the classes were

deselected and a manual selection process proceeded. The pixels located at the vertices rotating in the same direction in various dimensions were selected as possible spectral endmembers.

d. Identification

The mean spectra of the selected endmembers were used for comparison against measurements in spectral libraries and obtained via field collections. Visual comparison of spectral plots was used for initial selections. Beyond visual comparison, several algorithms that utilize location, depth, and shape of spectral features exist for identification of image endmember spectra. Identification of spectra for this thesis was accomplished using visual comparison, the expert system approach of Kruse, Lefkoff, and Dietz (1993a) and Kruse (2008); and “SigDB” by Ramachandran et al. (2014).

The “Spectral Expert” uses diagnostic features and characteristics of spectra to create rules for identification. The goal of the algorithm is to extract and isolate individual reflectance absorption features. A continuum is defined for each image endmember spectrum by creating a straight line between local maxima. The feature position, the feature depth, the full width at half maximum depth, and absorption band asymmetry are extracted to analysis (Kruse, Lefkoff, & Dietz, 1993a; Kruse, 2008). A matching score between 0.0 (no match) and 1.0 (perfect-match) is calculated for each specific pixel material. The algorithm is most effective when analyzing unique endmembers with prominent features and least effective for analysis of spectral mixtures.

The “SigDB” was created to meet the demands of the industry for a tool with the ability to view, search, and match infrared spectra obtained from a variety of sources. The database aids in the “exchange, preliminary analysis, comparison and classification of collected spectra” (Ramachandran et al., 2014, p. 5). Spectral comparison and identification of unknown spectra against library spectra is conducted using a derivative of SAM and k-Mean clustering to spatially characterize spectral similarities. The program provides direct comparison of spectra obtained from sensors with different spectral resolution and coverage.

e. Mapping and Characterization

A variety of methods are available for characterization of HSI data, including, but not limited, to Spectral Angle Mapper (SAM), feature-based classification, and spectral unmixing. SAM is an empirical approach that calculates a similarity score between an image spectrum and a reference spectrum, where a smaller score between the two spectra indicates higher similarity (Kruse et al., 1993b). Feature-based classification uses a continuum removal to extract strong spectral features for comparison against library spectra for identification and characterization (Clark & Roush, 1984, Clark et al., 2003, Kruse, 1988; Kruse et al., 1993a; Kruse, 2008). Spectral unmixing is defined as the process of reducing spectra containing multiple substances into specific endmembers – key spectral signatures that explain HSI data variability, and a set of fractional abundances representing the proportion of each endmember (Tarantola & Valette, 1982). Mixed pixels occur when the spatial resolution of a sensor is low enough that several substances occupy one pixel and their spectra combine at the sensor, or when distinct materials are physically combined into a mixture (Tarantola & Valette, 1982). Linear algorithms can be assumed if endmembers in a pixel appear in spatially segregated patterns. Non-linear approaches must be used when endmembers are mixed on a spatial scale smaller than the path length of photons in the mixture (Keshava & Mustard, 2002).

This thesis research utilized the spectral unmixing approach to map and characterize spectral endmembers using HSI. In both MSI and HSI data, image spectra may represent surfaces made up of mixtures of materials with different spectral properties. The increased number of spectral bands in HSI compared to MSI data allows pixels composed of multiple materials to be analyzed. Unmixing methods enable spectral separation of the materials' signatures (Boardman & Kruse, 2011).

In this work, the partial unmixing method Mixture-Tuned Matched Filtering (MTMF) was used because it does not require all the endmembers in the scene to be known, but still provides estimated abundances for each endmember (Boardman & Kruse, 2011). MTMF combines statistical concepts of matched filtering (MF) analysis with theory from linear mixing models. The MF model originated in the field of electrical engineering and signal processing, where the signals are unbound and false positives are

not restricted. MF theory alone fails in hyperspectral analysis because of the feasibility constraints of the simplex being additive and nonnegative (Boardman & Kruse, 2011). The MTMF procedure includes MF for abundance estimation and mixture-tuning (MT) for false positive rejection (Boardman & Kruse, 2011). Figure 35 illustrates the MTMF feasibility constraints; the certainty of pixel identification increases towards the center of the feasibility contours.

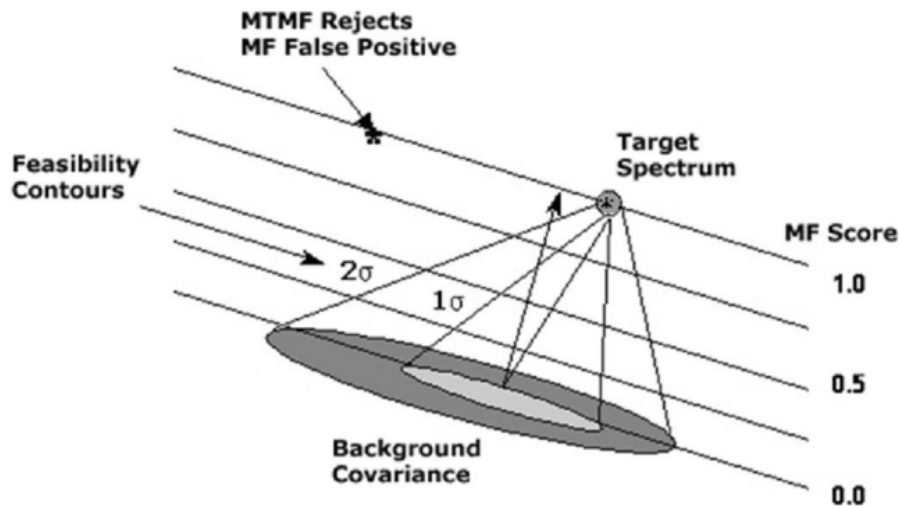


Figure 35. MTMF Feasibility Cone Concept (from Boardman & Kruse, 2011).

MTMF was applied to determine the feasibility of the unknown natural and dominant endmembers based on the target endmembers discovered during PPI investigation and n -dimensional visualization. Abundance estimation, the MF score, was calculated using the MNF data statistics for the background, and the MT score, defined as “infeasibility” was calculated using convex geometry theory to evaluate the feasibility of each pixel with regards to both the target and background (Boardman & Kruse, 2011). High MF scores correspond to high abundances of a specific endmember. Low infeasibility scores indicate high feasibility for that endmember. A ratio of MF to infeasibility score (used in further discussion here as the “feasibility ratio”) was used to determine those pixels with feasible mixtures and the highest abundances (Kruse et al.,

2011). Larger feasibility ratios indicate higher likelihood of a specific endmember occurring at that pixel.

Rule classification, a simple thresholding approach, was used to apply a consistent threshold to the feasibility ratio across all endmembers, and to produce classification maps of the most spectrally abundant material at each pixel (EXELIS, 2014). The background, defined as the densest area of pixels, clusters around zero abundance and zero infeasibility. Separation of endmember abundance from background was straight-forward where the background was compact and the endmember was able to be isolated (Figure 36, Left). In cases where the background was distributed, it became difficult to separate the endmember from background, and some background pixels were included in the class assignment (Figure 36, Right). For this research, a higher significance was given to the consistent comparison of the mapping results, and examples of the undesired inclusion of background pixels in the classification maps have been noted within the discussion. A feasibility ratio threshold was selected that mapped the majority of the endmembers for each wavelength range without including excess background pixels. If the threshold was reduced, the resulting map would have assigned background pixels as endmember pixels, and if the threshold was increased, additional endmembers would have been omitted from the map.

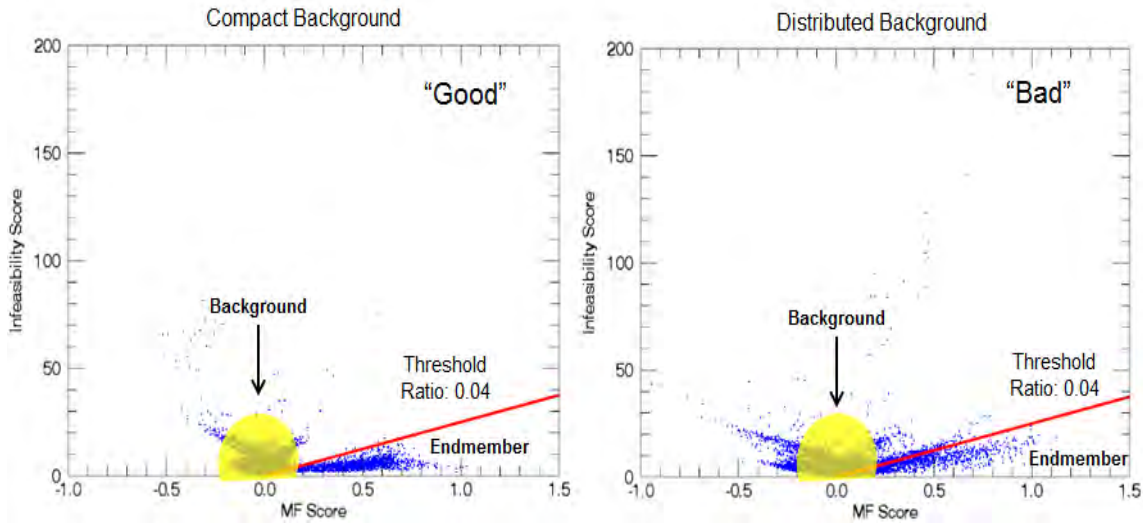


Figure 36. Examples of dispersal of pixels in MTMF plot; compact background and isolated endmember (left) compared to distributed background and endmembers with inclusion of background pixels using the 0.04 feasibility ratio threshold (right).

2. Integration

Two integration techniques were performed on the VNIR, SWIR, and LWIR datasets and compared to the standard hyperspectral analysis. The goal of the integration was to improve classification and mapping results by making use of the complementary features in all three spectral regions.

a. MNF Integration

The first approach applied the MNF transform to the three wavelength regions independently. Then, all non-noise MNF bands for the VNIR, SWIR, and LWIR regions were combined by creating a new image file. This was possible because the datasets were georegistered and provided consistent coverage. The new image consisted of forty-three bands: eleven VNIR MNF bands, twenty-two SWIR MNF bands, and ten LWIR MNF bands. The order of MNF bands was not significant because the MNF transformation is linear (Green et al., 1988). The analysis procedure from the integration point onward was the same as the standard approach described above. PPI was applied to the combined MNF image. The most extreme pixels were visualized using the n -Dimensional

Visualizer and possible spectral endmembers were isolated and identified. MTMF analysis was performed and a single classification map was created using the feasibility ratio threshold approach.

b. Full Integration

The second approach, coined *Full Integration*, combined 476 hyperspectral bands from the VNIR, SWIR, and LWIR regions prior to spectral reduction analysis using MNF. Again, combining these was possible because the spatial dimensions of the datasets were consistent. Before integration the SEBASS data were converted from emissivity to reflectance using Kirchoff's law to create consistency for viewing purposes. A new image was created by stacking the overlapping pixels of the MSS-1 reflectance and SEBASS reflectance data using nearest neighbor resampling. Layer stacking allowed for the entire spectral range from 0.4 to 2.5 and 8.0 to 13.5 micrometers to be viewed for each pixel. The combined dataset was transformed using MNF, applying a mask of only the pixels found in both the MSS-1 and SEBASS coverage area. Only MNF bands with significant information content were carried forward in the analysis and classification process. The standard hyperspectral analysis procedure as described above was implemented after the integration step to create a single classification map.

3. Field Spectroscopy and Validation

Field spectroscopy has a similar goal to HSI, to acquire accurate "data on the spectral [characteristics] of Earth surface materials from a remote location" (Milton, Schaepman, Anderson, Kneubuhler, & Fox, 2009, p. S92). Field measurements can be acquired with more control compared to airborne and satellite collects. For example, the target of interest can remain in the field of view for a longer duration and the path length between the target and the sensor can be reduced (Milton et al., 2009). Field instruments commonly have a higher spectral resolution and can provide additional information, as well as help fill in the missing gaps of overhead data.

There are a variety of commercially available field portable spectroradiometers capable of recording either the reflectance or emission properties of surface materials. Ground spectra of the NNSS site were measured for this study with the Spectra Vista

Corporation (SVC) HR-1024i and the Designs & Prototypes (D&P), discussed below. The field measurements aided in atmospheric correction of the MSS-1 data, as well as identification of spectral endmembers found in all three wavelength regions.

a. Spectra Vista Corporation (SVC)

The SVC HR-1024i is a field portable spectroradiometer covering the VNIR-SWIR wavelengths spanning from 0.35 to 2.5 micrometers. The sensor has a spectral resolution of approximately three nanometers in the VIS, nine nanometers in NIR, and six nanometers in the SWIR. The SVC uses one silicon and two indium gallium arsenide (InGaAs) diode array diffraction grating detectors to measure up to 1024 spectral bands (Spectra Vista Corporation, 2013). The instrument records local time and location information associated with each spectral measurement.

Radiometric calibration was achieved using a white reference and a dark reference. The white reference was a spectralon panel which has known highly diffuse reflectance. The dark reference was measured using the black cap of the lens, which has zero reflectance. One measurement was taken for each point of interest at the test site. Approximately ten spectra were acquired across a section of the road of interest and averaged to represent the mean spectra of the target road section (Figure 37). The radiance to reflectance conversion was calculated onboard the instrument.

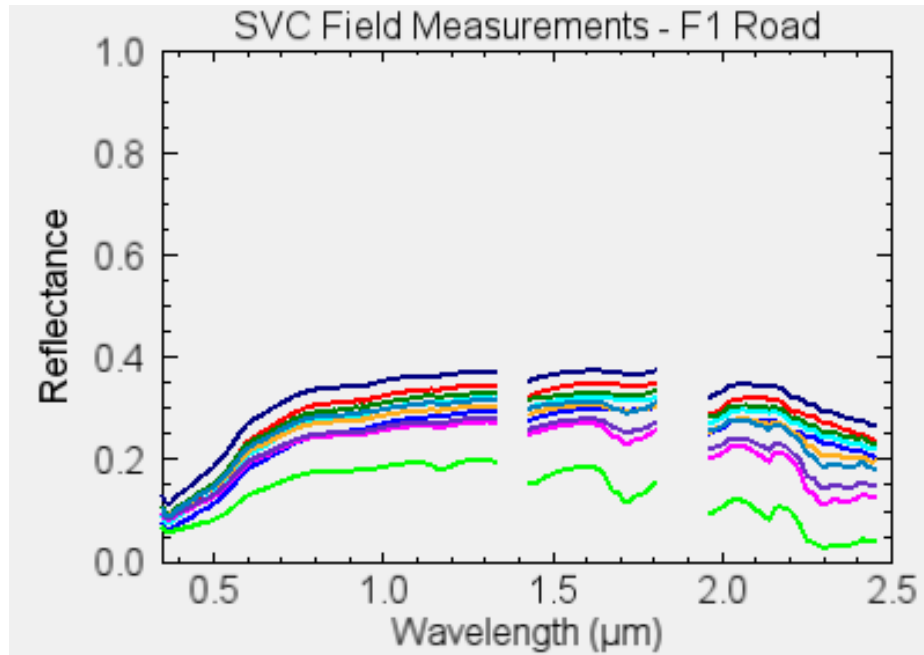


Figure 37. SVC reflectance field measurements of F1 Road.

b. Designs and Prototypes (D&P)

The D&P is a complete person-portable infrared spectrometer packaged in a small, portable, and durable case. The instrument measures a continuous spectrum of solar radiance using a miniature Michelson interferometer with a spectral range of approximately 2 to 16 micrometers. The spectral resolution can be adjusted to 2, 4, 8, or 16 inverse centimeters. The standard detector is a dual sandwich type, consisting of indium antimonide (InSb) and mercury cadmium telluride (HgCdTe). A temperature controlled laser diode provides the reference for the servo and sampling electronics, and wavelength calibration for the spectrum (D&P Instruments, 2009).

For this study, the D&P was calibrated approximately every 15 to 20 minutes using the attached blackbody, acquiring a warm and cold blackbody measurement to set the limits of the sample measurement. Radiance measurements covering the LWIR were obtained using the same approach as the VNIR-SWIR measurements, once at each point of interest and an average of approximately ten measurements to represent the sections of road throughout the scene (Figure 38). A downwelling radiance measurement was acquired every 1 to 2 minutes between sample measurements to account for atmospheric

and cloud conditions. The downwelling radiance measurements were subtracted from the sample radiance to remove atmospheric effects. The sample radiance measurements were then converted to emissivity using the bulk processing option in the D&P Utilities software (Salvaggio et al., 2001).

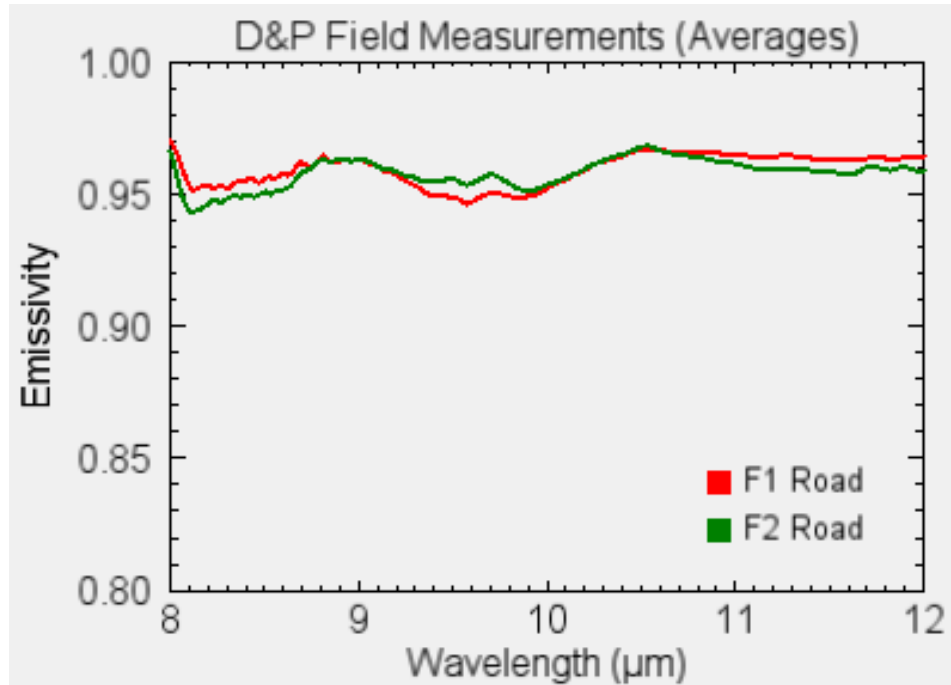


Figure 38. D&P emissivity field measurements averages of F1 Road (red) and F2 Road (green).

IV. RESULTS AND DISCUSSION

A. STANDARD HYPERSPECTRAL ANALYSIS APPROACH

Due to the background pixels generated by the geometric corrections, a mask was applied during the MNF transformations of the three individual wavelength regions to only include the image pixels in the analyses. The MSS-1 data were separated into VNIR and SWIR wavelength regions and the VNIR, SWIR, and LWIR data were individually transformed into MNF space. The number of non-noise MNF bands used for analysis for each region are listed in Table 5, and MNF bands 1, 2, and 3 are displayed as RGB for the VIS, SWIR, and LWIR subsets in Figure 39. The color variations in the MNF images for the individual wavelength regions extracted the baseline differences of the surface materials, but spectral analysis was required to understand and identify the meaning of the color assignments.

Wavelength Region	Wavelength Range (μm)	Number of Input Bands	Number of Non-noise MNF Bands
VNIR	0.387 to 0.998	123	11
SWIR	1.003 to 2.445*	231	22
LWIR	7.829 to 13.427	122	10

*Bands in the atmospheric water vapor region 1.324-1.449 and 1.794-1.970 micrometers were removed.

Table 5. MNF Transform Parameters of VNIR-SWIR-LWIR data

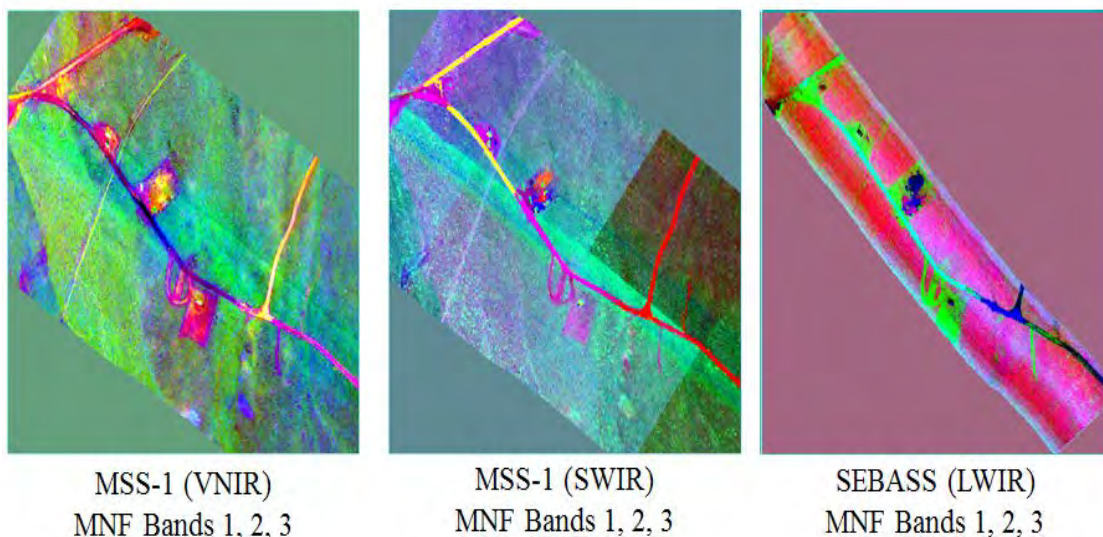


Figure 39. Linear MNF transform results of VIS (left), SWIR (center), LWIR (right) displaying MNF bands 1, 2, 3 as RGB.

The PPI algorithm was applied individually to the non-noise MNF bands from the VNIR, SWIR, and LWIR regions for 30,000 iterations and using a threshold of 2.5 DN, where DN was roughly equivalent to one standard deviation. The total pixel count leveled out after approximately 28,500 iterations for the VNIR, approximately 30,000 iterations for the SWIR, and approximately 28,400 for the LWIR. A threshold was applied to the PPI image to include the purest 10,000 pixels for initial n -dimensional visualization. These pixels represented potential endmember spatial locations. The number of non-noise MNF bands was used to specify the data dimensionality for each region and n -dimensional visualization was used to extract endmember spectra. The spectrally pure pixels located at the vertices of the simplex formed in n -dimensional space by the PPI extracted MNF spectra were selected as image endmembers. The endmember extraction results for the three individual wavelength regions are summarized in Table 6.

Wavelength Region	Number of Endmembers
VNIR	28
SWIR	38
LWIR	17

Table 6. Number of endmembers from each wavelength region

After the pure endmembers were isolated, MTMF analysis was applied individually to the non-noise MNF bands of the three wavelength regions. The feasibility ratio was calculated for each endmember to create consistency and quantify areas with feasible mixtures at various abundances. Classification maps for each wavelength region were generated by applying a feasibility ratio threshold of 0.04 to the endmembers to include only pixels with high MF scores and low infeasibility (Figure 40, Figure 41, and Figure 43). Some endmember classes only contained a few pixels or were omitted from the classification map at the 0.04 ratio threshold. Spectral endmembers composed of similar materials were displayed using similar color shades. What appeared to be man-made materials were displayed on the classification maps using shades of red to purple, vegetation spectra were displayed using shades of green, soils were displayed using shade of yellow to orange, and road surfaces were displayed using shades of blue. In several cases, soil and road endmembers appeared similar spatially and spectrally because the roads were composed of mixtures of soils.

Exact spectral identification of the majority of the endmembers was difficult using only the MSS-1 VNIR reflectance data. Even so, various types of man-made materials, vegetation, and soil varieties were verified using the extracted endmembers, spectral libraries, and spatial and spectral browsing of the MSS-1 VNIR wavelengths (Figure 41). Several of the man-made endmembers in the scene show prominent features between 0.4 and 0.6 micrometers indicating specific colors of the materials. For example, the spectra of Man-made #2, #5, #9, and #14 have broad peaks near 0.56 to 0.59 micrometers suggesting a green to yellow colored target. The majority of the man-made spectra have a sharp rise in reflectance between 0.45 and 0.60 micrometers and a broad

feature from 0.77 to 1.0 micrometers suggesting the presence of iron oxide or iron hydroxide, possibly a hematite or goethite mixture (Hunt & Ashley, 1979; Kerekes, Strackerjan, & Salvaggio, 2008). Man-made #6 has a peak near 0.46 micrometers and a minimum near 0.93 micrometers (common in most plastic materials) leading towards an identification of a blue, opaque high-density polyethylene material. The 0.93 to 0.94 micrometer region is also a known water vapor band. Using only the VNIR wavelengths, this feature could not be used to differentiate between the chemical makeup of the material and the atmosphere. Man-made #17 has a minimum near 0.39 micrometers and a peak near 0.42 micrometers, similar to spectra of white painted materials (painted aluminum in spectral library). Background pixels were included in the Man-made #10 and #12 classes at the 0.04 ratio threshold and therefore are seen spatially mixed in the desert background. The majority of the vegetation appeared green to yellow with a feature near 0.68 micrometers, suggesting the presences of chlorophyll (Elvidge, 1990; Kokaly, Despain, Clark, & Livo, 2007). Vegetation #1 and #4 are mostly featureless in the VNIR region, but spatial analysis indicated the endmembers as possibly dry vegetation. Both spectra have a feature near 0.76 micrometers and Vegetation #1 has a reflectance minimum near 0.94 micrometers. Vegetation #2, #3, and #5 have reflectance minima near 0.68 micrometers and higher reflectance near 0.8 micrometers, indicating healthier vegetation containing water; possible identities include sagebrush or saltbush. The soil endmembers were mostly featureless in the VNIR region, but were identified as desert soils based on spatial analysis of the feasible pixels. Soil #3 and #6 were the brightest soils, while #4 was the darkest soil in the scene. Based on the gradual incline from 0.45 to 0.60 micrometers in the soil spectra iron oxide is assumed to be present. Analysis of the additional wavelength regions, specifically the SWIR, can be used to help further identify the various soil types.

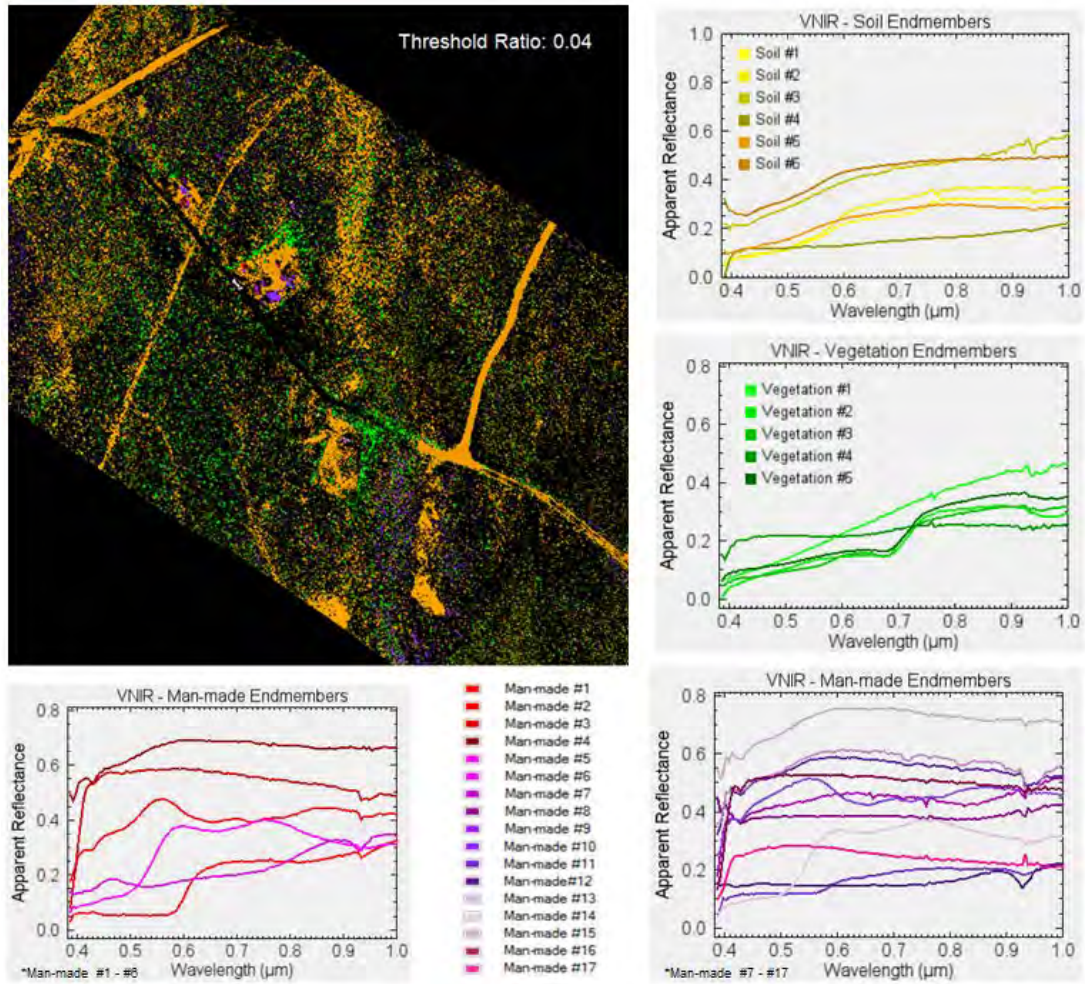


Figure 40. Image Map of MSS-1 VNIR endmembers using a feasibility ratio threshold of 0.04 (Top Left); VNIR endmember reflectance spectra extracted using MNF data (Right and Bottom Spectral Plots).

SWIR endmembers were verified using spectral libraries and spatial and spectral browsing of the MSS-1 SWIR reflectance data. Several man-made targets, a few vegetation types, and sixteen different types of soil spectra were isolated (Figure 41). Many of the SWIR endmember spectra contained a water vapor band near 1.14 micrometers that was not completely removed by the atmospheric correction model. Several of the man-made spectra had a doublet near 1.11 and 1.15 micrometers, similar to the feature seen in fiberglass materials and atmospheric water vapor. Using only the SWIR wavelengths made identification of material features versus atmospheric features challenging. Man-made #10, most similar to the library spectra of a fiberglass roof, has

additional features near 1.72, 2.14, and 2.26 micrometers. Man-made #1 and #8 have a deep reflectance minimum near 1.21 and another feature near 1.54 micrometers, indicating the presences of nylon or a synthetic polymer material. Man-made #1 also has a feature near 1.71 micrometers. Man-made #6 and #12 have features near 2.3, consistent with fiberglass and nylon signatures. All the vegetation endmembers have reflectance minima near 1.68, 2.10, and 2.30 micrometers from protein, lignin, and cellulose associated with dry vegetation (Kokaly, Despain, Clark, & Livo, 2007; Peterson & Hubbard, 1992). From visual comparison to library spectra, possible identifications include tumbleweed, sagebrush, or other types of dry vegetation found in desert environments. Vegetation #2 has a unique feature near 1.19 micrometers consistent with Pinyon Pine, Bigberry Manzanita, and Mormon Tea shrubs spectra. Based on the site location, the most probably identification is Mormon Tea or similar vegetation. Soil #4 has a feature at 2.2 micrometers indicating the presence of clay or mica in the soil; additional features expected in these minerals fall in the water vapor absorption regions and cannot be confirmed using only the SWIR wavelengths. Soil #6, #8, #10 have reflectance minima near 2.15 micrometers, similar to calcite, but lack the strong feature near 2.34 micrometers and instead showed a weak shifted feature near 2.30, similar to dolomite. Soil #7 has features near 1.22 and 2.30. Chlorite is also likely to be in the soils based on features near 2.32 micrometers. When only using the SWIR wavelengths, these feature locations can be confused with dry vegetation or synthetic materials. The various surface coatings on the road could be differentiated in the SWIR. Soil-Road #2 and #5 had similar base coatings applied to the surfaces and different additives, which explains why two spectrally different classes were discovered. Soil-Road #2, #4, and #5 have reflectance minima near 1.68 micrometers, #2 and #4 have additional features near 2.14 and 2.30 micrometers corresponding with ground measurements collected on the site. These features are not present in spectra of the untreated road surfaces (Figure 42).

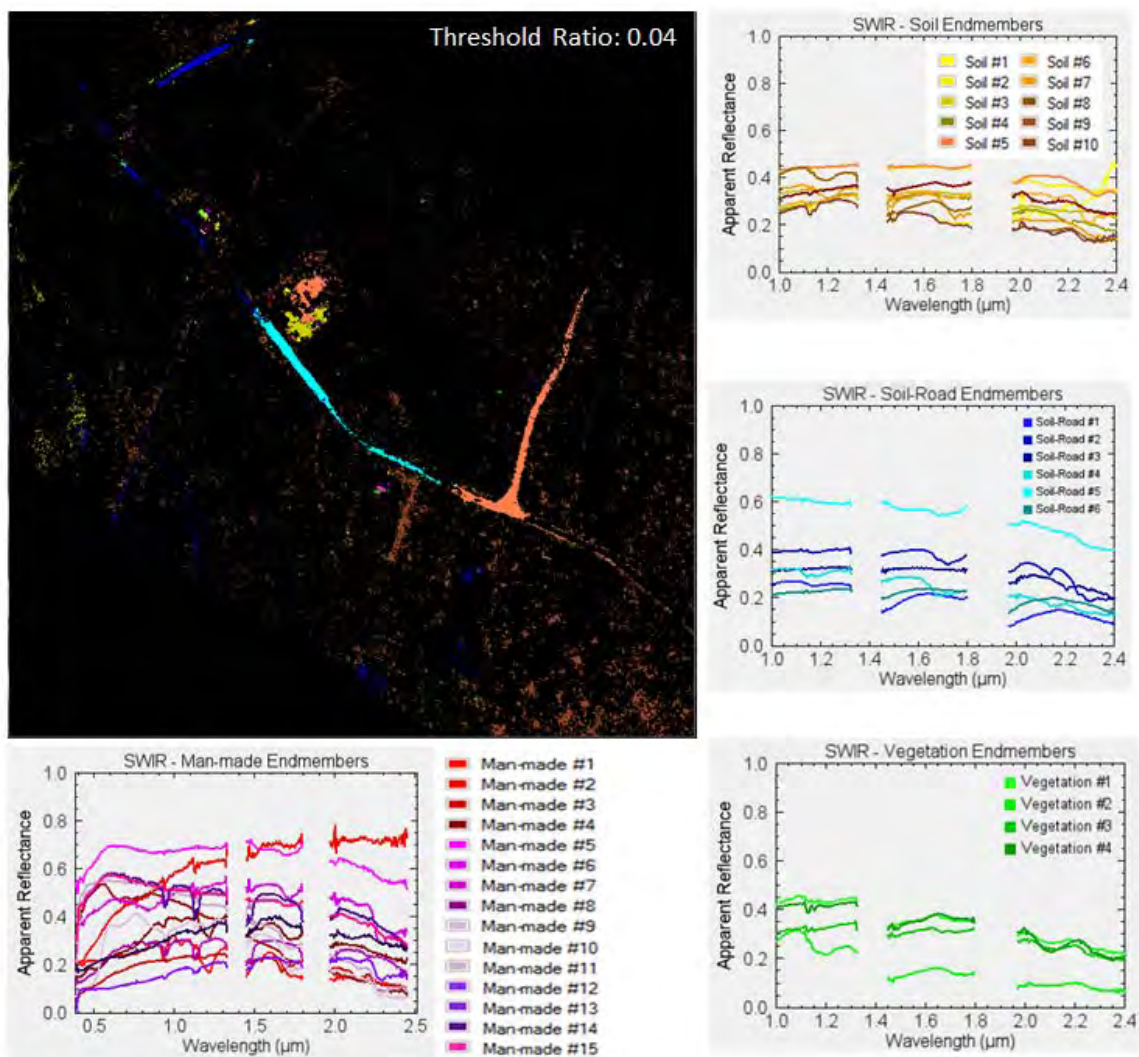


Figure 41. Image Map of MSS-1 SWIR endmembers using a feasibility ratio threshold of 0.04 (Top Left); SWIR endmember reflectance spectra extracted using MNF data (Right and Bottom Spectral Plots).

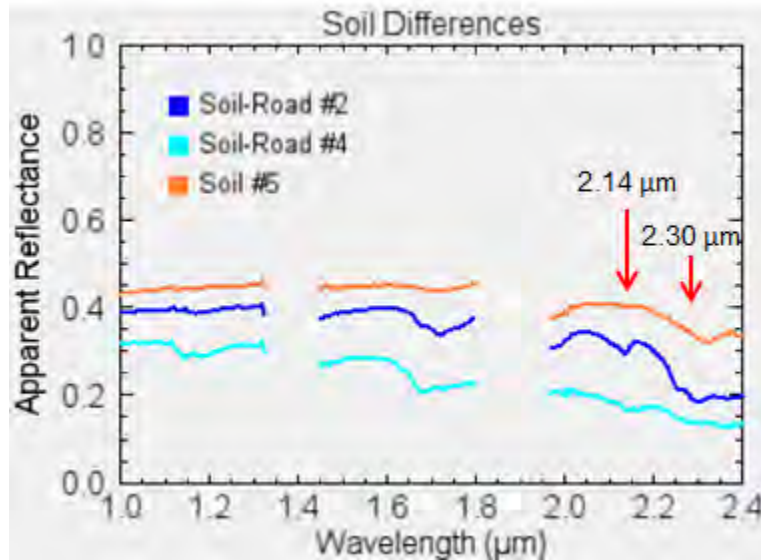


Figure 42. Differences between road (Soil-Road #2 [blue] and Soil-Road #4 [cyan]) and bare soil (Soil #5 [orange]).

A few man-made objects and several different types of soils in both the desert background and on the road surfaces were detected using the SEBASS (LWIR) data (Figure 43). Man-made #1 and #2 were spectrally similar and ended up representing the same rooftop on one of the buildings in the scene, even though the n -dimensional visualization indicated two different pure endmembers. Soil endmembers #1, #2, and #8 were similar and have emissivity minima near 11.2 micrometers similar to calcite (Hewson, Cudahy, Jones, & Thomas, 2008; Loeppert, 2008). The emissivity minimum near 9.2 micrometers, present in most of the soil spectra, indicates the presence of silica in the soil. The compositions of soils on the road surfaces were similar to the soils in the desert background, making it difficult to entirely separate these endmembers from the background pixels using the feasibility ratio approach. At a 0.04 threshold, almost all the “Soil-Road” endmembers included background pixels, most evident in Soil-Road # 2 and #3. Most of the road soils spectra also had an emissivity minimum near 9.38 micrometers. Soil-Road #1 had a small feature near 8.08 micrometers, which differed from the rest of the spectra in the group. Residual atmospheric ozone (not removed by the atmospheric correction model) was also apparent, as evidenced by the emissivity minimum at 9.58 micrometers present in all LWIR spectra.

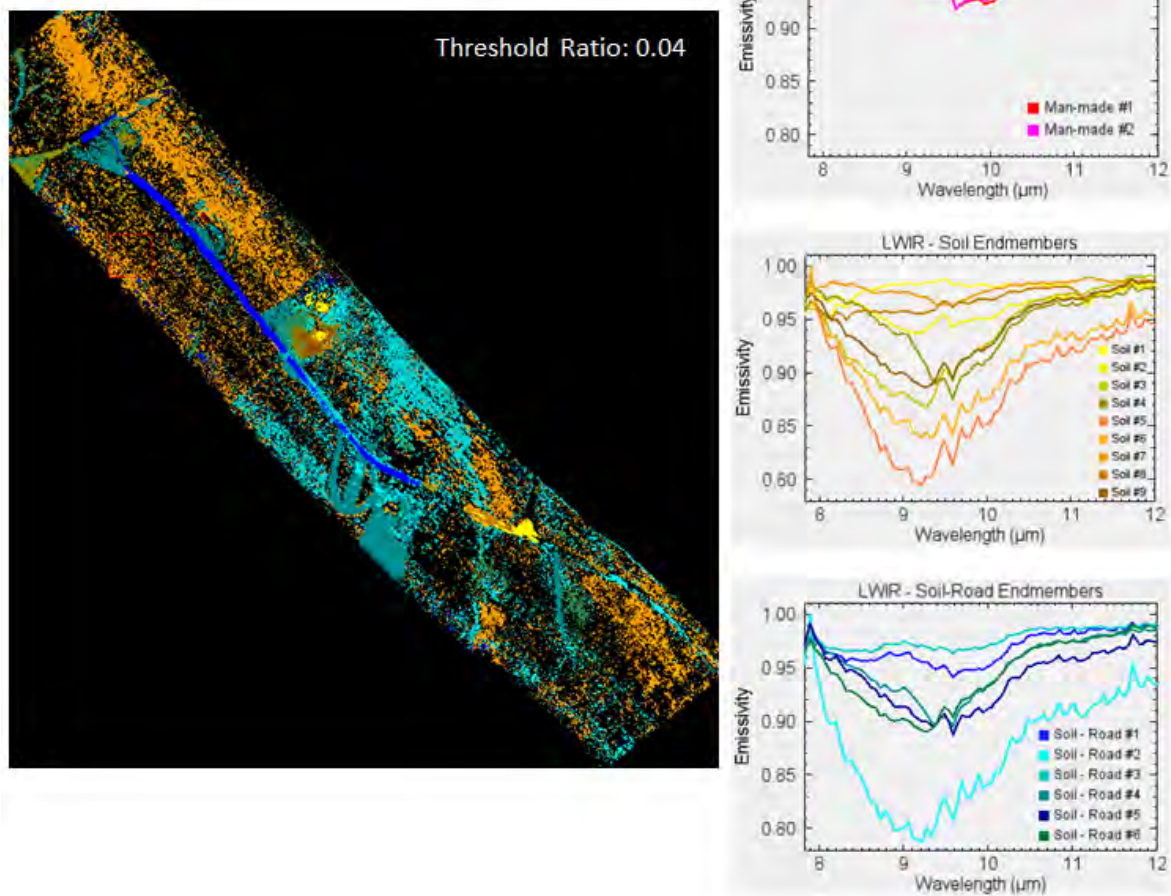


Figure 43. Image Map of SEBASS LWIR endmembers using a feasibility ratio threshold of 0.04 (Top Left); LWIR endmember reflectance spectra extracted using MNF data (Right and Bottom Spectral Plots).

The discussions above make it apparent that identification of specific materials using the individual VNIR, SWIR, and LWIR wavelength ranges can be difficult. Using two or more wavelength regions in combination potentially provides additional information that could highlight spectral similarities and differences and enhance spectral identification.

B. MNF INTEGRATION APPROACH

The forty-three non-noise MNF bands summarized in Table 5 were combined into a single dataset and the PPI algorithm was applied for 30,000 iterations. The purest 10,000 pixels from the PPI were viewed in n -dimensional space using 43 dimensions. Forty-five spectrally unique endmembers were isolated and selected for MTMF unmixing. A mask of the LWIR data was applied before the MTMF analysis to include only pixels present in both datasets.

When analyzing the MTMF feasibility ratio scores at the 0.04 ratio threshold for the integrated MNF data, very few to zero endmember pixels were extant in the classification map (Figure 44). A feasibility ratio of 0.02 was deemed more appropriate for the majority of the combined endmembers, and was used for comparison of the mapping results for the integrated datasets. The infeasibility scores were higher in the integrated analysis because of the increase of spectral content, which resulted in increased variability between the background and the endmember pixels. The higher variance simplified the extraction process of feasible endmembers; however, the average feasibility ratios were lower, and thus a reduced feasibility threshold ratio was required for mapping.

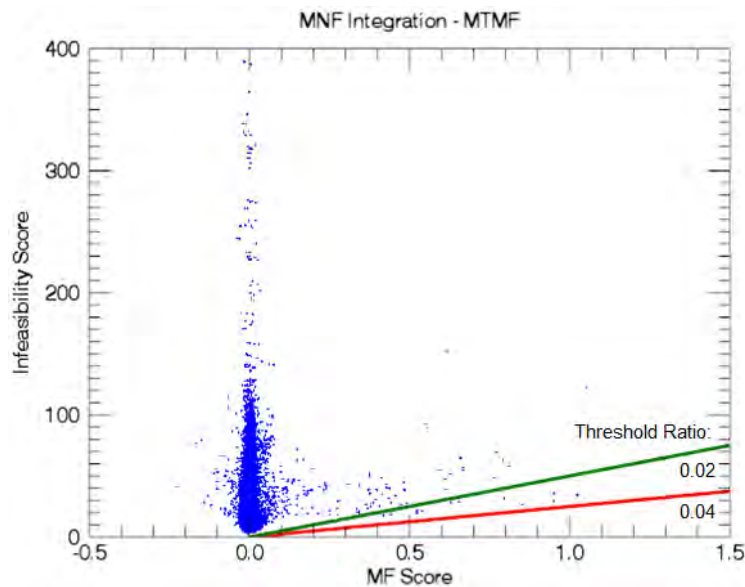


Figure 44. Comparison of ratio threshold at 0.04 (red) and 0.02 (green).

The integration of the VNIR, SWIR, and LWIR allowed further discrimination and identification of image endmembers. The MNF integration detected man-made materials, road surfaces, soils, vegetation types, as well as other unique spectra (Figure 45).

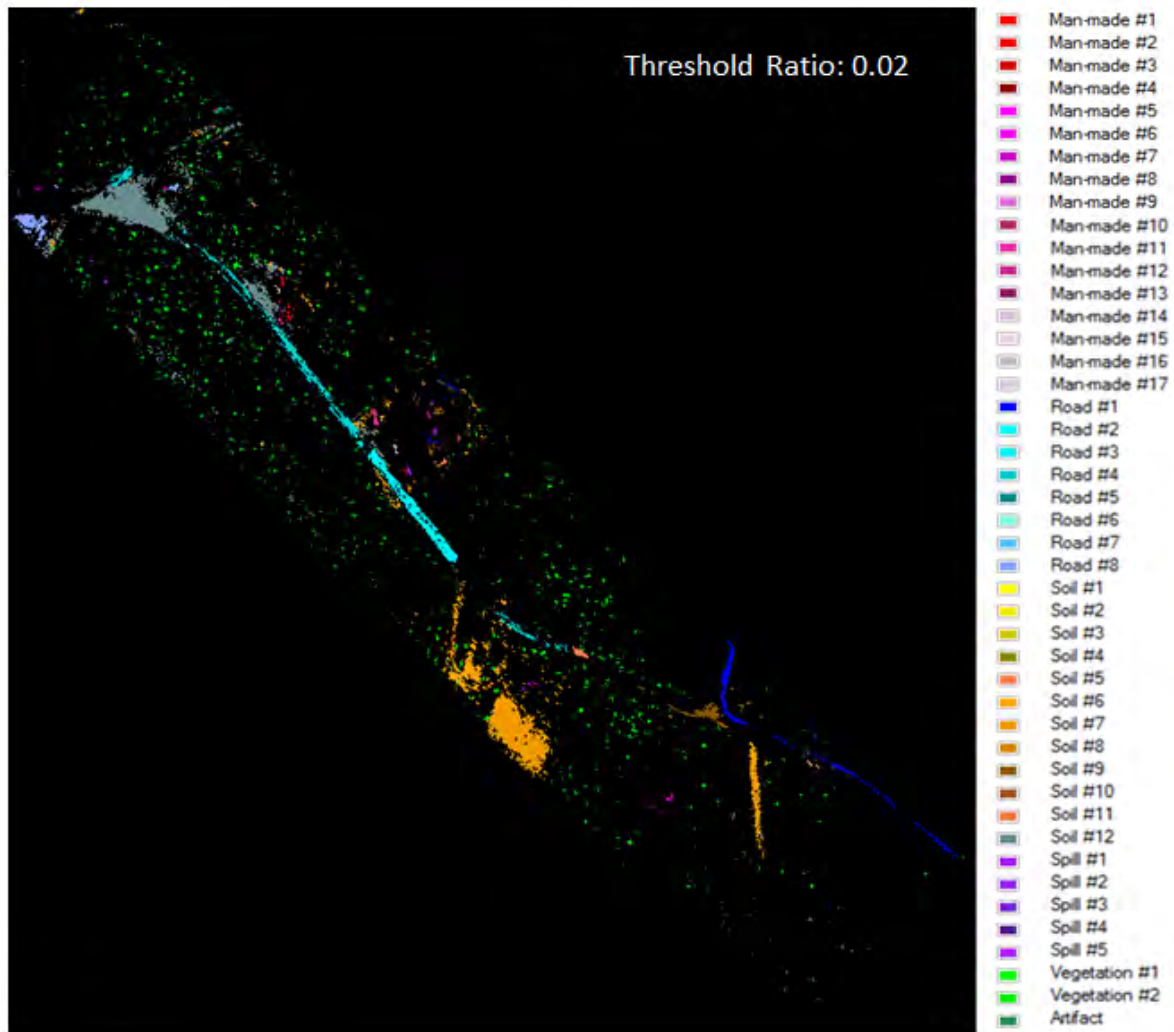


Figure 45. Image Map of MNF Integration endmembers using a feasibility ratio threshold of 0.2.

In several instances the VNIR and SWIR spectral features differed, while the LWIR spectra were similar. Likewise, for some endmembers the VNIR and SWIR spectra appeared similar, but spectral differences were seen in the LWIR. For example, Man-made #12 and #14 appeared similar in the VNIR, but differed dramatically in the

SWIR and LWIR (Figure 46). Man-made #12 has SWIR and LWIR features near 1.70, 2.15, 2.28, 9.38, and 9.58 micrometers, while Man-made #14 has LWIR features near 8.08, 9.59, 9.94, and 10.34 micrometers. Man-made #12 and #13 have similar features near 2.27 micrometers in the SWIR and the spectra appeared almost identical in the LWIR, but differed dramatically in the VNIR. The high reflectance between 0.38 to 0.57 micrometers in the Man-made #12 spectrum suggested a white material and the peak near 0.65 micrometers in Man-made #13 indicated a dark red material. Man-made #15 is mostly featureless in the VNIR and SWIR only showing a gradual increase in reflectance between 0.04 to 0.75 micrometers, but was identical to the LWIR signature of Man-made #14. Man-made #12 appeared similar to white fiberglass based on the features near 1.13, 1.69, 2.15, and 2.27 micrometers. Man-made #13 has a doublet feature near 1.12 and 1.15 micrometers expected in spectra of plastics. Man-made #14 appeared similar to library spectra of painted aluminum with a reflectance minimum near 0.43. Additional LWIR library spectra would have provided further evidence for identification, but were challenging to find for comparison.

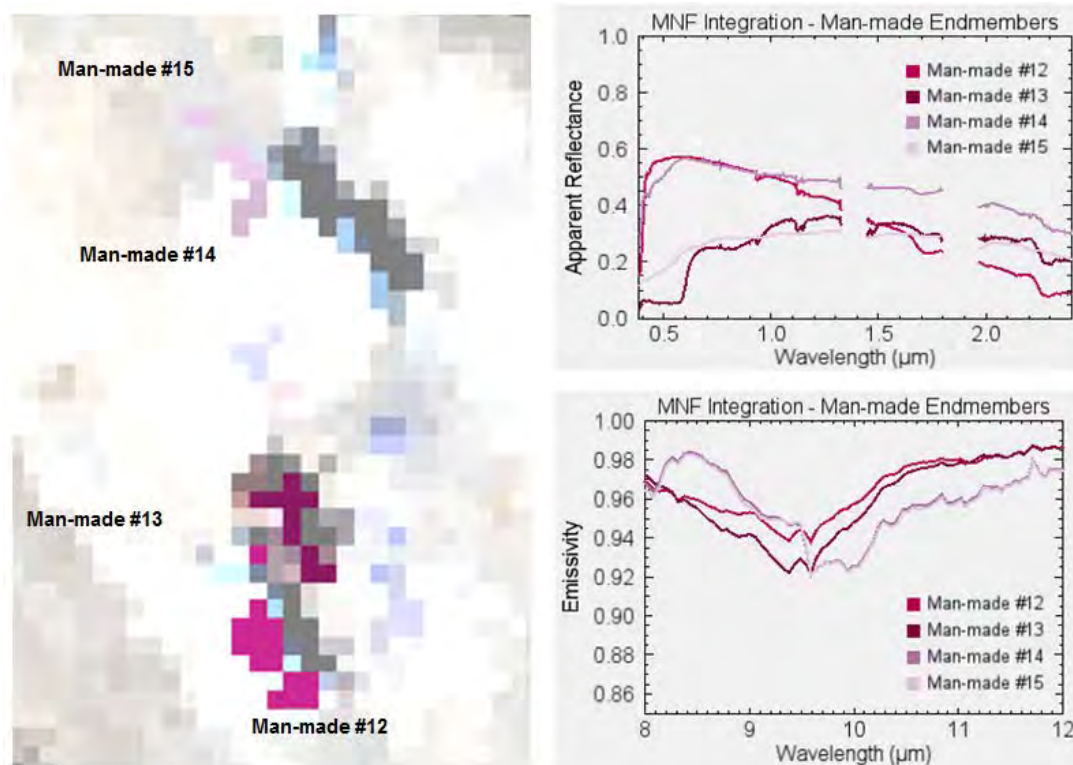


Figure 46. True color image showing classification results of Man-made #12-#15 (left); VNIR-SWIR reflectance spectra (top right); LWIR emissivity spectra (bottom right).

Spectral feature locations, depths, and shapes differed slightly in the soil and road endmembers when analyzing the full spectrum (Figure 47). Soil #6 and #7 were similar in the VNIR and SWIR with features near 0.43, 0.94, 1.71, and 2.21 micrometers. The gradual rise in reflectance from 0.4 to 0.8 micrometers suggested the presences of iron oxide in the soil. The LWIR spectra for Soil #6 and #7 were also similar, but differed in emissivity level, as well as small shape difference at the 9.38 micrometer feature. Road #3 and #4 differed slightly in all three wavelength regions. Road #3 has features near 0.99 and 1.18 micrometers and showed a more significant increase in reflectance after the 1.4 micrometer water vapor band compared to Road #4. Road #4 resembled the soil endmembers in the VNIR and SWIR, but with an additional feature near 2.13 micrometers. The Road #4 spectrum appeared more similar to Road #3 in the LWIR, but with a feature at 9.22 micrometers.

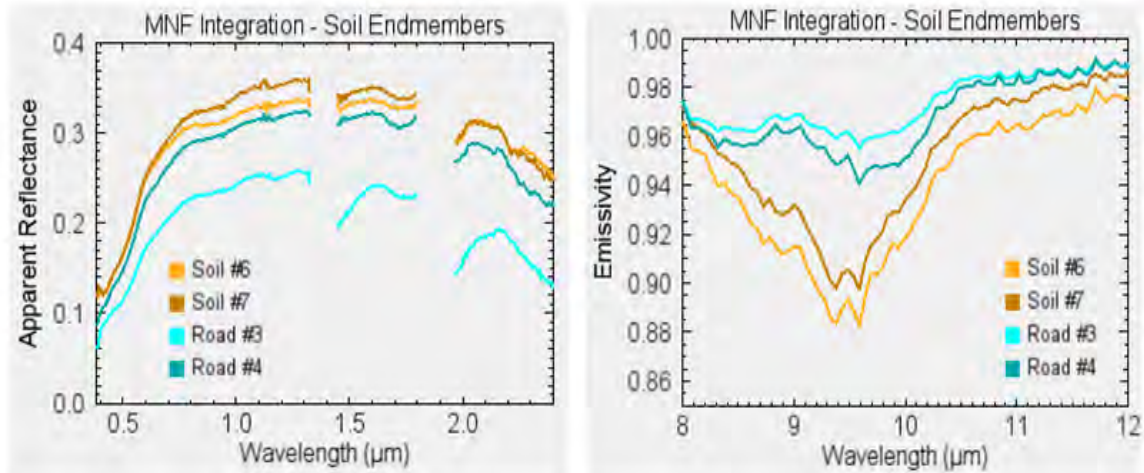


Figure 47. Full range comparison of spatially similar soil (Soil #6, Soil #7) and road (Road #3, Road #4) endmembers; VNIR-SWIR reflectance spectra (left) and LWIR emissivity spectra (right).

The different road surfaces were differentiated more effectively in the MNF Integration compared to the individual wavelength analysis (Figure 48). Road #5 and #6 appeared similar in the VNIR and SWIR with features near 0.41, 1.71, 2.13, 2.30 micrometers. Slight differences occurred at 1.16 micrometers for Road #5 and at 0.93 and 1.14 micrometers for Road #6. The 0.93 and 1.14 micrometers features are consistent with atmospheric water vapor. Unfortunately, no HSI LWIR information was obtained for the Road #5 endmember because the pixels isolated in the PPI visualization were not spatially located in the overlapping coverage area, making it difficult to determine if the water vapor features in Road #6 were real or if they were not appropriately corrected by the atmospheric model. The pixels representing Road #5 and #6 were most likely assigned to different classes because of the nonexistent LWIR data for Road #5. Road #7 appeared similar in shape and overall reflectance value to the spectra of Road #5 and #6, however, Road #7 did not have features near 1.71, 2.13, 2.30 micrometers. Road #8 has features near 0.50, 0.92, 1.11 and 2.20 micrometers. The features near the atmospheric water vapor regions were smoother and broader compared to Road #6, suggesting the features are real. The LWIR spectra for Road #7 and #8 were identical with weak features near 8.84, 9.27, 9.59, 10.09, and 11.15 micrometers. The feature near 9.27 micrometers suggests that the road surface includes a silica soil mixture.

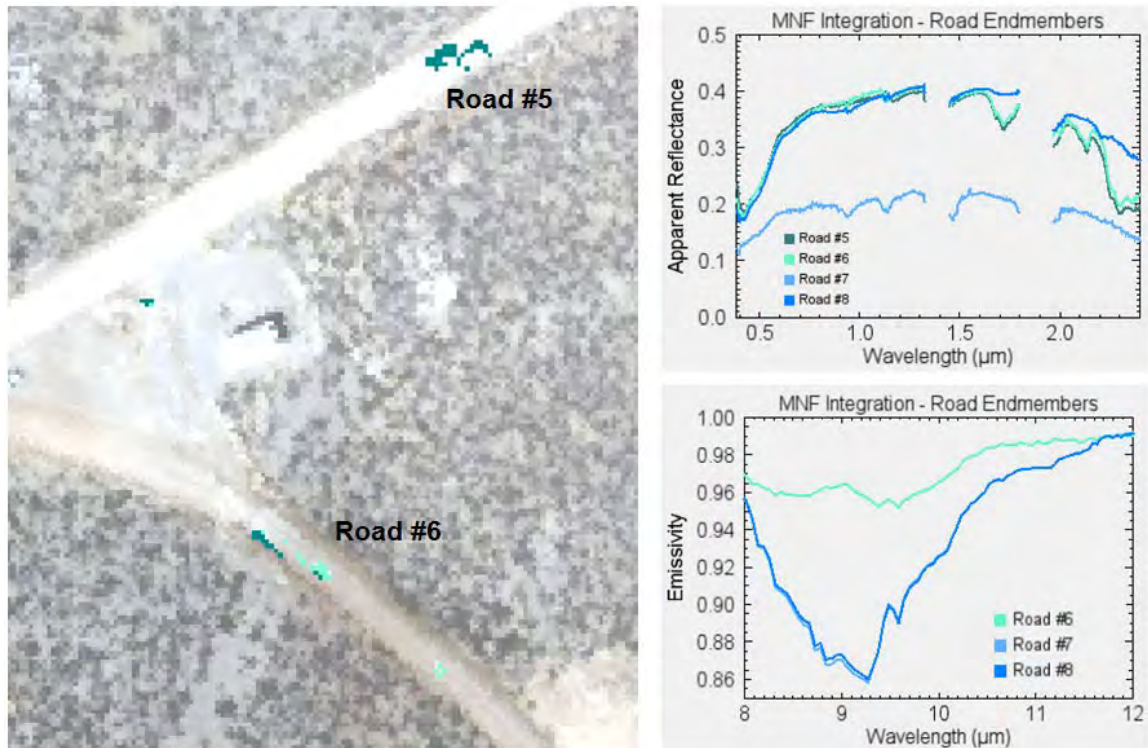


Figure 48. True color image showing classification results of Road #5 and #6 (left); VNIR-SWIR reflectance spectra of Road #5-#8 (top right); LWIR emissivity spectra of Road #6-8 (bottom right).

Further analysis of spectral features was accomplished by comparing the image spectra for Road #5 and #6 to field measurements (Figure 49). The atmospheric water vapor features near 0.93 and 1.14 micrometers were not seen in the field measurement, leading to the conclusion that the atmospheric model did not appropriately correct for water vapor in the Road #6 spectrum. The LWIR field measurement was an average of approximately ten point measurements, which explains the small differences in the spectra seen between Road #6 and the field measurement. Key features are seen the spectra near 9.38 and 9.58 micrometers. Based on the field measurement an expected feature should have been located near 8.01 micrometers.

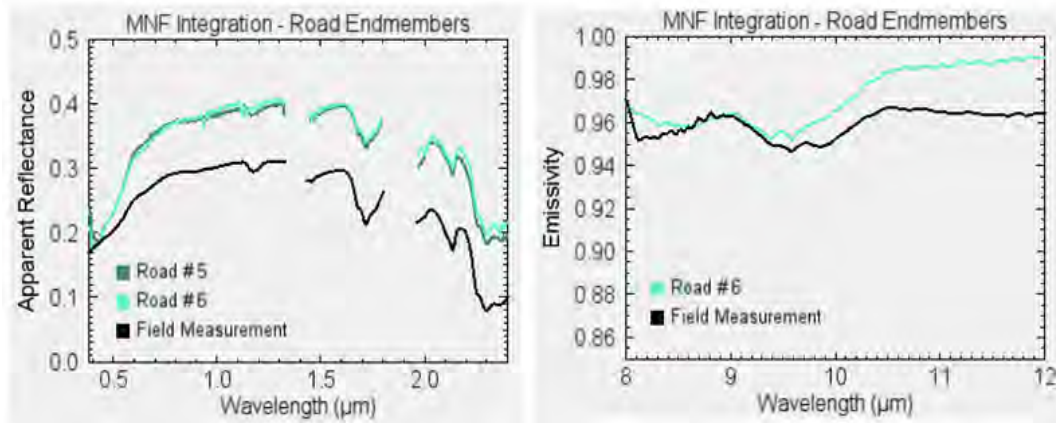


Figure 49. Spectral comparison of field (black) and image endmember spectra (green).

Fewer vegetation endmembers were detected in the integration of the non-noise MNF bands compared to the standard analysis. This may be because the vegetation spectra contain fewer features across the full range and are mostly featureless in the LWIR. Identification of Vegetation #1 was made by comparison with library spectra of sagebrush (Figure 50). Reflectance features were found at 0.68, 0.97, 1.19, 1.72, 2.10 and 2.30 micrometers in both spectra. In addition to feature locations, the overall depths and shapes were similar for the image and library spectra. The difference in overall reflectance value is most likely due to variation in collection variables, to include bidirectional effects, environment and seasonal differences, collection geometry, and field of view. Sagebrush was assumed to be present in the VNIR and SWIR analyses, but conclusive identification was not possible. Vegetation #2 is similar to #1, but has a reflectance peak near 0.63 micrometers suggesting an orange color, and has a different shape between 0.73 and 0.93 micrometers compared to Vegetation #1. No significant LWIR data was obtained for either vegetation endmember.

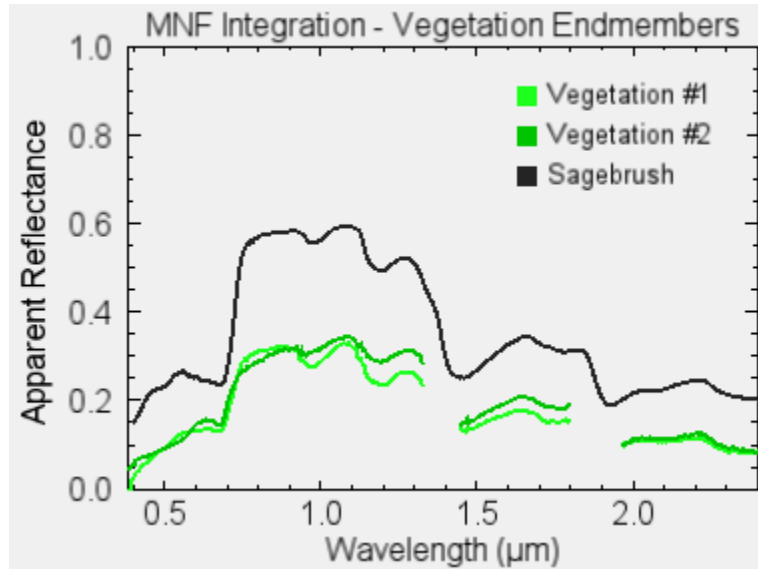
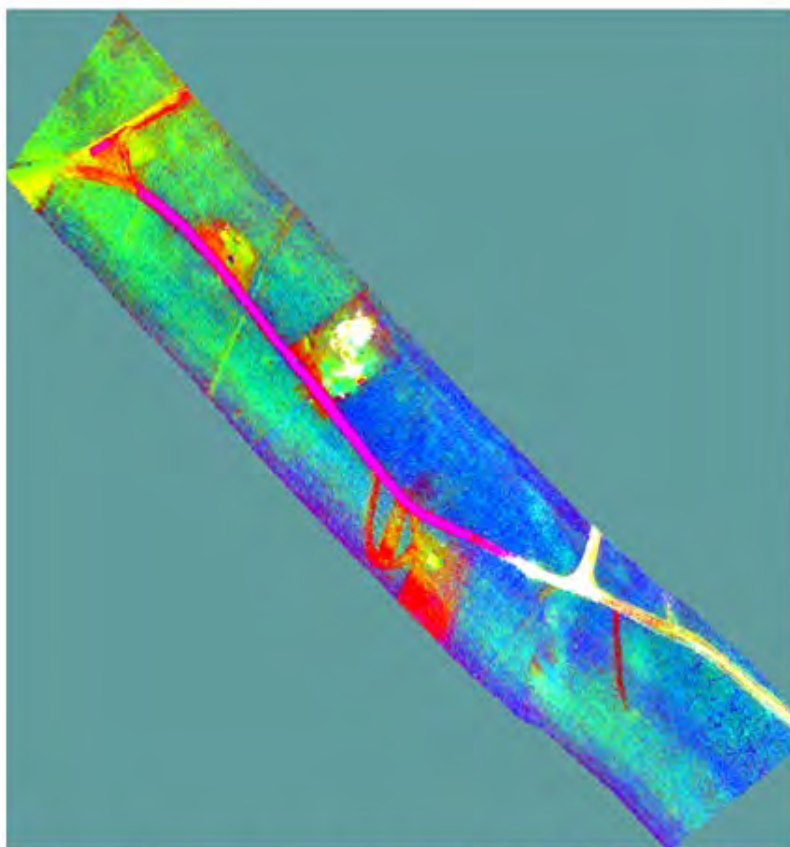


Figure 50. Spectral comparison of sagebrush library spectrum and vegetation image endmember spectra.

C. FULL INTEGRATION APPROACH

A MNF transformation was applied to the 476 bands in the combined image created by layer stacking MSS-1 bands 2-189, 214-283, and 318-413 with SEBASS bands 4-125. A mask was applied to the data to include only pixels in both the MSS-1 and the SEBASS data. A color image of MNF bands 1, 2, and 3 showed expected contrast throughout the scene. Specifically, the variations in road surfaces were apparent in the initial MNF bands (Figure 51). The MNF results of the integrated data contained less noise and fewer sensor artifacts compared to any of the individual MNF images because the artifact signals were overpowered by the signals of the surface materials. There was less user subjectivity in this approach because all the bands were included in the MNF transform, reducing the likelihood of omitted spectral information.



Full Integration (VNIR-SWIR-LWIR)
MNF Bands 1, 2, 3

Figure 51. Linear MNF transform results of full integration image displaying MNF bands 1, 2, 3 as RGB.

Of the transformed 476 input bands, the first twenty-six MNF bands contained high information content and low noise. The non-linear focal plane response of the SEBASS data was still apparent in later MNF bands even when using the corrected data, suggesting the sensor artifacts were not entirely removed from the radiance data. A PPI algorithm was applied to the twenty-six non-noise MNF bands for 30,000 iterations and using a threshold of 2.5. The response leveled out near the end of the 30,000 iterations. The 10,000 purest pixels from the PPI were visualized using twenty-six dimensions in n -dimensional space. Thirty-six endmembers were manually selected and used for MTMF analysis. The feasibility ratios were calculated, and for consistency purposes and comparison with the MNF Integrated results, a 0.02 ratio threshold was applied to the

Full Integration classification map. The classification map result was a similar to the MNF Integration, which was expected, due to the fact that MNF is a linear transformation (Green et al., 1988). Several man-made and natural materials were detected using this integration technique (Figure 52).

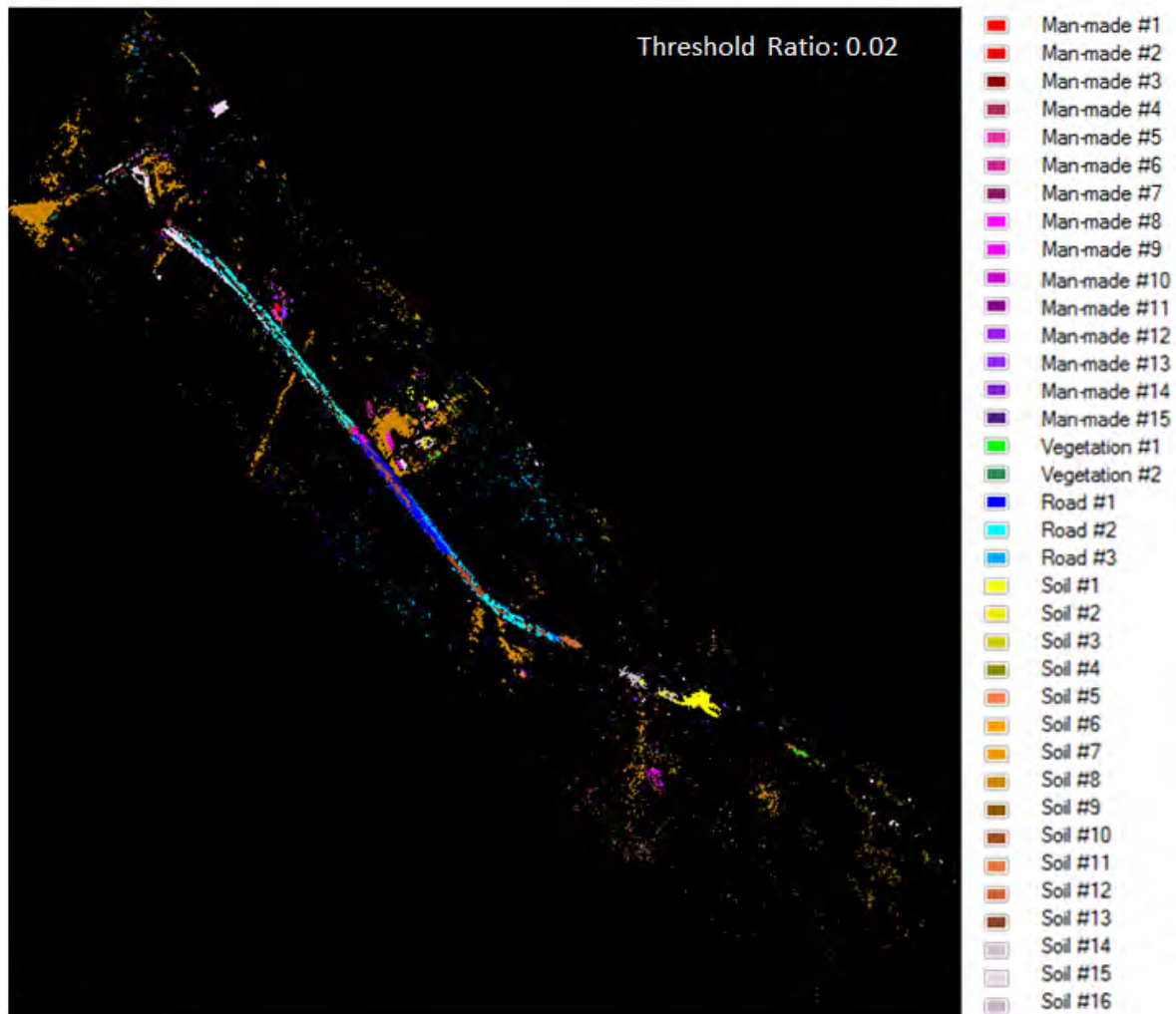


Figure 52. Image Map of MNF Integration endmembers using a feasibility ratio threshold of 0.2.

Man-made #10 and #13 have reflectance features in the VNIR and SWIR near 0.47, 0.93, 1.20, 1.54, and 1.70 (Figure 53). The location and shape of these features is consistent with opaque plastic. A library spectrum of white opaque high density polyethylene plastic was used for comparison against the man-made endmember spectra

(Figure 53). Nylon spectra also exhibit similar features, confirming the identification of a plastic polymer endmember. The 0.47 micrometer peak was more prominent in Man-made #13 and indicated the material of interest is blue in color. The shape of the LWIR spectra differ because Man-made #10 has additional features near 8.72 and a broad shallow feature ranging from 8.78 to 9.48 micrometers.

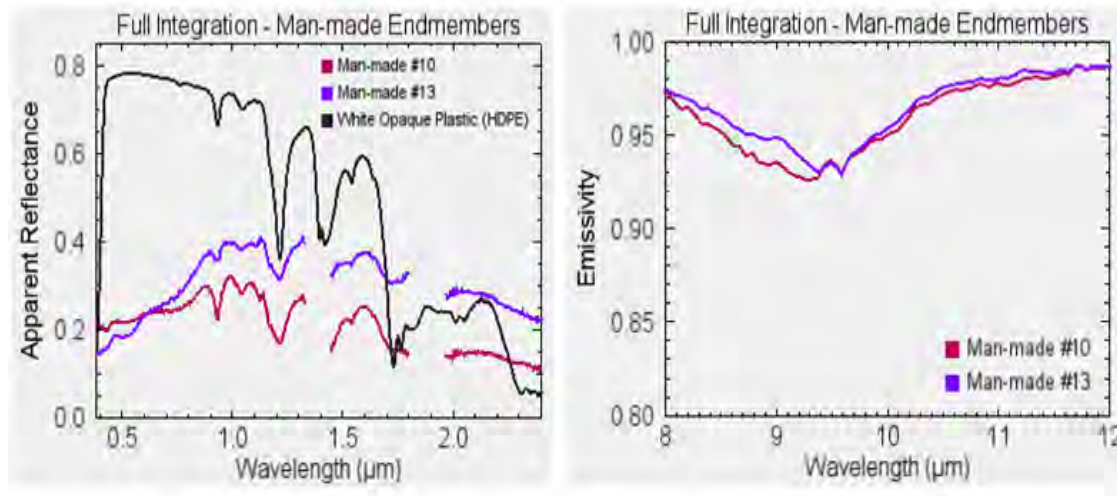


Figure 53. Spectral comparison of assumed plastic spectra; VNIR-SWIR reflectance spectra (left); LWIR emissivity spectra (right).

Iron oxides, assumed to be a mixture of goethite, were found in multiple man-made endmembers (Figure 54). Man-made #8 and #14 have broad features from 0.60 to 0.76 and 0.76 to near 1.20 micrometers commonly seen in iron oxide spectra. Both spectra have a peak near 0.60 micrometers suggesting the material is red. Man-made #14, as well as Man-made #1 and #7, appear to contain plastic based on the features at 0.93, 1.12, 1.70, and 2.30 micrometers. Man-made #7 has a feature at 0.43 and a distinctive peak at 0.56 micrometers suggesting the presence of a green painted material (similar to green painted aluminum in spectral library). The LWIR spectra are similar in shape, but Man-made #8 has deeper and smoother features from 9.0 to 9.5 micrometers and Man-made #14 has shallow features from 8.0 to 9.5 micrometers.

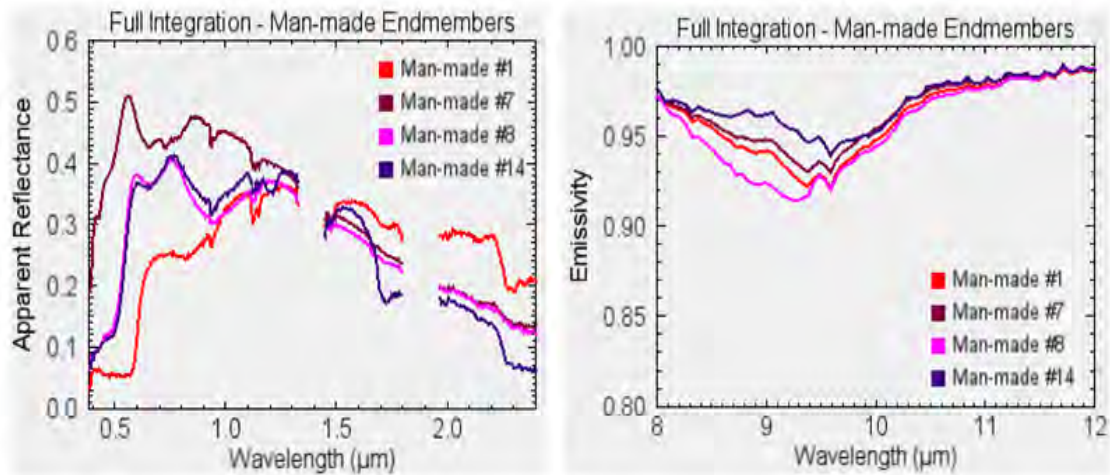


Figure 54. Spectral comparison of assumed plastic spectra; VNIR-SWIR reflectance spectra (left); LWIR emissivity spectra (right).

The majority of the predicted soil endmembers isolated in the Full Integrated method were similar in the VNIR and SWIR wavelength regions and differed most in the LWIR (Figure 55). Soil #6, #7, #8, #9, and #10 all have a gradual rise in reflectance between 0.40 to near 0.75 micrometers, suggesting the presence of iron oxide. The majority of the soils are assumed to contain a silica mixture based on the subtle LWIR features near 8.3 and 9.2 micrometers. The ozone feature near 9.60 micrometers seen in all the LWIR spectra may overpower and change the mineral features.

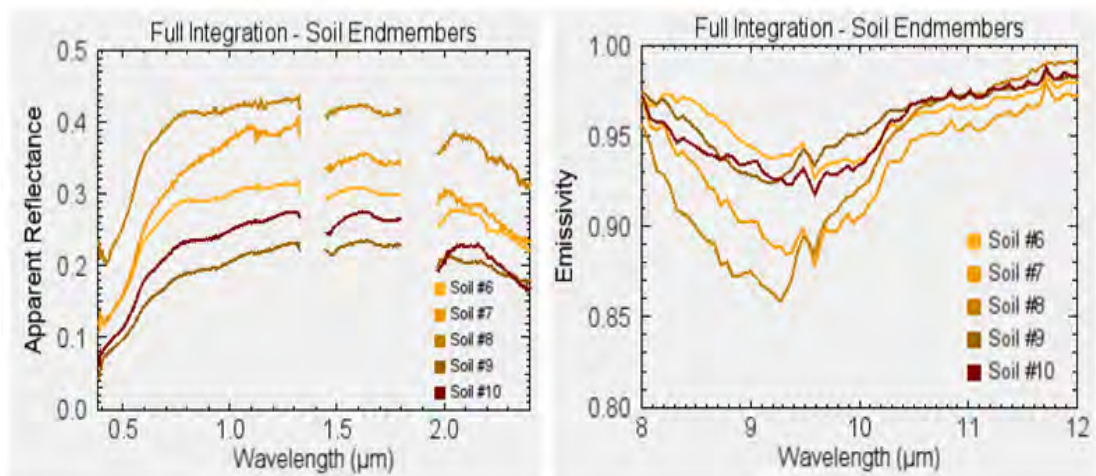


Figure 55. Spectral comparison of soil spectra; VNIR-SWIR reflectance spectra (left); LWIR emissivity spectra (right).

One of the issues emphasized in this technique was the sensitivity of the geocorrections and registration of the MSS-1 and SEBASS data. The registration errors were more pronounced in this analysis because of the increase number of bands and variance. The slight misalignment of pixels returned multiple classes because different materials were detected in the different wavelength regions. For example, the VNIR and SWIR detected a vegetation signature, while the LWIR detected a soil sample. This was specifically seen near the edges of road surfaces (Figure 56). Soil #10, Road #2, and Road #3 appear similar in shape in the VNIR-SWIR and share a common feature near 1.70 micrometers. Soil #15 has unique features at 1.12 and 2.30 micrometers and shares a similar feature with Road #2 at 2.14 micrometers. The LWIR spectra are all similar with varying levels of emissivity at 9.38 and 9.59 micrometers. Road #3 has the weakest emissivity minima, with broad shallow features from 8 to 9 micrometers and from 9 to 10 micrometers. Soil #15 shows a broad, smooth emissivity minimum from 9 to 9.4 micrometers. The overlapping class assignment on the edges of the road resulted from misalignment of MSS-1 and SEBASS pixels.

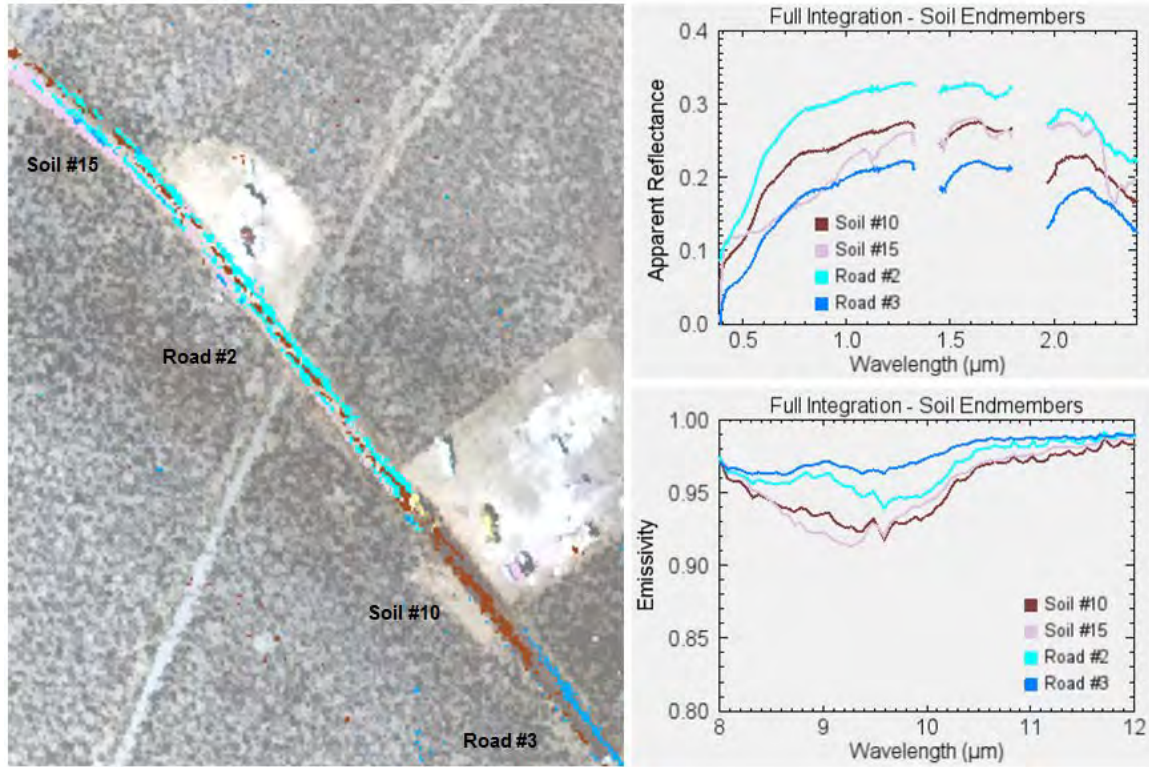


Figure 56. True color image showing classification results soil and road endmembers (left); VNIR-SWIR reflectance spectra (top right); LWIR emissivity spectra (bottom right).

Fewer vegetation classes were detected and isolated in the Full Integration. This is likely caused by the lack of vegetation features in the LWIR. The two assumed vegetation classes have spectral features near 0.68 micrometers, but the rise of the IR plateau is not as steep or as long as expected for healthy vegetation (Figure 57). The additional features in the VNIR and SWIR wavelengths at 0.96, 1.18, 1.76, 2.10, and 2.30 are consistent with several types of dry vegetation. The features in the LWIR at 8.99, 9.38, 9.59, and 10.34 micrometers are more similar to soil endmembers found in the previous analyses.

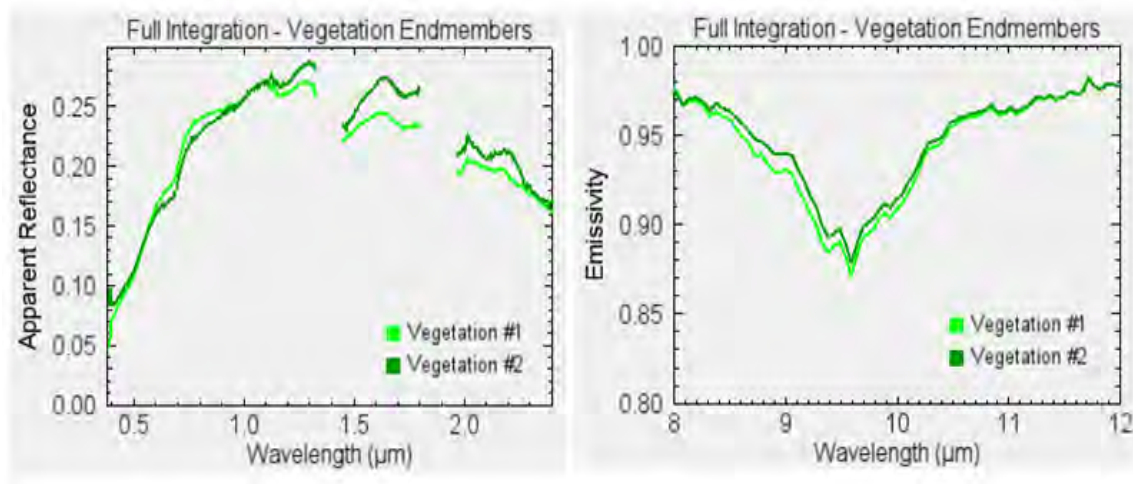


Figure 57. Spectral comparison of assumed vegetation endmember spectra; VNIR-SWIR reflectance spectra (left); LWIR emissivity spectra (right).

D. COMPARISON AND DISCUSSION OF IMAGE MAP RESULTS

The image map results from the standard hyperspectral analysis and integration methods were compared to determine how each phenomenology detected the man-made and natural endmembers within the scene (Figure 58). The individual MTMF feasibility ratio classifications maps for the VNIR, SWIR, and LWIR are located in the top and middle rows, and the MNF Integration and Full Integration results are located on the bottom row. Five spatial locations were selected across the images to provide direct comparison; descriptions are in Table 7.

Location	Description
A	Road surface (top)
B	Bare soil areas with man-made materials
C	Road surface (center)
D	Road surface (bottom)
E	Desert background

Table 7. Description of comparison locations

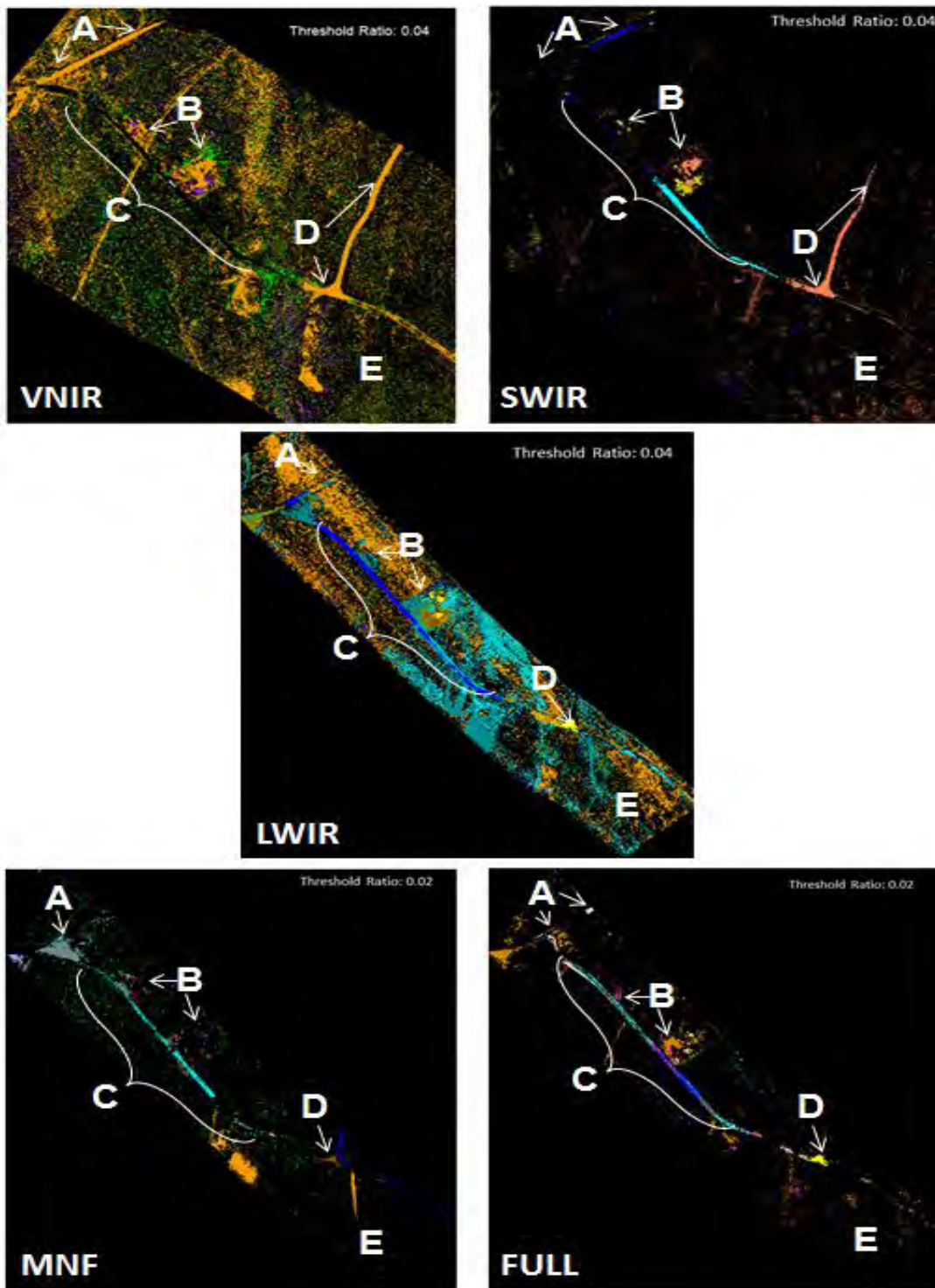


Figure 58. Comparison of MTMF feasibility ratio classification maps; VNIR (top left), SWIR (top right), LWIR (middle center); MNF Integration (bottom left), Full Integration (bottom right).

1. Comparison

Note that similar materials in each classification were assigned similar colors for consistency; however, this makes it challenging to see some of the individual endmembers at times. Also note that class color assignments are variable between the images, specifically in differentiation between soil and road surfaces, due to similarity of composition and locations. These concerns are discussed in more detail for each location.

Location (A) was mapped clearly in the VNIR and the SWIR analyses, as soil and road, respectively. The VNIR analysis did not include road classifications because the wavelengths lacked significant soil features and could not clearly differentiate between the bare soil and road surfaces. The LWIR and both integrated analyses partially mapped the area with multiple classes. Based on ground truth knowledge, the multiple class assignment in the LWIR analysis is artificial and due to inclusion of excess background pixels. The MNF analysis mapped only the area above the center road and the Full analysis mapped the area above the center road and the area farthest to the right along the road. The lack of consistent mapping in the integration is due to the influence of the LWIR data.

Location (B) emphasizes the man-made materials in the scene, consisting of buildings and large equipment. Man-made materials were detected in all analyses. Small deviations in class assignment are most clear in the VNIR, MNF, and Full analyses because these analyses included VNIR wavelengths, which are more sensitive to physical color and iron oxide content compared to the SWIR and LWIR wavelengths. Soil endmembers were most clearly located in the VNIR, SWIR, and Full analyses. A variety of soils, mixed with road classes, were detected in the LWIR. The misclassification between soil and road was common throughout the analyses because the class assignment was subjective. Few soil pixels were included in the MNF Integration image at the chosen feasibility ratio.

Location (C) representing the main road located in the center of the coverage area was detected in the SWIR, LWIR, MNF, and Full analyses. The LWIR analysis assigned the entire road to one class, while the SWIR, MNF, and Full analyses were able to

differentiate between the sections containing various additives to the bare soil. There are some artificial classes seen along this road in the Full analysis caused by coregistration errors.

Location (D) includes the intersection of the center road and a side road located near the bottom of the image. The soil and road variations were mapped in the analyses. Both the VNIR and SWIR classified the intersection, composed of bright soil, and the extending road as the same endmember. The extending road was mostly truncated in the analyses using only the LWIR and overlapping coverage area. The LWIR and Full analyses detected the intersection, but did not detect the road. The MNF analysis uniquely differentiated the soil surface intersection and the road surface.

Location (E) was selected to highlight the desert background consisting of vegetation and soil. Vegetation was most effectively detected in the VNIR, SWIR, and MNF analyses. Vegetation was not adequately mapped in the LWIR and Full analyses. Background soil pixels were best mapped in the VNIR, SWIR, and Full analyses. The LWIR also mapped a variety of soil types, but the visual analysis of the LWIR was misleading because the road endmembers in the middle of the image were unable to be fully isolated from the background pixels at the chosen feasibility ratio threshold.

2. Discussion

The VNIR analysis mapped the locations of man-made and natural endmembers within the desert scene. Man-made materials were detected based on physical color differences exhibited in the spectra and interpreted iron oxide content, but were smaller in size compared to the desert background, and therefore not as clearly seen on the map. The soil spectra generally lacked spectral features in the VNIR region, making identification difficult. Spatial context was used, however, to help determine that they were in fact soils. The vegetation spectra had prominent features in the VNIR, enabling detection and identification of several vegetation types.

The individual analysis of the SWIR region achieved detection of similar man-made and natural materials, but based on physiochemical makeup of the materials. Man-made materials, specifically plastics, were located and displayed on the image map.

Different types of soil materials were spatially and spectrally detected. The spectra from the SWIR wavelengths indicated silica and clay were present in the soil mixtures. The majority of the road surfaces were differentiated from the background and bare soil, although not all endmembers were mapped at the chosen feasibility ratio. Fewer vegetation endmembers were detected compared to the VNIR analysis, but the SWIR spectra provided evidence of dry vegetation. Class assignment was difficult using only the SWIR wavelength. Ambiguities in this spectral region caused some confusion between soils, dry vegetation, and synthetic materials.

The individual LWIR analysis detected and mapped various man-made and natural endmembers, some different from the VNIR and SWIR analyses. Spectral identification was difficult due to residual atmospheric effects present in all LWIR spectra and lack of comprehensive library spectra for comparison. No vegetation endmembers were detected in the LWIR due to the lack of features in this range. Broad emissivity features seen near 8.2 to 9.5 micrometers in the soil and road endmember spectra indicated that many of the surfaces contained silica. The main road surfaces were differentiated from the bare soils in the desert background. Inclusion of background pixels was most prevalent in the LWIR image map. This suggests that the selected feasibility ratio threshold, chosen for consistency with the standard analysis, could have been improved.

The MNF and Full Integration approaches detected man-made and natural endmembers similar to those found by the standard analyses. Man-made materials such as metal and plastics were detected and partially identified by the integrated analyses based on features seen through the VNIR, SWIR, and LWIR spectral regions. The variations in road surface materials were best differentiated (spatially and spectrally) in the integrated analyses, seen in the color differences along the center road. Although the road surfaces contained various additives mixed with the bare soil, it was difficult to separately define the soil and road classes. Fewer vegetation endmembers were detected utilizing the integrated approaches, again due to the lack of features across the full range, specifically the LWIR. Identification was achieved for the vegetation discovered in MNF

Integration analysis using spectral features found in the VNIR and the SWIR wavelength regions.

The Full Integration results were similar to the MNF Integration, as expected because MNF is a linear transform. Man-made materials were detected based on electronic and vibrational modes of the physiochemical makeup of the materials. Consistent identification of metals and plastics was obtained, mainly aluminum, fiberglass, and other synthetic materials. Identification was achieved using the spectral features across all three wavelength ranges. Soil and road variations were detected spatially and spectrally. The most variability was seen along the center road in the Full Integration compared to all other analysis methods. The majority of the unique class assignments appear to be real based on ground truth knowledge, but some were artificial caused by the misalignment of the MSS-1 and SEBASS pixels. A few possible vegetation endmembers were detected, but spatial/spectral browsing revealed that many of the corresponding LWIR spectra were not consistent with expected vegetation features. The features in the LWIR spectra suggest the predicted vegetation spectra were a mixture of vegetation and soil.

Both integrated methods produced classification maps with endmembers similar to the results obtained with the baseline analysis. Additional spatial and spectral variations of man-made, soil, and road endmembers were detected in the integrated approaches compared to the standard analysis. The integrated analyses also benefited from reduced computation and data volume making the procedure more effective and the results straight-forward. Full range analysis of spectral features provided more information for spectral identification compared to separate use of the individual wavelength regions.

THIS PAGE INTENTIONALLY LEFT BLANK

V. SUMMARY AND CONCLUSIONS

Material maps were created utilizing hyperspectral remote sensing data and analyses to explore the benefits of integrated full-range spectral analysis of the VNIR, SWIR, and LWIR wavelength regions. MSS-1 data were used for the VNIR and SWIR regions and SEBASS data were used for the LWIR region. Before beginning hyperspectral analysis, sensor artifacts were removed from both datasets. Model-based atmospheric correction algorithms were separately applied to the MSS-1 and SEBASS data. The MSS-1 data were geocorrected and the SEBASS data were resampled and registered to the MSS-1 data. Standard hyperspectral analysis consisting of spectral data reduction, spatial data reduction, n -dimensional visualization to extract possible spectral endmembers, identification of spectral endmembers using expert systems and spectral libraries, and partial unmixing and mapping using the MTMF algorithm was carried out individually on the VNIR, SWIR, and LWIR wavelength regions. After this baseline analysis was created, two integration methods were examined. The first integration method, MNF Integration, consisted of combining all non-noise MNF bands from previous analysis of the VNIR, SWIR, and LWIR. The integration occurred during the spatial reduction process. The second integration method, Full Integration, combined the reflectance bands from the VNIR and SWIR and the emissivity bands from the LWIR, and integration was achieved during the spectral reduction process. In both cases, integration was possible because the images were geocorrected, coregistered, and spatial dimensions were identical. A mask was applied before integration to include only pixels represented in both scenes. After the specific integration step, the standard analysis approaches were followed and a single classification map was created for each integration method.

The results from the standard hyperspectral analysis utilizing separate spectral regions provided detection of man-made and natural endmembers. The VNIR analysis was most effective in locating and differentiating between vegetation and soils in the desert background. Specifically, the 0.68 micrometer feature in healthy vegetation was most prevalent in VNIR. The reflectance peaks between 0.4 and 0.6 micrometers

established color of selected materials. The SWIR analysis excelled at differentiating the types of soils within the scene and identifying potential minerals present in the soils. Based on the spectral features, it can be assumed the soils are composed of phyllosilicates (2.2 to 2.3 micrometers), oxides (0.45 to 0.6 micrometers), and carbonates (2.3 to 2.34 micrometers). The LWIR analysis detected the differences between the soil background and the road surfaces. The emissivity minimum present in most of the soil spectra near 11.2 micrometers is assumed to represent calcite and the feature near 9.2 micrometers indicates the presences of silica in the soil. In all three cases, using only an individual wavelength region to analyze the scene made positive and conclusive endmember identification difficult.

The full spectral range integration methods provided more efficient analysis in a consolidated classification map. Identification improved when library spectra were available for comparison, because materials with features in multiple wavelength regions could be analyzed. For example, when examining soil endmembers, the VNIR wavelengths suggested the presence of iron oxide, the SWIR wavelengths specified the existence of carbonates, and the LWIR wavelengths gave insight into silicate material in the soil. The MNF Integration dataset detected man-made and natural materials similar to those found in the standard analysis. The inclusion of multiple wavelength regions allowed confirmation of spectral features across the full range. The results for the Full Integration were similar to the MNF Integration approach, as expected based on the fact that MNF is a linear transformation. Some exceptions occurred within the subjective endmember selection and artificial class assignments due to misalignment of MSS-1 and SEBASS pixels. Vegetation endmembers were more difficult to isolate in the integrated analysis due to the lack of specific features across the entire spectrum, notably in the LWIR.

Results would have been improved by the removal of residual atmospheric and sensor artifacts, as well as eliminating registration errors. Model-based correction algorithms provide spectra that are more similar to ground truth than the corrected spectra from most empirical methods, but are not always consistent with reality. The inconsistent results from the atmospheric correction models often differentiated similar pixels into

more than one class. The atmospheric correction was applied to the data before the standard hyperspectral or integrated analysis, so the issues were apparent in the results for both the control and the experiment. Inclusion of the full range of spectral data helped discriminate between the existence of material and atmospheric features. The MSS-1 and the SEBASS data contained sensor artifacts, which affected the isolation and class assignments of the spectral endmembers. Even though algorithms were implemented to remove the artifacts, some pixels remained influenced. The slight misalignment of the small MSS-1 and SEBASS pixels resulted in artificial spectral endmembers, where a spatial target was represented by multiple classes. This was mostly seen near the edges of the roads, and was more apparent in the Full Integration results than any of the other classification maps. Although a rural scene was used for this analysis and was not expected to dramatically change spectrally over time, the month time gap between the MSS-1 and SEBASS collects may have also contributed to incorrect pixel identification and class assignments. Artifacts due to geometric misalignments would have been minimized if a single platform with multiple sensors was used to simultaneously collect the spectral measurements.

Benefits of integrated analysis across the full wavelength range from VNIR through SWIR and LWIR include independence of the data from phenomenology units, because the data were transformed into a new data space for analysis. When combining at the spatial data reduction or the spectral data reduction step, the integrated classification maps were representative of the man-made and natural elements in the scene. The results were similar to each other and to the results obtained from the standard hyperspectral analysis. Integrated analysis was more efficient, resulting in reduced computation and data volumes compared to individually analyzing each wavelength region. Both integrated methods enabled straight-forward and effective identification, characterization, and mapping of the scene because higher variability existed between the endmembers and background. Material identification was more conclusive when analyzing across the full spectrum.

THIS PAGE INTENTIONALLY LEFT BLANK

VI. RECOMMENDATIONS FOR FUTURE WORK

While this research has validated the basic integrated analysis approaches, additional work is required to quantify improvements resulting from the integrated methods. Future work should include additional experimentation between the MNF and Full integration methods to quantify results. This would require a well-characterized site and additional, detailed ground truth. The inclusion of more field measurements would assist in the removal of atmospheric influences, specifically water vapor and ozone, and improve identification and mapping. Additional geologic ground truth of the scene with regards to reflectance and emission properties of the surface materials would also help confirm spectral and spatial identification of image endmembers. Increased availability of LWIR library spectra would be valuable in this analysis and should provide further evidence for identification. Increasing the amount of overlapping coverage in the datasets would have also been helpful for conclusive analysis. In future work, all analysis should be limited to the smallest coverage area to reduce confusion of spectral endmember assignments. The decision of assigning similar colors to similar materials should be reconsidered in future work because the visualization and differentiation of endmembers were challenging to see on the image maps. Full-range spectral analysis may also be appropriate in improving computation and reducing data volumes for other applications within remote sensing field. The benefits of integrated approaches could aid in operationally identifying specific targets of interest with known features across the EM spectrum. Additional benefits may be revealed if utilizing integrated analysis on urban scenes containing higher variability of materials. As the demand for development and operation of single platforms with multiple sensors increases, integrated analysis will become more prevalent and provide an efficient means of analysis. If the VNIR, SWIR, and LWIR data were acquired simultaneously, coregistration of the different phenomenologies and temporal differences in the data would be minimized. Simultaneously obtained data would ease and potentially reduce the analysis process, as well as reduce the number of artificial class assignments and error.

THIS PAGE INTENTIONALLY LEFT BLANK

LIST OF REFERENCES

- Abrams, M., Abbott, E., & Kahle, A. (1991). Combined use of visible, reflected infrared, and thermal infrared images for mapping Hawaiian lava flows. *Journal of Geophysical Research*, 96(B1), 475-484. doi:10.1029/90JB01392
- Adler-Golden, S. M., Gruninger, J., & Smith, D.R. (1992). Derivation of atmospheric atomic oxygen and hydrogen profiles from ozone ν_3 band emission. *Journal of Geophysical Research*, 97(A12), 19, 509-10518. doi:10.1029/92JA01544
- Adler-Golden, S. M., Conforti, P., Gagnon, M., Tremblay, P., & Chamberland, M. (2014). Long-wave infrared surface reflectance spectra retrieved from Telops Hyper-Cam imagery. *Proceedings of SPIE, Algorithms and Technologies for Multispectral, Hyperspectral, and Ultraspectral Imagery XX, Vol. 9088* (pp. 90880U-1:8). Baltimore, MD. doi:10.1117/12.2050446
- Berk, A., Bernstein, L. S., & Robertson, D. C. (1987). MODTRAN: A moderate resolution model for LOWTRAN (SSI-TR-124). Burlington, MA: Spectral Sciences. Retrieved from www.dtic.mil/cgi-bin/GetTRDoc?AD=ADA185384
- Berk, A., Bernstein, L. S., & Robertson, D. C. (1989). MODTRAN: A moderate resolution model for LOWTRAN7 (GL-TR-89-0122). Hanscom AFB, Bedford, MA: Air Force Geophysics Laboratory. Retrieved from www.dtic.mil/dtic/tr/fulltext/u2/a214337.pdf
- Bernstein, L. S., Jin, X., Gregor, B., & Adler-Golden, S. M. (2012). Quick atmospheric correction code: Algorithm description and recent upgrades. *Optical Engineering*, 51(11), 111719-1:11. doi:10.1117/1.OE.51.11.111719
- Boardman, J. W. (1993). Automating spectral unmixing of AVIRIS data using convex geometry concepts. In *Proceedings of Summaries of the 4th Annual JPL Airborne Geoscience Workshop: Vol. 1* (pp. 11-14). Pasadena, CA: Jet Propulsion Laboratory.
- Boardman, J. W., Kruse, F. A., & Green, R. O. (1995). Mapping target signatures via partial unmixing of AVIRIS data. In *Proceeding of Summaries of the 5th Annual JPL Airborne Geoscience Workshop: Vol. 1* (pp. 23-26). Pasadena, CA: Jet Propulsion Laboratory.
- Boardman, J. W., & Kruse, F. A. (2011). Analysis of imaging spectrometer data using n - dimensional geometry and a mixture-tuned matched filtering approach. *IEEE Transactions on Geoscience and Remote Sensing*, 49(11), 4138-4152. doi:10.1109/TGRS.2011.2161585

- Campbell, J. B. (2002). *Introduction to remote sensing* (3rd ed.). New York: The Guilford Press.
- Chen, X., Warner, T. A., & Campagna, D. J. (2007). Integrating visible, near-infrared and short-wave infrared hyperspectral and multispectral thermal imagery for geological mapping at Cuprite, Nevada. *Remote Sensing of Environment*, 110(3), 344-356. doi: 10.1016/j.rse.2007.03.015
- Chen, X., Warner, T. A., & Campagna, D. J. (2010). Integrating visible, near-infrared and short-wave infrared hyperspectral and multispectral thermal imagery for geological mapping at Cuprite, Nevada: A rule-based system. *International Journal of Remote Sensing*, 31(7), 1733–1752. doi: 10.1080/01431160902926616
- Clark, R. N. and Roush, T. L. (1984). Reflectance spectroscopy: Quantitative analysis techniques for remote sensing applications. *Journal of Geophysical Research: Solid Earth*, 89(B7), 6329–6340. doi:10.1029/JB089iB07p06329
- Clark, R. N., Swayze, G. A., Livo, K. E., Kokaly, R. F., King, T. V. V., Dalton, J. B. ... McDougal, R. R. (2002). Surface reflectance calibration of terrestrial imaging spectroscopy data: A tutorial using AVIRIS. In *Proceedings of the 10th Airborne Earth Science Workshop* (pp. 1–21). Pasadena, CA: Jet Propulsion Laboratory.
- Clark, R. N., Swayze, G. A., Livo, K. E., Hoefen, T., Kokaly, R. F., Sutley, S. J. ... Gent, C. A. (2003). Imaging spectroscopy: Earth and planetary remote sensing with the USGS Tetracorder and expert systems. *Journal of Geophysical Research*, 108(E12), 5131, 5-1-5-44. doi: 10.1029/2002JE001847
- Collins, B. H. (1996). *Thermal imagery spectral analysis* (master's thesis). Retrieved from Defense Technical Information Center www.dtic.mil/cgi-bin/GetTRDoc?AD=ADA320553
- Cudahy, T. J., Wilson, J., Hewson, R., Linton, P., Harris, P., Sears, M. ... Hackwell, J. A. (2001). Mapping porphyry-skarn alteration at Yerington, Nevada, using airborne hyperspectral VNIR-SWIR-TIR imaging data. In *Proceedings of the International Geoscience and Remote Sensing Symposium, IGARSS 2001: Vol. 2* (pp. 631-633). Sydney, NSW: IEEE International. doi:10.1109/IGARSS.2001.976573
- DiStasio, Jr., R. J., & Resmini, R. G. (2010). Atmospheric compensation of thermal infrared hyperspectral imagery with the emissive empirical line method and the in-scene atmospheric compensation algorithms: A comparison. *Proceedings of SPIE, Algorithms and Technologies for Multispectral, Hyperspectral, and Ultraspectral Imagery XVI, Vol. 7695* (pp. 76952B-1:12). Orlando, FL. doi:10.1117/12.849898
- D&P Instruments (2009). *Model 102 portable FTIR instruction manual* (version 1.4). Simsbury, CT: Author.

- Elachi, C. (1987). *Introduction to physics and techniques of remote sensing*. Upper Saddle River, NJ: John Wiley & Sons.
- Elvidge, Christopher D. (1990). Visible and near infrared reflectance characteristics of dry plant materials. *International Journal of Remote Sensing*, 11(10), 1775–1795. doi: 10.1080/01431169008955129
- EXELIS, Ed. (2014). *ENVI help* (version 5.1). McLean, VA: Author.
- EXELIS, Ed. (2013). *ENVI classic tutorial: Georeferencing images using input geometry*. McLean, VA: Author.
- Fehner, T.R., & Gosling F.G. (2000). *Origins of the Nevada Test Site* (DOE/MA-0518). Washington, DC: History Division, Executive Secretariat, Management and Administration, United States Department of Energy. Retrieved from <http://www.dd.anl.gov/ddtraining/50yrsNTSHistory.pdf>
- Fountanas, L. (2004). *Principal components based techniques for hyperspectral image data* (master's thesis). Retrieved from Defense Technical Information Center www.dtic.mil/cgi-bin/GetTRDoc?AD=ADA429890
- Gao, B. C., Heidebrecht, K. B., & Goetz, A. F. H. (1993). Derivation of scaled surface reflectances from AVIRIS data. *Remote Sensing of Environment*, 44(2-3), 165–178. doi: 0.1016/0034-4257(93)90014-O
- Goetz, A.F.H., Vane, G., Solomon, J.E., & Rock, B.N. (1985). Imaging spectrometry for earth remote sensing. *Science*, 228(4704), 1147–1153. doi:10.1126/science.228.4704.1147
- Goetz, A.F.H. (1992). Imaging spectrometry: Sensors and data analysis. In *Proceedings of the International Geoscience and Remote Sensing Symposium IGARSS* (pp. 547-548). Houston, TX: IEEE.
- Goetz, A. F.H. (2009). Three decades of hyperspectral remote sensing of the Earth: A personal view. *Remote Sensing of Environment*, 113(supplement 1), S5–S16. doi:10.1016/j.rse.2007.12.014
- Green, A. A., Berman, M., Switzer, P., & Craig, M. D. (1988). A transformation for ordering multispectral data in terms of image quality with implications for noise removal. *IEEE Transactions on Geoscience and Remote Sensing*, 26(1), 65–74. doi:10.1109/36.3001
- Green, R. O., Eastwood, M. L., Sarture, C. M., Chrien, T. G., Aronsson, M., Chippendale, B. J. ... Williams, O. (1998). Imaging spectroscopy and the airborne visible/infrared imaging spectrometer (AVIRIS). *Remote Sensing of Environment*, 65(3), 227-248. doi:10.1016/S0034-4257(98)00064-9

- Griffin, M. K., & Burke, H. K. (2003). Compensation of hyperspectral data for atmospheric effects. *Lincoln Laboratory Journal*, 14(1), 29–54. Retrieved from https://www.ll.mit.edu/publications/journal/pdf/vol14_no1/14_1compensation.pdf
- Hackwell, J. A., Warren, D. W., Bongiovi, R. P., Hansel, S. J., Hayhurst, T. L., Mabry, D. J. ... Skinner, J. W. (1996). LWIR/MWIR imaging hyperspectral sensor for airborne and ground-based remote sensing. *Proceedings of Proceedings of SPIE, Imaging Spectrometry II*, 102, Vol. 2819 (pp. 102–107). Denver, CO. doi:10.1117/12.258057
- Hewson, R.D., Cudahy, T.J., Jones, M., and Thomas, M. (2012). Investigations into soil composition and texture using infrared spectroscopy (2–14 μ m). *Applied and Environmental Soil Science*, 2012(535646), 1-12. doi:10.1155/2012/535646
- Hook, S. J., Abbott, E. A., Grove, C., Kahle, A. B., & Palluconi, F. (1999). Use of multispectral thermal infrared data in geological studies. In A. N. Rencz (Ed.), *Remote sensing for the earth sciences: Manual of remote sensing*, vol. 3 (pp. 59–110). New York: John Wiley and Sons.
- Hook, S. J. Myers, J. J., Thome, K. J., Fitzgerald, M., & Kahle, A. B., (2001). The MODIS/ASTER airborne simulator (MASTER) - a new instrument for earth science studies. *Remote Sensing of Environment*, 76(1), 93–102. doi:10.1016/S0034-4257(00)00195-4
- Hunt, G.R., & Ashley R.P. (1979). Spectra of altered rocks in the visible and near infrared. *Economic Geology*, 74(7), 1613-1629. doi: 10.2113/gsecongeo.74.7.1613
- Salvaggio, C., Miller, C., Bauer, R., & Lewis, P. (2001). *Infrared field spectra collection protocol (Ver 1.0)*. Fairfax, VA: Spectral Information Technology Applications Center. Retrieved from http://dirs.cis.rit.edu/instrument_protocols/Field_IR_Protocol.pdf
- Kealy, P. S., & Hook, S. J. (1993). Separating temperature and emissivity in thermal infrared multispectral scanner data: Implications for recovering land surface temperatures. *IEEE Transactions on Geoscience and Remote Sensing*, 31(6), 1155–1164. doi:10.1109/36.317447
- Kerekes, J.P., Strackerjan, K.E., & Salvaggio, C. (2008). Spectral reflectance and emissivity of man-made surfaces contaminated with environmental effects. *Optical Engineering*, 47(10), 106201-1:10. doi:10.1117/1.3000433
- Keshava, N., & Mustard, J. F. (2002). Spectral unmixing. *Signal Processing Magazine, IEEE*, 19(1), 44–57. doi:10.1109/79.974727

- Kirkland, L., Herr, K., Keim, E., Adams, P., Salisbury, J., Hackwell, J., & Treiman, A. (2002). First use of an airborne thermal infrared hyperspectral scanner for compositional mapping. *Remote Sensing of Environment*, 80(3), 447–459. doi:10.1016/S0034-4257(01)00323-6
- Kokaly, R.F., Despain, D.G., Clark, R.N., & Livo, K.E. (2007). *Integrated geoscience studies in the greater Yellowstone area-volcanic, tectonic, and hydrothermal processes in the Yellowstone geoecosystem* (Professional Paper 1717). Bozeman, MT: U.S. Geological Survey. Retrieved from <http://pubs.usgs.gov/pp/1717/downloads/pdf/p1717N.pdf>
- Kruse, F. A. (1988). Use of airborne imaging spectrometer data to map minerals associated with hydrothermally altered rocks in the northern Grapevine Mountains, Nevada and California, *Remote Sensing of Environment*, 24(1), 31–51. doi:10.1016/0034-4257(88)90004-1
- Kruse, F. A., Lefkoff, A. B., & Dietz, J. B. (1993a). Expert system-based mineral mapping in northern Death Valley, California/Nevada using the Airborne Visible/Infrared Imaging Spectrometer (AVIRIS). *Remote Sensing of Environment*, 44(2-3), 309–336. doi:10.1016/0034-4257(93)90024-R
- Kruse, F. A., Lefkoff, A. B., Boardman, J. B., Heidebrecht, K. B., Shapiro, A. T., Barloon, P. J., & Goetz, A. F. H. (1993b). The spectral image processing system (SIPS) - interactive visualization and analysis of imaging spectrometer data. *Remote Sensing of Environment*, 44(2-3), 145-163. doi:10.1016/0034-4257(93)90013-N
- Kruse, F. A. (2002). Combined SWIR and LWIR mineral mapping using MASTER / ASTER. In *Proceedings of the International Geoscience and Remote Sensing Symposium, IGARSS 2002: Vol. 4* (pp. 2267-2269). Toronto, Canada: IEEE International. Published on CD ROM–Paper Int1_B15_04, 2267 – 2269. doi:10.1109/IGARSS.2002.1026514
- Kruse, F. A. (2004). Comparison of ATREM, ACORN, and FLAASH atmospheric corrections using low-altitude AVIRIS data of Boulder, Colorado. In *Proceedings of the 13th JPL Airborne Geoscience Workshop* (pp. 1–10). Pasadena, CA: Jet Propulsion Laboratory.
- Kruse, F. A. (2008). Expert system analysis of hyperspectral data. In *Proceedings of SPIE Defense and Security, Algorithms and Technologies for Multispectral, Hyperspectral, and Ultraspectral Imagery XIV, Vol. 6966* (pp. 69660Q-1:12). Orlando, FL. doi:10.1117/12.767554
- Kruse, F. A., Taranik, J. V., Coolbaugh, M., Michaels, J., Littlefield, E. F., Calvin, W. M. ... Martini, B. A. (2011). Effect of reduced spatial resolution on mineral mapping using imaging spectrometry – Examples using HypsIRI-simulated data. *Remote Sensing*, 3(8), 1584–1602. doi:10.3390/rs3081584

- Loeppert, R. (2008). Soil Chemistry. In W. Chesworth (Ed.), *Encyclopedia of soil science* (pp. 637–641). Dordrecht, The Netherlands: Springer.
- Lyon, R.J.P. (1964). *Evaluation of infrared spectrophotometry for compositional analysis of lunar and planetary soils* (NASA Contractor Report 100). Washington, D.C.: National Aeronautics and Space Administration. Retrieved from http://ntrs.nasa.gov/archive/nasa/casi.ntrs.nasa.gov/19650001173_1965001173.pdf
- Matthew, M. W., Adler-Golden, S. M., Berk, A., Felde, G. W., Anderson, G. P., Gorodetzky, D. ... Shippert, M. (2003). Atmospheric correction of spectral imagery: Evaluation of the FLAASH algorithm with AVIRIS data. In *Proceedings of SPIE Algorithms and Technologies for Multispectral, Hyperspectral, and Ultraspectral Imagery IX, Vol. 5093* (pp. 474–482). Orlando, FL. doi:10.1117/12.499604
- Milton, E.J., Schaepman, M.E., Anderson, K., Kneubuhler, M., & Fox, N. (2009). Progress in field spectroscopy. *Remote Sensing of Environment, 113*(Supplement 1), S92-S109. doi:10.1016/j.rse.2007.08.001
- Moersch, J.E., & Christensen, P.R. (1995). Thermal emission from particulate surfaces: A comparison of scattering models with measured spectra. *Journal of Geophysical Research, 100*(E4), 7465-7477. doi:10.1029/94JE03330
- National Research Council. (2007). *Earth science and applications from space: National imperatives for the next decade and beyond*. Washington, DC: The National Academies Press. Retrieved from http://www.nap.edu/catalog.php?record_id=11820
- Olsen, R. C. (2014). *Remote sensing from air and space* (2nd Ed.) Bellingham, WA: SPIE Press.
- Peterson, D.L., & Hubbard, G.S. (1992). Scientific issues and potential remote sensing requirements for plant biogeo-chemical content. *Journal of Imaging Science and Technology, 36*(5), 445–455.
- Ramachandran, V. R., Jacobs, S. K., Firpi, A. H., Mitchell, H. J., Tzeng, N. H., & Rodriguez, B. M. (2014). Spectral comparison using k-means clustering. In *Proceedings of the 2014 IEEE Aerospace Conference* (pp. 1–10). Big Sky, MT. doi:10.1109/AERO.2014.6836472
- Rees, W.G. (2013). *Physical principles of remote sensing* (3rd Ed.). Cambridge: Cambridge University Press.
- Richards, J. A., & X. Jia (2013). *Remote sensing digital image analysis: An introduction* (5th Ed.). Berlin, Germany: Springer.

- Richter, R. (1996). A spatially adaptive fast atmospheric correction algorithm. *International Journal of Remote Sensing*, 17(6), 1201–1214. doi:10.1080/01431169608949077
- Riedl, M. J. (2001). *Optical design fundamentals for infrared systems* (2nd Ed.). SPIE Press. Bellingham, WA: SPIE Press. doi:10.1117/3.412729
- Scheffler, D., & Karrasch, P. (2014). Destriping of hyperspectral image data: An evaluation of different algorithms using EO-1 Hyperion data. *Journal of Applied Remote Sensing*, 8(1), 083645-1-083645-18. doi:10.1117/1.JRS.8.083645
- Shaw, G. A., & Burke, H. H. K. (2003). Spectral imaging for remote sensing. *Lincoln Laboratory Journal*, 14(1), 3–28. Retrieved from https://www.ll.mit.edu/publications/journal/pdf/vol14_no1/14_1remotesensing.pdf
- Simi, C., Reith, E., & Olchowski, F. (2009). The mapping reflected-energy sensor-MaRS: a new level of hyperspectral technology. In *Proceedings of SPIE, Imaging Spectrometry XIV, Vol. 7457* (pp. 745703–745703). San Diego, CA. doi:10.1117/12.830098
- Shapley, P. (2012). Light and the electromagnetic spectrum: The electromagnetic spectrum [Online]. Retrieved from: <http://butane.chem.uiuc.edu/pshapley/GenChem2/A3/3.html>
- Spectra Vista Corporation (2013) *SVC HR-1024i/SVC HR-768i user manual*. Poughkeepsie, New York: Author.
- Tarantola, A., & Valette, B. (1982). Generalized nonlinear inverse problems solved using least squares criterion. *Reviews of Geophysics and Space Physics*, 20(2), 219–232. doi: 10.1029/RG020i002p00219
- van der Meer, F. D., & S. M. de Jong (2011). *Imaging spectrometry: Basic principles and prospective applications* (Vol. 4). Dordrecht, Netherlands: Springer.
- Vaughan, R. G., & Calvin, W. M. (2004). Synthesis of high-spatial resolution hyperspectral VNIR / SWIR and TIR image data for mapping weathering and alteration minerals in Virginia City, Nevada. In *Proceedings of the International Geoscience and Remote Sensing Symposium, IGARSS 2004: Vol. 2* (pp. 1296–1299). Anchorage, AK: IEEE International. doi:10.1109/IGARSS.2004.1368654
- Vincent, R.K., & Thomson, F. (1972). Spectral compositional imaging of silicate rocks. *Journal of Geophysical Research*, 77(14), 2465–2472. doi:10.1029/JB077i014p02465

- Warner, T. A., & Nerry, F. (2009). Does single broadband or multispectral thermal data add information for classification of visible, near- and shortwave infrared imagery of urban areas? *International Journal of Remote Sensing*, 30(9), 2155–2171. doi:10.1080/01431160802549286
- Wright, C., Riley, D. N., Peppin, W.A., & Schulenburg, N.W. (2008). *Mineral exploration in the western United States using visible – short wave infrared and a mid wave – long wave infrared hyperspectral imagers: Joint airborne collection using hyperspectral systems (JACHS)*. Reno, NV: Spectral Technology and Innovative Research Corporation. Retrieved from http://www.spectir.com/wp-content/uploads/2011/12/prospectir_sebass_collect.pdf
- Young, S. J., Johnson, R., & Hackwell, J.A. (2002). An in-scene method for atmospheric compensation of thermal hyperspectral data. *Journal of Geophysical Research*, 107(D24), 4774, 14-1:20. doi:10.1029/2001JD001266
- Yamaguchi, Y., Kahle, A. B., Tsu, H., Kawakami, T., & Pniel, M. (1998). Overview of advanced spaceborne thermal emission reflectance radiometer. *IEEE Transactions on Geoscience and Remote Sensing*, 36(4), 1062–1071. doi:10.1109/36.700991

INITIAL DISTRIBUTION LIST

1. Defense Technical Information Center
Ft. Belvoir, Virginia
2. Dudley Knox Library
Naval Postgraduate School
Monterey, California